Technical Developments for the Inspection of Off-shore Wind Blades: Final Report

NOWRDC #126 Report Deliverables for 4.1

EPRI
3420 Hillview Avenue, Palo Alto, California 94304-1338 USA
800.313.3774 ▪ 650.855.2121 ▪ askepri@epri.com ▪ www.epri.com

NOTE

For further information about EPRI, call the EPRI Customer Assistance Center at 800.313.3774 or e-mail askepri@epri.com.

Together…Shaping the Future of Energy®

ACKNOWLEDGMENTS

EPRI and the following organizations, under contract to EPRI, contributed to the preparation of this report:

Electric Powe Research Institute (EPRI)
Principal Investigators
N. Myrent
G. Connolly
M. Dennis
M. Rencheck
S. Villalobos
B. Fitchett
L. Haus

Advanced Microwave Imaging
1481 Sherwood Forest Blvd
Baton Rouge, LA 70815

Principal Investigator
R. Stakenborghs

TPI Composites
373 Market Street
Warren, RI 02885

Principal Investigator
Stephen C. Nolet

This publication is a corporate document that should be cited in the literature in the following manner: *Technical Developments for the Inspection of Off-shore Wind Blades: Final Report: NOWRDC #126 Report Deliverables for 4.1.* EPRI, Palo Alto, CA: 2023.

ABSTRACT

This report presents information related to the inspection and evaluation of offshore wind (OSW) turbine blades prior to turbine commissioning. This report focuses on the use of ultrasonic and microwave testing techniques for the evaluation of wind blade quality and development of acceptance criteria as critical manufacturing flaws manifest. The combination of these two techniques can provide valuable information for the inspection of the components during manufacturing and could pave the way to suitable delivery platforms for field inspection applications.

Testing was performed on samples which were fabricated on a previous DOE research project to proof the technologies and advancements that have occurred in NDE inspection techniques over the past decade. From there, additional lab samples were fabricated by TPI Composites with features specific to OSW turbine blade manufacturing.

Subsequently, testing was performed on actual blade sections at the Carbon Rivers blade laydown yard (https://www.carbonrivers.com/) to demonstrate the technologies and advancements that have occurred in NDE inspection techniques over the past decade.

For ultrasonic techniques, the viability of advanced ultrasonics such as full matrix capture (FMC) and the total focusing method (TFM) and FMC with planar wave in sonification (PWI) were evaluated. Ultrasonic techniques were deployed on blade sections at Carbon Rivers. For microwave testing, a frequency sweep antenna was employed with advanced software for the analysis of phase, imaginary, magnitude, and difference of the signals. The advanced analysis has the capability to identify different varieties of flaws and the technique was deployed on blade sections at Carbon Rivers.

This report documents the advancement of the techniques and will serve as a platform for the development of inspection methods for offshore wind turbine blades.

Keywords

Offshore wind

Wind turbine blades

Ultrasonic testing

Microwave testing

Fiberglass

Carbon fiber

CONTENTS

1 Introduction 1

2 NDE Techniques 2

2.1 Ultrasonic Techniques 2

2.2 Microwave Techniques 3

3 Summary of Technique Evaluation and Technical Development with Lab Specimens 7

3.1 Information About Samples for Preliminary Testing 7

3.2 Ultrasound Testing 122

3.3 Microwave Testing 177

3.3.1 Tabletop Test Results 18

3.3.2 Field Inspection Capability 20

4 Fabrication of Offshore Wind Samples 23

4.1 Overview 23

4.2 Summary of the Samples and Fabrication Process 244

4.2.1 Carbon pultrusion samples 244

4.2.2 Balsa core samples 255

4.2.3 Foam core samples 266

4.2.4 Porosity samples 277

4.2.5 Wrinkle samples 28

5 Testing of Offshore Wind Samples 29

5.1 Ultrasound 29

5.2 Microwave 344

5.2.1 CFRP sample 344

5.2.2 Samples with core material 344

5.2.3 Porosity samples 411

5.2.4 Wrinkle panel 433

6 Summary of Testing at Carbon Rivers 47

7 Summary of Test Results at Carbon Rivers 522
7.1 Testing of Advanced Ultrasound Techniques..... 522
7.1.1 Blade Section #2 54
7.1.2 Blade Section #4 55
7.1.3 Blade Section #7 56
7.2 Testing of Advanced Microwave Techniques..... 590
7.2.1 Blade Section #1 60
7.2.2 Blade Section #2 62
7.2.3 Blade Section #3 65
7.2.4 Blade Section #4 67
7.2.5 Blade Section #5 69
7.2.6 Blade Section #6 72
7.2.7 Blade Section #7 74

8 Summary and Conclusions 77

9 References 79

Appendix – Microwave Scan Results 80

LIST OF FIGURES

Figure 2-1. Material's frequency dependent variations. 4

Figure 3-1. REF-STD-C3-141-SNL plan photograph (top left), side photograph (top right), side sketch and legend, units in inches (middle) [2], plan view of defects units in inches (bottom) [2]. (1 in=25.4 mm)..... 8

Figure 3-2. WIND-7-110-SPAR-150 Spar Cap Isometric photographs. 9

Figure 3-3. Sample REF-STD-6-202-250-SXX-1. Photograph of the backside for the sample (top), plan view of the defect locations units in inches (middle) [2,3], elevation of the cross-section units in inches [2,3]. (1 in=25.4 mm)..... 9

Figure 3-4. REF-STD-7-214-265-SNL-1. Photograph of the backside for the sample (top), plan view of the defect locations units in inches (middle) [2,3], elevation of the cross section [2,3]. (1 in=25.4 mm)..... 10

Figure 3-5. REF-STD-3-126-176-TXX-1. Bottom side photograph (top), plan view of features embedded in the sample units in inches (middle) [3], sample elevation units in inches (bottom) [3]. (1 in=25.4 mm)..... 11

Figure 3-6. Probe paths overlaid upon the schematic of "REF-STD-C3-141-SNL" showing longitudinal paths in red and transverse paths in blue. Feature indications are labelled by flaw type. Note that the axis scales are not equal. (1 in=25.4 mm). 133

Figure 3-7. Cumulated PWI/TFM side view of "REF-STD-C3-141-SNL", scanned longitudinally by the 5MHz array to cover the features at the depth of 17.5mm. Feature indications are labelled by flaw type. Note that the axis scales are not equal..... 155

Figure 3-8. Cumulated PWI/TFM side view of "REF-STD-C3-141-SNL", scanned longitudinally by the 5MHz array to cover the features at the depth of 26.3mm. 166

Figure 3-9. Layer detail for "REF-STD-C3-141-SNL" with each layer measuring 5mm. 17

Figure 3-10. Inspection table and sample during inspection. 17

Figure 3-11. Composite Microwave Image (left) Illustrating Detection and Mapping of Flaws in the sketch of Ref-STD-6-202-250-SNL-1 (adapted from [3]). 19

Figure 3-12. Composite Microwave Image(left) Illustrating Detection and Mapping of Flaws in sketch Ref-STD-7-214-265-SXX-1 (right adapted from [3])..... 19

Figure 3-13. Scanning area using the MAPS scanner on sample Ref-STD-6-202-250-SNL-1..... 20

Figure 3-14. MAPS data for sample Ref-STD-6-202-250-SNL-1. 211

Figure 3-15. WIND-7-110-SPAR-150. Scanning with the MAPS (top left), isometric photograph of the part showing the curvature (top right), and data (bottom)..... 211

Figure 3-16. WIND-7-110-SPAR-150. Missing adhesive underneath the fiberglass piece. 22

Figure 3-17. Sample WIND-7-110-SPAR-150. Photograph of the top of the sample (top), C-scan data of the inspection with MAPS (middle), and data overlaid on top of photograph (bottom). 22
Figure 4-1. Fabrication of carbon pultrusion panels with five layers. Two layers of carbon (top left), five layers (top middle), inserts (top right), infusion (bottom left), curing (bottom middle), samples without drilled holes (bottom right). 24
Figure 4-2. Sketches of back-drilled holes on carbon panels. Diameter and depth of holes (left) and position of holes (right) (1 in. = 25.4 mm) 25
Figure 4-3. Photographs of carbon samples with back-drilled holes. 25
Figure 4-4. Eighteen-ply Balsa core GFRP samples. Sample 1 Layer 13 (top left), Layer 15 (top middle), Layer 17 (bottom left), Sample 2 Balsa core (bottom middle), finished samples (bottom right). 26
Figure 4-5. Foam core sample..... 27
Figure 4-6. Injection of air during infusion with a 20-cc syringe. 27
Figure 4-7. Porosity sample trial. Close up of induced porosity (left) and photograph of sample (right). 28
Figure 4-8. Plan view (left) and cross section view of the wrinkle panel (right). 28
Figure 5-1. Carbon fiber specimen manufacturing by TPI for UT scanning. The 5MHz phased array probe with Ultragel II couplant is shown atop the specimen towards the top left.. 29
Figure 5-2. Cumulated side view (left subplot) and end view (right subplot) of the FMC/TFM scan of the TPI sample at 5MHz..... 31
Figure 5-3. Cumulated side view (left subplot) and end view (right subplot) of the PWI/TFM scan of the TPI sample at 5MHz. 311
Figure 5-4. Cumulated side view (left subplot) and end view (right subplot) of the FMC/TFM scan of the TPI sample at 10MHz. The annotation lists void channels (VC) and flat-bottom holes (FBH). 322
Figure 5-5. Cumulated side view (left subplot) and end view (right subplot) of the PWI/TFM scan of the TPI sample at 10 MHz. The annotation lists void channels (VC) and flat-bottom holes (FBH). 322
Figure 5-6. Cumulated side view (left subplot) and end view (right subplot) of the PWI/TFM scan of the TPI sample at 5MHz. Scan taken “transversely”; that is, with the probe motion aligned to the second-longest dimension of the plate. The annotation lists void channels (VC) and flat-bottom holes (FBH). 333
Figure 5-7. Cumulated side view (left subplot) and end view (right subplot) of the PWI/TFM scan of the TPI sample at 5MHz. Scan taken from the face connected to the FBHs. 333
Figure 5-8. Bottom view (left) and side view (right) of the 50 mm (2 in.) thick balsa core sample. 355

Figure 5-9. Bottom view (left) and side view (right) of the 50 mm (2 in.) thick balsa core sample. 355
Figure 5-10. Lower GFRP samples compared to flaw locations. 366
Figure 5-11. Lower GFRP layer (1in.=25.4mm). 366
Figure 5-12. Lower GFRP layer compared to flaw locations. 377
Figure 5-13. Overlay of microwave image over panel. (1in.=25.4mm). 377
Figure 5-14. Ply Drop Detection. 38
Figure 5-15. Porosity foam flaw. 39
Figure 5-16. Pull-tab. 39
Figure 5-17. Pull-tab under bond paste. 40
Figure 5-18. Pull-tab. 40
Figure 5-19. Bond paste flaws. 41
Figure 5-20. Example of Frequency Image 11.56GHz (±2.3 GHz). 42
Figure 5-21. Depth Image with Possible Air Path. 42
Figure 5-22. Porosity versus Imaginary Data. 43
Figure 5-23. Wrinkle Panel Image. 44
Figure 5-24. Width Measurement. 45
Figure 5-25. Wrinkle height. 45
Figure 6-1. Aerial view of Carbon Rivers blade laydown yard in Kingston, TN. Credit: Google Earth 47
Figure 7-1. Photographed UT probes used in this work; from top left: (a) 0.5MHz monocrystal; (b) 1.0MHz monocrystal; (c) 2.25MHz phased array; (d) 5.0MHz phased array 54
Figure 7-2. Composited view of volumetric TFM data acquired from axial scan of Section #2, showing (a) top view; (b) side view and (c) end view 55
Figure 7-3. (a) Photograph from the end of Section #4 and (b) a corresponding annotated side view of volumetric TFM data captured by the 5MHz Imasonic probe 56
Figure 7-4. (a) Photograph from the end of Section #4 and (b) a corresponding annotated side view of volumetric TFM data captured by the 2.25MHz Olympus probe 56
Figure 7-5. Scanning area at the OD of Section #7. Suspected reflectors of interest are indicated by the two black arrows 57
Figure 7-6. Figure 7-6. Side views at (a) index=0.0in. and (b) index=12.0in., which slice the scan volume so at the locations of suspected reflectors of interest indicated in Figure 7-6, which are indicated by black arrows 58
Figure 7-7. (a) Photograph from the end of Section #7 and (b) a corresponding annotated side view of volumetric TFM data captured by the Imasonic 5MHz probe 58

Figure 7-8. End view of Section #7 composited from volumetric UT data acquired by (a) the Imasonic 5MHz probe and (b) the Olympus 2.25MHz probe 59
Figure 7-9. AMWI MAPS System in Use 59
Figure 7-10. Image of inspection zone 60
Figure 7-11. AMWI Microwave Inspection image overlay on part showing flaw location 61
Figure 7-12. Inspection cross section using Horizontal B identifying delamination at spar cap 612
Figure 7-13. Inspection Site 2 – Blade Root 622
Figure 7-14. Root Top view and cross section showing construction detail 633
Figure 7-15. Inspection Images with rounded indication mid stud 633
Figure 7-16. Cross section of root area 644
Figure 7-17. Section 3 Root with no studs 655
Figure 7-18. Root section with rounded indication 666
Figure 7-19. Mid span with internal reinforcement 67
Figure 7-20. Inspection image in plain view 68
Figure 7-21. Microwave inspection showing detection of flaws in bond paste levels 68
Figure 7-22. Carbon Fiber spar cap section 69
Figure 7-23. Plan and section detail of microwave inspection 70
Figure 7-24. Close up comparison of Horizontal B image and blade cross section 70
Figure 7-25. C Scan at depth showing detection of bond paste flaws at edge of carbon fiber 711
Figure 7-26. Blade trailing edge showing approximate location of internal edge of bond paste 72
Figure 7-27. Microwave C scan at depth shows ability to map edge of bond paste to validate proper squeeze out 733
Figure 7-28. Edge of blade repair section 744
Figure 7-29. Horizontal B image shows ability to detect and locate stacked flaws within part 755
Figure 7-30. Horizontal B image compared to part edge to validate ability for microwave imaging to track varying blade wall thickness in the presence of delamination 755

LIST OF TABLES

Table 3-1. Samples used for the preliminary assessment. 7
Table 3-2. Attributes for the phased array UT probes used to scan “REF-STD-C3-141-SNL”. (1 in=25.4 mm). 12
Table 3-3. Scan attributes for “REF-STD-C3-141-SNL”. (1 in=25.4 mm). 13
Table 3-4. Defect SNR for PWI/TFM scanning of “REF-STD-C3-141-SNL” arranged by scan ID and then by flaw. (1 in=25.4 mm). 14
Table 3-5. Summary of detection quality by flaw type. 15
Table 4-1. Summary of offshore wind blade samples. 23
Table 5-1. Attributes for the phased array UT probes used to scan the TPI carbon fiber samples (1 in. = 25.4 mm) 30
Table 5-2. Scan attributes for the TPI carbon fiber samples (1 in. = 25.4 mm) 30
Table 6-1. Sections used for NDE testing demonstration with flaws identified according to EPRI’s Blade Anomaly Dictionary 48
Table 7-1. Attributes for the conventional monocrystal UT probes used to assess UT performance and sound speed in the blade sections 53
Table 7-2. Phased array UT probe attributes used to scan the blade sections 53
Table 7-3. Summary of scan plans shown in this section 53

1 INTRODUCTION

With the increased size, design, and complexity of offshore wind blades, the development of non-destructive examination (NDE) strategies utilizing state-of-the-art technologies is critical to create opportunities for proactive blade maintenance. For offshore wind power, the blades play an important role in the performance and reliability of the overall system making it is necessary to develop and further advance techniques that can support the safe and reliable operation of wind turbine blades, especially in an offshore environment.

This report summarizes the exploration and evaluation of ultrasonic and microwave testing techniques for the purposes of identifying flaws in offshore wind turbine blades. The evaluation of these techniques was first performed with mockup samples which were utilized in previous wind power research projects. Subsequently, the advancement of the NDE and flaw detection techniques was achieved through the testing of actual blade sections at the Carbon Rivers (CR) Powerhouse blade laydown yard. The results from this report are built to serve as a baseline towards the evaluation of blade issues (such as manufacturing flaws or damages from transportation/service) which are specific to offshore wind blades and fabricated as part of this project.

Advancements in data collection and analysis have been achieved with the use of ultrasonic and microwave NDE techniques. These advancements can support the inspection of wind blades in a quality control setting during fabrication and can potentially be deployed in the field for pre-commissioning inspections as more portable versions of these techniques become available.

2 NDE TECHNIQUES

The inspection of wind turbine blades is a challenging task due to the composition and materials used for the fabrication of the components. To address these challenges, the use of ultrasonic and microwave technique can allow for the inspection of components given that they are used for specific materials. For the inspection of carbon fiber reinforced polymer (CFRP) components, ultrasonic methods are better suited for an evaluation of the material. In the case of glass fiber reinforced composites (GFRC), the use of microwave testing is likely better suited given the properties of the material and the nature of the physics used for testing. A summary of the ultrasonic and microwave methods used in this project is presented in report Sections 2.1 and 2.2, respectively.

2.1 Ultrasonic Techniques

Ultrasonic techniques (UT) are widely used across multiple industries for volumetric inspection, material characterization and component monitoring. UT is a potential candidate for integrity assessment of offshore wind turbine blades. Aided by many decades of research and development, UT for industrial purposes is relatively cheap, quick, non-hazardous, easily interpretable and with good availability of instrumentation and sensors commercially available.

In the simplest common implementation of UT, a piezoelectric sensor converts electrical energy to physical deformation and vice versa. The frequency of insonification, for industrial purposes, is typically in the range 500kHz to 10MHz. The transducer can act as both transmitter and receiver by the same physical principle of an active sonar. The received signal is interpreted with each reflection indicating the presence of some component geometry or discontinuity in the propagating material along the principal direction of the sonic energy.

Some natural deficiencies of contact UT are that it requires good coupling, good surface contact and a clear line of sight through the propagating medium to the region of interest. In materials unfavorable to ultrasound, the energy is prone to attenuation and/or scattering or redirection of the energy that make interpretation difficult or unreliable, even to very experienced practitioners.

In all UT applications, the physical principle is the same: Ultrasonic energy propagates through a clean bulk material without reflecting. When the same energy encounters a change in acoustic impedance, part of the energy is scattered in an amount determined by its characteristics such as acoustic impedance, orientation, size and other physical attributes. The transceiver records the scattered energy. Extensive academic research involving modelling and simulation, combined with improvements in imaging and image analysis, have offered potential for characterization of each indication in addition to mere detection.

Towards the end of the last century, the advent of probes comprising arrays, as opposed to just one, facilitated electronically-controlled steering and focusing abilities, allowing for even quicker acquisition of the examination volume with the potential sharper focusing. Corresponding procedures were developed to accommodate the new technology and methods.

In the decades that followed the common use of phased arrays in modern NDE, the foundation was laid for a further development in UT, in conjunction with rapid recent increases in both general computing power and the availability of high capacity data storage. One such example is the introduction of the Full Matrix Capture (FMC) for acquisition, involving insonification in such a manner than requires a further step of synthetic focusing (using a synthetic beamformer) to reconstruct the volume. If said beamformer steers and focuses everywhere in the reconstruction volume, then this process is generally known as the Total Focusing Method (TFM) and the entire process is often referred to as FMC/TFM.

There are several common variations of FMC acquisition: If transmitting apertures comprise one element only, then this is called elementary FMC (or sometimes just “FMC”). If the transmitting aperture comprises multiple elements and they are phased so as to generate planar waves in the specimen, this is known as Planar Wave Insonification (PWI) and the entire process is correspondingly known as PWI/TFM. Further variation of PWI involves generation of waves that are not planar: They may be diverging, converging or more irregular, depending on the acquisition and focusing needs. The EPRI report #3002015971 provides a summary of FMC, TFM and its variants [1].

In contrast to Conventional Phased Array (CPA), TFM requires a distinct additional step after acquisition, to carry out the focusing via the synthetic beamformer. However, contemporary instrumentation is powerful enough for real-time TFM focused from either elementary FMC or PWI, although PWI is faster.

In this report, we will demonstrate the viability of FMC/TFM and PWI/TFM in application to composite structures, reference standards of multi-layered structure with artificial defects.

2.2 Microwave Techniques

Microwave inspection of composites was theorized in papers and articles as early as the 1960’s. The underlying physics of the interaction of electromagnetic radiation (EMR) with materials was well understood by this time, and this lent itself to realizing the potential for its application in the inspection industry.

Microwave inspection of composites involves using microwave radiation to detect and analyze defects or anomalies in composite materials. It typically works by transmitting microwave signals into the material and measuring the reflected or transmitted signals. This technique is now commonly used for non-destructive testing (NDT) in multiple industries, including petrochemical and aerospace.

The principles of microwave inspection of composites are based on when a non-magnetic material is exposed to EMR in the microwave frequency range, it will reflect a signal based on the material's complex permittivity. The reflected signal will be different for materials with different dielectric properties. The dielectric properties of materials are a complex value composed of two components. The first is the material's ability to store electrical energy in the presence of an electric field. When referenced to a vacuum's ability to store electrical energy under the same conditions, this first component is referred to as the material's dielectric constant.

The second component represents the amount of electromagnetic energy the material dissipates, called dielectric loss. The dielectric loss is typically quantified as the angle of the phasor in the complex plane of the real and imaginary component of the complex permittivity. This becomes the loss angle or, because this angle is usually small, the loss tangent.

The complex permittivity of a material varies with both frequency and temperature. The most common cause of temperature dependence in composite materials, like glass fiber reinforced polymer (GFRP), is that the material undergoes phase transitions at specific temperature ranges. These transitions can dramatically alter the electrical properties of the material. Some composite materials may also undergo relaxation processes involving molecular or atomic rearrangements with temperature changes. These relaxation processes can affect the dielectric properties, causing temperature-dependent variations in ε' and ε". In this case, the materials under test (MUT) are inspected at normal outdoor or indoor environmental conditions, which are away from any phase transition or atomic rearrangement temperature so that the dielectric properties can be treated as temperature-independent for our purposes.

The complex permittivity of the MUT is also frequency-dependent, as noted above. This means some flaws or material combinations may be more or less responsive to a specific range of frequencies, returning a higher or lower signal magnitude. This particular aspect of any inspection is investigated and incorporated into the inspection procedure during the development phase of the methodology. In many instances, this variability can be used strategically to enhance the ability to detect specific material or flaw characteristics. Figure 2-1 shows a typical material's frequency-dependent variations in ε' and ε" and where specific material-to-EMR interaction mechanisms become more or less critical.

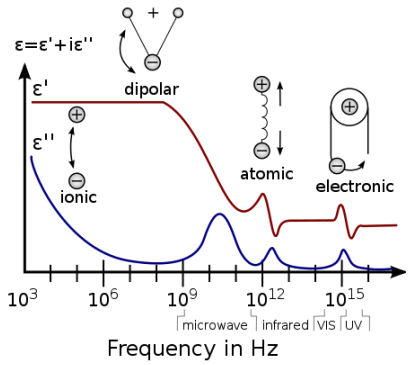

Figure 2-1. Material's frequency dependent variations.

Using the EMR interaction with material as an inspection tool provides specific opportunities to detect flaws. This is because, in most composite materials, the complex permittivity of the composite material differs substantially from the complex permittivity of flaws. In the case of a delamination within the GFRP material, the delamination would be filled with either air or a vacuum, depending on the location of the delamination. The dielectric constant in this case, would be 1, compared to the dielectric constant of the GFRP, which is 4.4. This contrast is sufficiently large to result in a reflected signal at the delamination that allows it to be easily discriminated from the rest of the GFRP.

Another key feature of using EMR for inspections is that EMR is air coupled to the material and does not require a liquid or gel couplant to provide efficient energy transfer into the MUT. This simplifies inspections and allows the inspection to occur without the antenna contacting the MUT. Using a non-contact method increases inspection speed and eliminates inspection issues that minor surface irregularities might cause. It also allows the sensors to be mounted on robotic arms and other advanced scanners that can inspect curved and sloped geometries more efficiently than traditional scanners.

Another important by-product of the air-coupled method is that the EMR beam does not stop at an internal air or vacuum interface, such as a delamination. This means that details from the inspection may be available beyond internal flaws, including delamination. Significant differences in the material's impedance properties do not result in a complete reflection of the EMR, as is common in other methods. This allows for the complete inspection of a structure that contains multiple materials, such as GFRP with foam or balsa core. This is a significant advantage when inspecting complex structures, such as wind turbine blades, commonly constructed of multiple materials.

Microwave inspection is limited to the inspection of materials that are non-magnetic and non-conductive and cannot inspect metals or conductive materials. Conductive materials cause a reflection of the EMR at the surface and do not provide any volumetric information past a very shallow skin effect. This includes materials that are conductive in multi-directions, such as thick carbon fiber composites (CFRP). More traditional inspection methods, such as ultrasonic inspections, are helpful for those materials.

Early iterations of the microwave method involved using a single frequency to interrogate the MUT. Advancements in technology have improved the microwave methodology by using a frequency sweep over a specific range of frequencies to provide the best signal-to-noise ratio for the MUT. This methodology change enhances the inspection in the following ways:

- Sweeping the frequency range improves the probability of detection by increasing the number of frequencies that might interact with the MUT and flaws
- Collecting data over a range of frequencies allows for changing the domain of the dataset from frequency to time using an Inverse Fast Fourier Transform (IFFT), thus providing access to signal amplitude versus time of flight or depth within the MUT

The improved microwave methodology also uses an advanced microwave inspection antenna versus the “open waveguide” or broadcast antenna systems. The antenna is purposely designed to allow broadband broadcast into the MUT while controlling the spot size of the EMR injected into the MUT. This provides for a more accurate time of flight conversion and better feature resolution in the MUT.

The software used for analysis has been modified to work with the data acquisition system and provides improved imaging and location features in comparison to previous versions. the latest version of the software includes 3D rendering capabilities of the data. The software also includes a radar synthetic aperture focusing (SAFT) technique as an added feature for better resolution.

3 SUMMARY OF TECHNIQUE EVALUATION AND TECHNICAL DEVELOPMENT WITH LAB SPECIMENS

This section presents a brief description of the samples used for the preliminary evaluation and a summary of the UT and MW techniques deployed in some of the samples. The samples used for this preliminary evaluation include fiberglass and carbon fiber materials. These samples have similar characteristics to what can be found OSW blades and the sole purpose of inspecting the samples is to demonstrate the capability of tools available in the market to inspect the materials. Further, the results from this technique evaluation will serve as a platform for development of the techniques in samples fabricated with materials and characteristics of OSW blades.

3.1 Information About Samples for Preliminary Testing

Four samples loaned from Sandia National Laboratories (SNL) were used during the preliminary assessment of the UT and MW techniques. A list of the samples and general information is included in Table 3-1. The UT and MW sections will include information about test testing section for the samples tested.

Table 3-1. Samples used for the preliminary assessment.

Sample ID	Reference	Report Figure	Material	General description (technique)
REF-STD-C3-141-SNL	[2]	3-1	Carbon fiber	Carbon spar cap (UT)
WIND-7-110-SPAR-150 Spar Cap	[2]	3-2	Fiberglass	Spar cap and shear web (MW)
REF-STD-6-202-250-SXX-1	[2,3]	3-3	Fiberglass	Spar cap and shear web (MW)
REF-STD-7-214-265-SNL-1	[2,3]	3-4	Fiberglass	Spar cap and shear web (MW)
REF-STD-3-126-176-TXX-1	[4,2]	3-5	Fiberglass	Spar cap and shear web (MW)

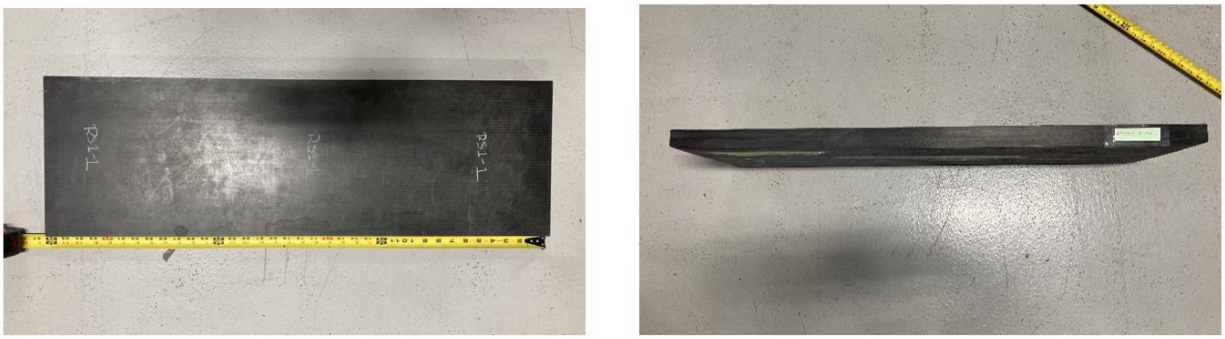

Plan and side photograph

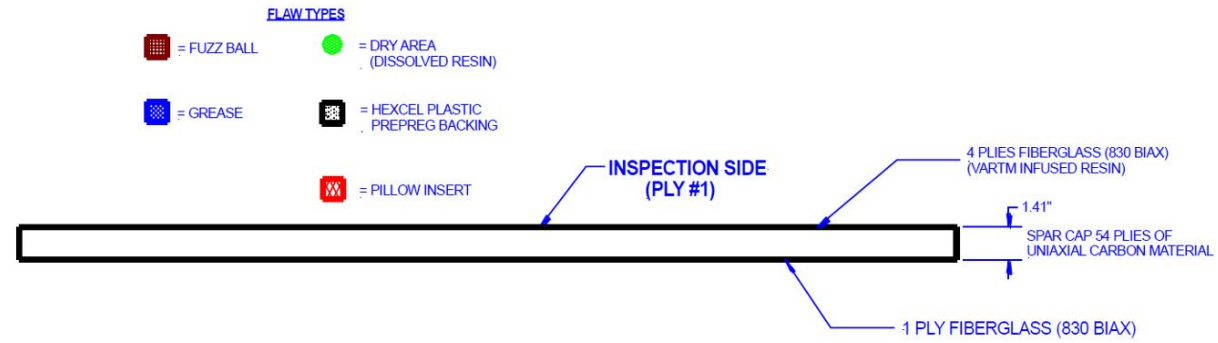

Elevation and defect legend

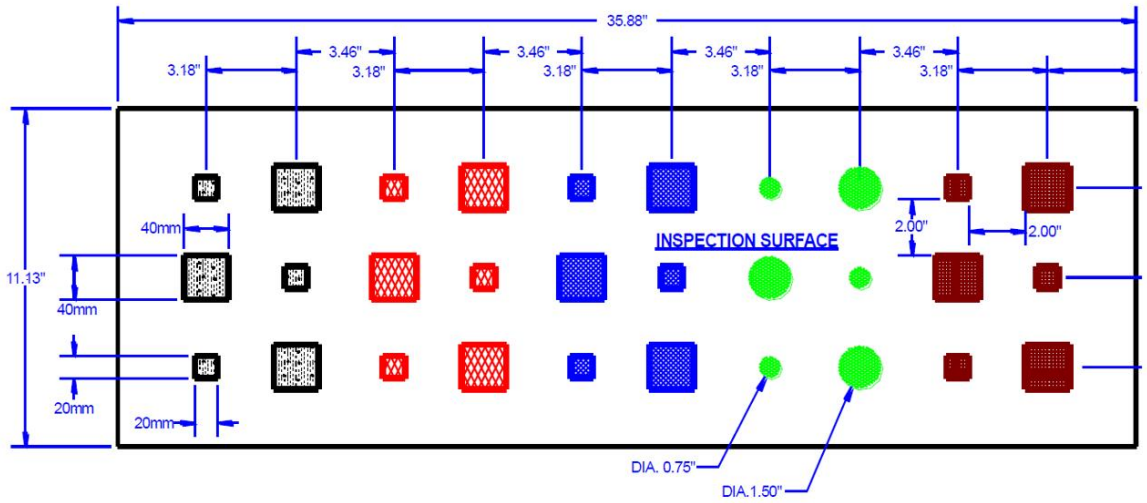

Figure 3-1. REF-STD-C3-141-SNL plan photograph (top left), side photograph (top right), side sketch and legend, units in inches (middle) [2], plan view of defects units in inches (bottom) [2]. (1 in=25.4 mm).

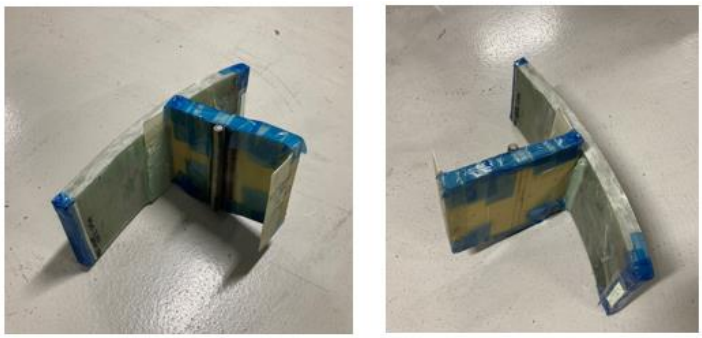

Figure 3-2. WIND-7-110-SPAR-150 Spar Cap Isometric photographs.

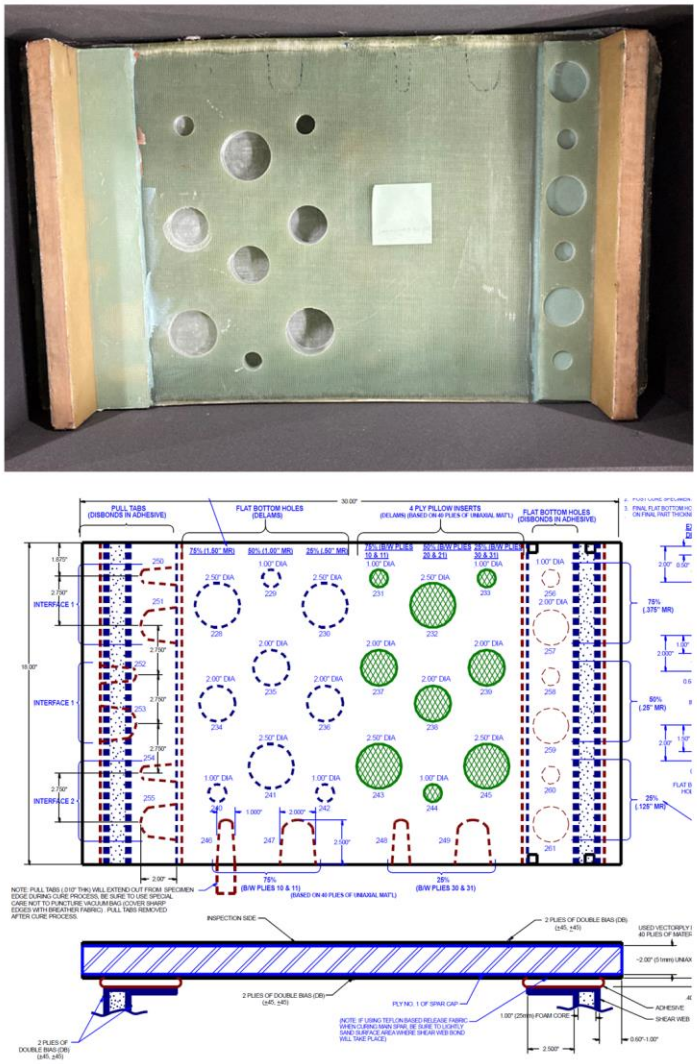

Figure 3-3. Sample REF-STD-6-202-250-SXX-1. Photograph of the backside for the sample (top), plan view of the defect locations units in inches (middle) [2,3], elevation of the cross-section units in inches [2,3]. (1 in=25.4 mm).

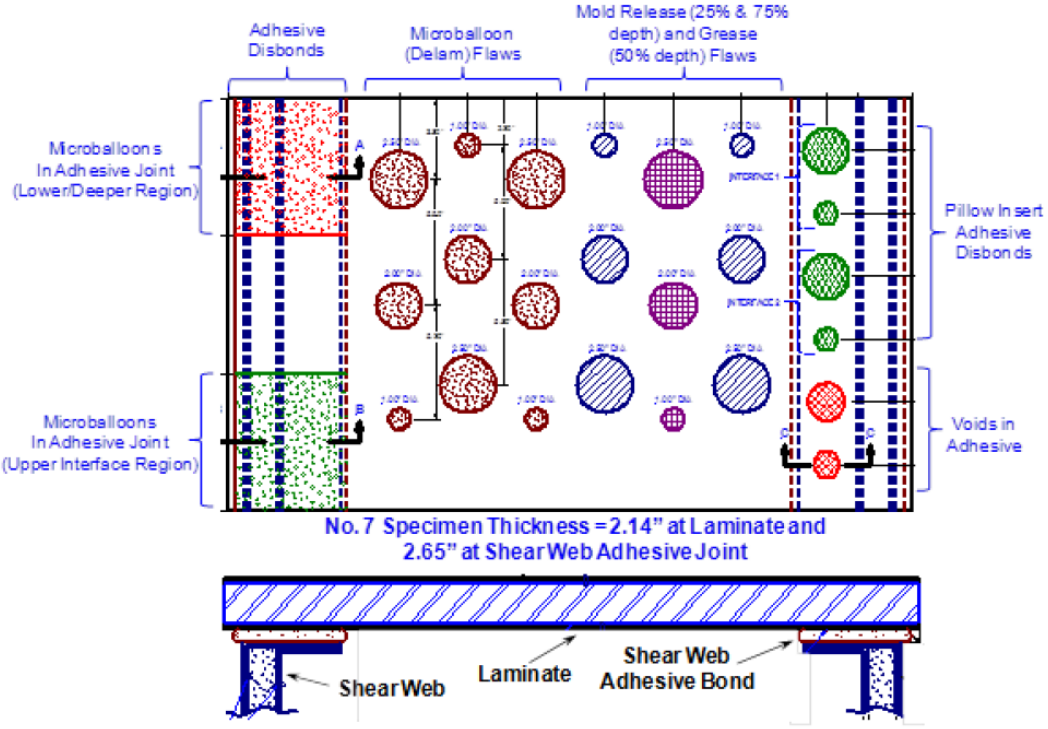

Figure 3-4. REF-STD-7-214-265-SNL-1. Photograph of the backside for the sample (top), plan view of the defect locations units in inches (middle) [2,3], elevation of the cross section [2,3]. (1 in=25.4 mm).

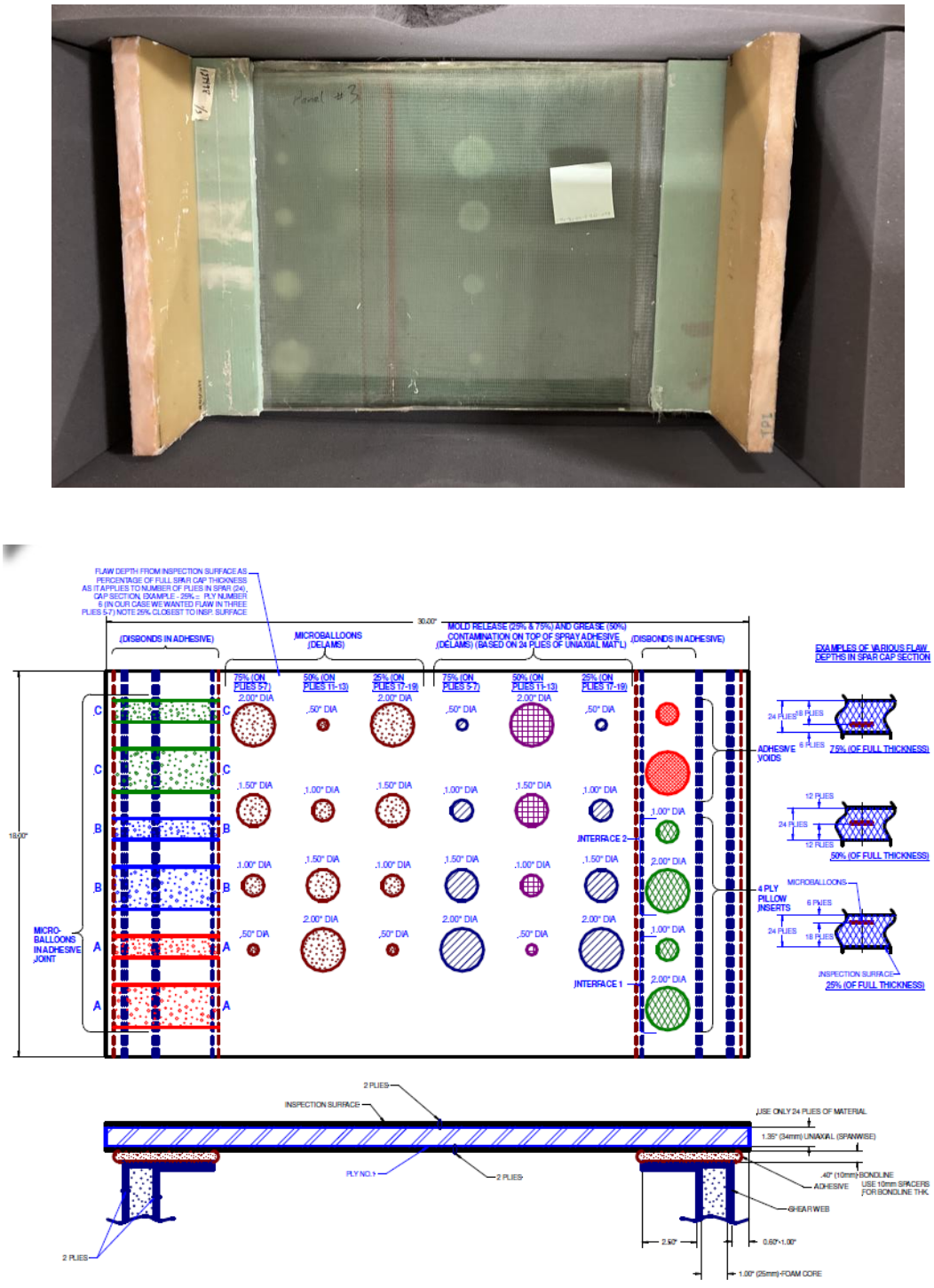

Figure 3-5. REF-STD-3-126-176-TXX-1. Bottom side photograph (top), plan view of features embedded in the sample units in inches (middle) [3], sample elevation units in inches (bottom) [3]. (1 in=25.4 mm).

3.2 Ultrasound Testing

The sample “REF-STD-C3-141-SNL” was selected for volumetric UT scanning for its rich variety of internal and embedded features that are representative of some typical manufacturing deficiencies. The sample measures 911×290×35 mm (35.9×11.4×1.38 in.) and the longitudinal sound speed is determined to be 2600 m/s (8530 ft/s).

The five types of artificial defects included: hexcel plastic (HP), pillow insert (PI), grease (GR), dry area (DA), fuzz ball (FB). The defects and are arranged at three depths, namely 8.9, 17.5, and 26 mm (0.35, 0.69, 1.02 in.), throughout the thickness and in two different dimensions of 20.0, and 40.0 mm (0.79, and 1.57 in.). The range of sizes and depths of the defects would offer some insight into their effects upon the performance of the UT techniques.

The UT instrument used was the Zetec Emerald 64/128, a device capable of FMC and PWI acquisition and real-time TFM display. Two different phased array probes were used to acquire data with the sensor in direct contact with the specimen. Their attributes are listed in Table 7-. Ultrasonic acquisitions were carried out in elementary FMC and in PWI. The latter was done with angular sweeping from -20° to 20° in 5° increments. Coupling between the probe and the specimen was done by Ultragel II.

Table 3-2. Attributes for the phased array UT probes used to scan “REF-STD-C3-141-SNL”. (1 in=25.4 mm).

Probe ID	**1-11506-1060**	**13493-1011**
Centre Frequency	5.0MHz	10.0MHz
Element Count	64	128
Pitch	0.6mm	0.3mm
Elevation	10.0mm	10.0mm
Pulse Width	100ns	50ns
Active Aperture	38.4mm	19.2mm

The scan performed using the 5 MHz probe are listed in Table 3-3 and the probe motion paths are illustrated in Figure 3-6 overlaid upon the specimen schematic., The applied hard gain was 45dB for all scans and the TFM reconstruction was carried out within a 40×40 mm (1.6 x 1.6 in.) plane centered beneath the middle of the array aperture, and with the top of the region of the interest touching the interface between the probe and the specimen.

Table 3-3. Scan attributes for “REF-STD-C3-141-SNL”. (1 in=25.4 mm).

Scan ID	Acquisition Type	Scan Orientation	Defect Type(s)	Reconstruction Volume Dimension
FMC_L0	FMC	Longitudinal	*All*	(40×40×870)mm
FMC_L1	FMC	Longitudinal	*All*	(40×40×870)mm
FMC_T1	FMC	Transverse	HP	(40×40×230)mm
PWI_L0	PWI	Longitudinal	*All*	(40×40×870)mm
PWI_L1	PWI	Transverse	*All*	(40×40×870)mm
PWI_T1	PWI	Transverse	HP	(40×40×230)mm
PWI_T2	PWI	Transverse	PI	(40×40×230)mm
PWI_T4	PWI	Transverse	GR	(40×40×230)mm
PWI_T6	PWI	Transverse	DA	(40×40×230)mm
PWI_T8	PWI	Transverse	FB	(40×40×230)mm

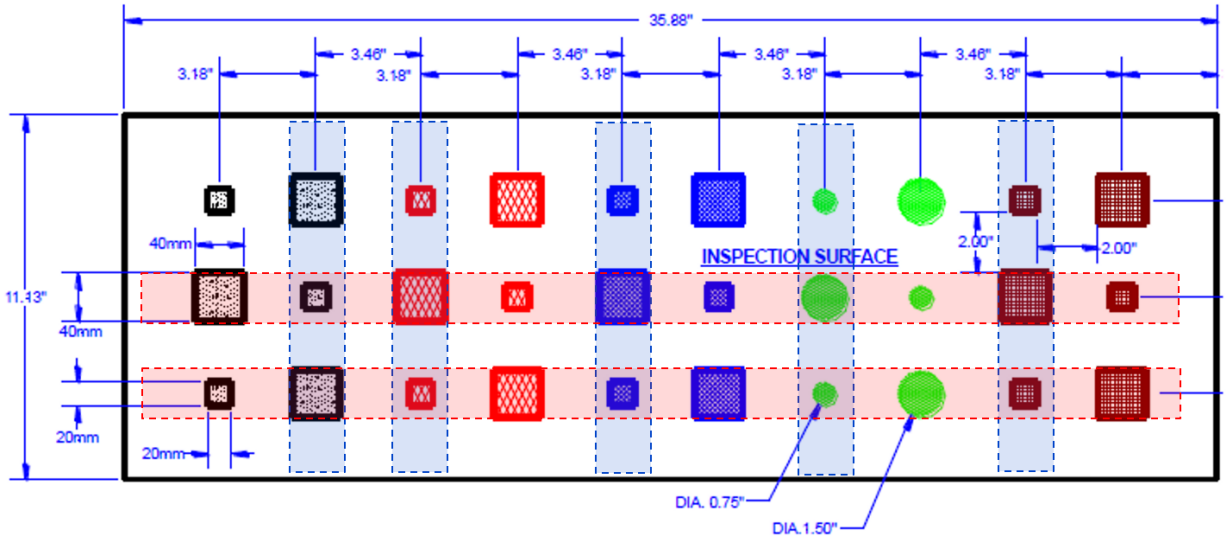

Figure 3-6. Probe paths overlaid upon the schematic of “REF-STD-C3-141-SNL” showing longitudinal paths in red and transverse paths in blue. Feature indications are labelled by flaw type. Note that the axis scales are not equal. (1 in=25.4 mm).

The Signal-to-Noise (SNR) ratio is quantified for the flaws that are visible within each probe path, considering the background noise within a bounding box at a depth proximate to the bounding box that encapsulates the flaw. The resulting values, sourced from PWI acquisition, are tabulated in Table 3-4 and are arranged firstly by scan ID (as described in Table) and then by defect. The overall detectability of the flaws, from a qualitative perspective, is summarized in

Table 3-5 according to flaw type and scan type.

Table 3-4. Defect SNR for PWI/TFM scanning of "REF-STD-C3-141-SNL" arranged by scan ID and then by flaw. (1 in=25.4 mm).

Scan ID	Defect			Statistics				
	Type	Dimension	Depth	Max Signal	Max Noise	Mean Noise	Max SNR	Mean SNR
PWI_L0	HP	40mm	17.5mm	64.7%	14.1%	2.2%	13.3dB	29.4dB
		20mm		70.3%	20.8%	2.7%	10.6dB	28.4dB
	PI	40mm		97.9%	24.1%	3.2%	12.2dB	29.7dB
		20mm		89.9%	18.2%	2.3%	13.8dB	31.6dB
	GR	40mm		63.9%	18.2%	1.7%	13.3dB	31.3dB
		20mm		40.0%	14.1%	2.3%	9.1dB	24.7dB
	DA	40mm		31.2%	17.9%	2.3%	4.9dB	22.1dB
		20mm		36.5%	24.1%	2.6%	3.6dB	23.0dB
	FB	40mm		53.0%	19.1%	2.6%	8.9dB	26.1dB
		20mm		35.8%	10.1%	1.4%	11.0dB	28.2dB
PWI_L1	HP	20mm	26.3mm	40.4%	6.3%	1.2%	11.9dB	30.3dB
		40mm		25.9%	5.0%	1.0%	12.2dB	28.4dB
	PI	20mm		28.3%	5.0%	0.9%	15.0dB	29.8dB
		40mm		20.6%	9.8%	1.0%	6.4dB	25.8dB
	GR	20mm		13.5%	6.4%	0.9%	6.5dB	23.2dB
		40mm		19.1%	7.2%	1.2%	8.5dB	24.4dB
	DA	20mm		19.1%	9.4%	1.4%	6.1dB	22.8dB
		40mm		21.3%	5.6%	1.0%	11.6dB	26.8dB
	FB	20mm		17.9%	7.3%	1.1%	7.8dB	24.0dB
		40mm		17.8%	4.9%	0.8%	11.1dB	26.7dB
PWI_T1	HP	40mm	26.3mm	16.1%	4.1%	0.8%	12.0dB	26.3dB
		20mm	17.5mm	38.4%	12.8%	1.7%	9.5dB	27.1dB
		40mm	8.9mm	69.8%	33.9%	6.1%	6.3dB	21.2dB
PWI_T2	PI	20mm	26.3mm	12.4%	4.0%	0.7%	9.9dB	24.6dB
		40mm	17.5mm	49.7%	6.5%	1.2%	17.6dB	32.0dB
		20mm	8.9mm	61.0%	21.2%	4.2%	5.8dB	23.2dB
PWI_T4	GR	20mm	26.3mm	8.8%	4.2%	0.8%	6.4dB	20.4dB
		40mm	17.5mm	30.9%	10.7%	1.6%	9.3dB	25.6dB
		20mm	8.9mm	54.1%	43.0%	5.5%	2.0dB	19.8dB
PWI_T6	DA	20mm	26.3mm	11.3%	5.4%	0.9%	6.4dB	21.5dB
		40mm	17.5mm	20.5%	10.0%	1.8%	6.2dB	20.9dB
		20mm	8.9mm	48.9%	48.4%	7.0%	0.1dB	16.8dB
PWI_T8	FB	20mm	26.3mm	8.0%	4.1%	0.7%	5.8dB	20.7dB
		40mm	17.5mm	25.4%	6.4%	1.3%	11.9dB	25.7dB
		20mm	8.9mm	54.4%	36.5%	6.7%	3.5dB	18.2dB

Table 3-5. Summary of detection quality by flaw type.

Flaw type	Longitudinal scan	Transverse scan
HP	Strong	Strong
PI	Strong	Strong
GR	Moderate	Moderate
DA	Moderate	Weak
FB	Moderate	Weak

The cumulated side view of the longitudinal PWI/TFM scans (the orientation that captures all the flaws in the same scan) are shown in 3-7 and 3-8 for the middle row of defects and lower row of defects, respectively. Note that in these figures, the first 8mm depth of the specimen is not reconstructed.

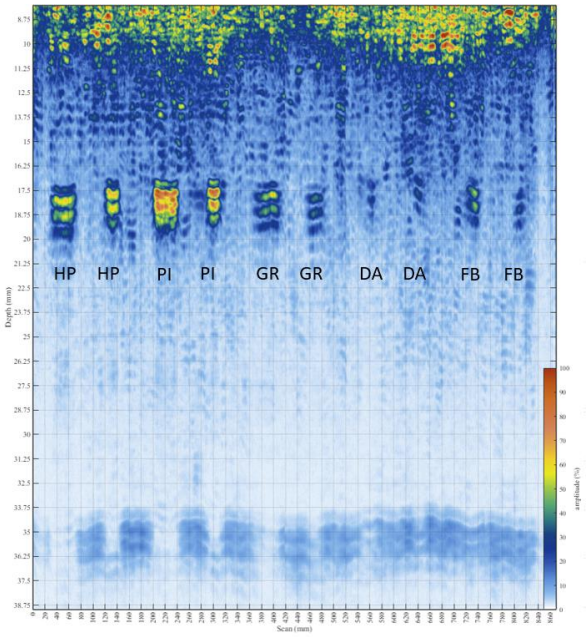

Figure 3-7. Cumulated PWI/TFM side view of "REF-STD-C3-141-SNL", scanned longitudinally by the 5MHz array to cover the features at the depth of 17.5mm. Feature indications are labelled by flaw type. Note that the axis scales are not equal.

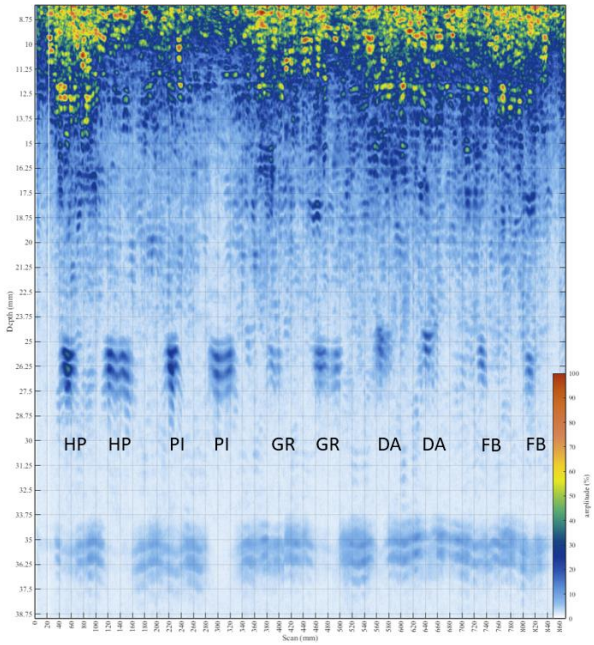

Figure 3-8. Cumulated PWI/TFM side view of "REF-STD-C3-141-SNL", scanned longitudinally by the 5MHz array to cover the features at the depth of 26.3mm.

In the longitudinal scans, all defect types were successfully detected with SNR of 6dB or higher, except for dry areas. In transverse scans, most defect types were successfully detected with SNR of 6dB or higher, though many of the flaws that were closest to the top surface had a SNR lower than 6dB due to poorer ability to focus within the near field of the array. The greases and fuzz balls were also difficult to detect strongly at greater depths.

There are some key observations which will impact the development of the UT technique:

- There was a noticeable difference in detectability with respect to the orientation of the phased array probe, which was confirmed by experimental observation in real-time scanning. The stronger detection was observed when the array elevation was oriented along the longest dimension of the specimen. The arrays used in this study have a significant elevation and the noticed difference may result from material inhomogeneity due to the specimen's composite structure, either within the plies or in terms of its bonding method. The EPRI UT technique should consider array orientation in the development process;

- There was a significant volume within the first 5mm depth that was saturated with noise and made difficult the identification of the flaws that were closest to the top surface. The use of a zero degree wedge would certainly have a mitigating effect although would introduce the presence of internal wedge reflections. The thickness of said wedge is a key parameter which must be selected in consideration of the thickness of the overall specimen;

- The layers between the plies were easily visible to the eye (see Figure 3-9) but were not observed at all in the ultrasonic images even where focusing was applied in the TFM reconstruction. It would be concluded that the interlayer bonding is strong and even.

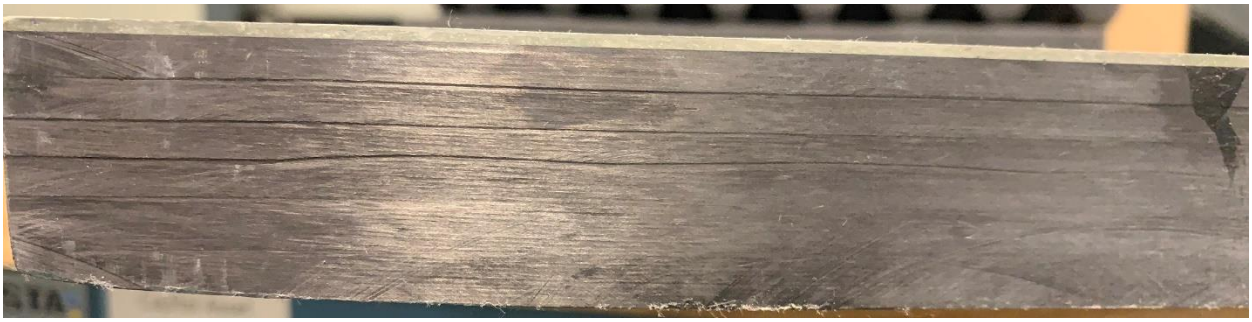

Figure 3-2. Layer detail for "REF-STD-C3-141-SNL" with each layer measuring 5mm.

3.3 Microwave Testing

The GFRP samples identified in Section 3.1 were initially inspected using the microwave inspection stationary table scanning system, Figure 3-10. The system uses a vector network analyzer (VNA) and proprietary inspection antenna system to acquire data over a specific range of user-selectable frequencies, but they must match the range of the selected antenna.

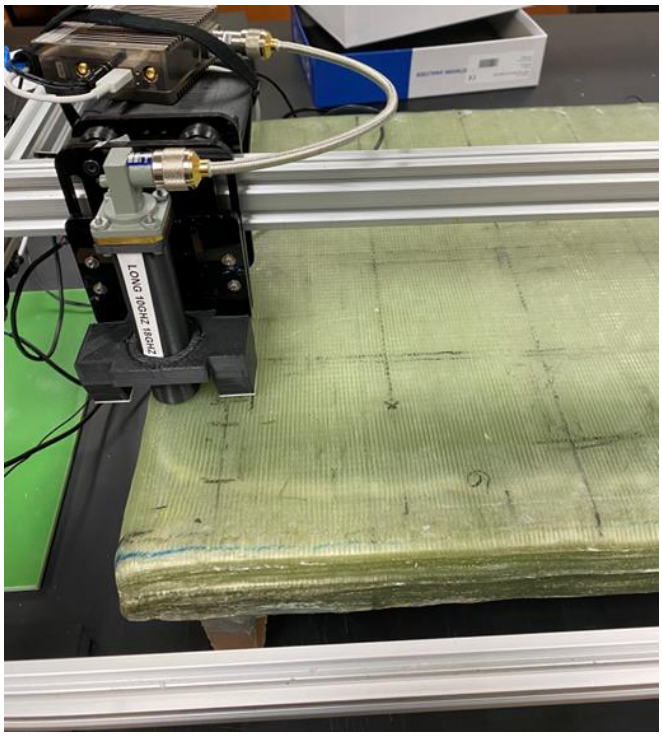

Figure 3-3. Inspection table and sample during inspection.

This system provides the ability to inspect with frequency ranges from 6 GHz to 14 GHz and from 10 GHz to 18 GHz or any subset of these ranges. The frequency range is selected based on the material to be inspected and on a balance between penetration requirements and resolution.

3.2.1 Tabletop Test Results

The initial scan set-up was as follows:

Ref-STD-6-202-250-SNL-1 and Ref-STD-7-214-265-SXX-1

- Initial scan using the Tabletop Scanning system
- Frequency Range 10GHz-18GHz
- 201 Data Points
- 10mm by 10mm (0.39 in. by 0.39 in) scan/index and 5mm by 5mm (0.20 in by 0.20 in) scan/index
- Sample 680mm by 430mm (26.8 in by 16.9 in). In some cases, the sample was split into two scans to accommodate SAR software)
- Scan time is approximately 15 minutes (10 by 10) and 30 minutes (5 by 5)
- No couplant required (Air coupled)

The inspection aimed to detect and map as many flaws as possible in the samples. To do this, the complete data sets available were processed in the a proprietary software: Real, Imaginary, Magnitude, Phase, and Difference (Only in SAR software). The data was imaged using both the IFFT (Time of Flight) and Synthetic Aperture Radar modes to provide a range of data visualization techniques.

The findings were compared to the sample drawings to determine which flaw types were detectable. A secondary result was to compare the findings to the other NDT result methods published in the Sandia Report SAND2014-16965[5].

Using the available data and imaging techniques, all the flaws embedded in both samples were successfully detected and mapped for the initial inspection phase. Images were created from a composite of the methods to detail the entire sample. The figures illustrate the successful detection and mapping of the flaws in the two samples from the composite images. A summary of the results is presented in figures 3-11 and 3-12.

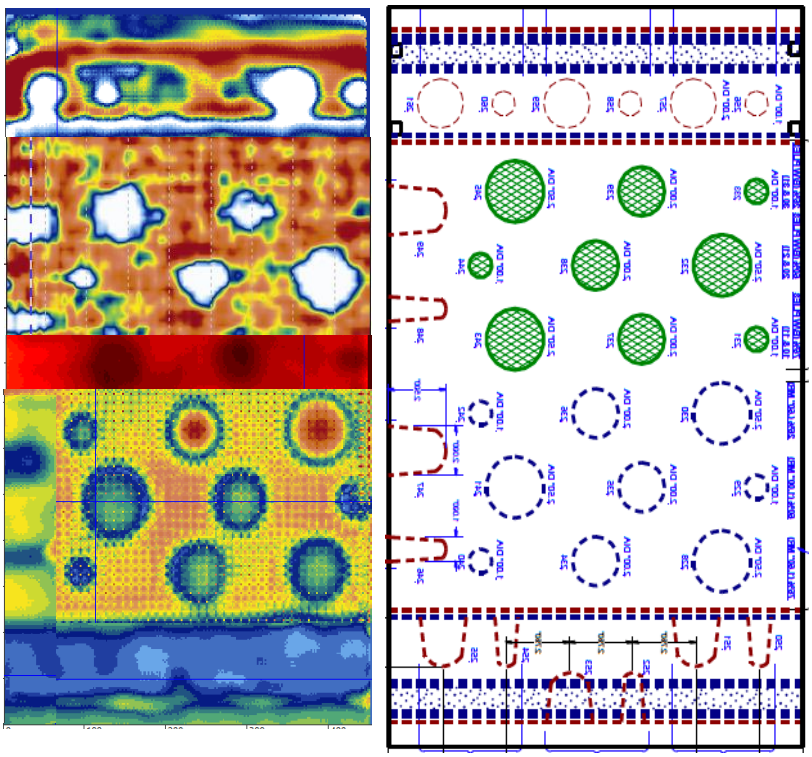

Figure 3-4. Composite Microwave Image (left) Illustrating Detection and Mapping of Flaws in the sketch of Ref-STD-6-202-250-SNL-1 (adapted from [3]).

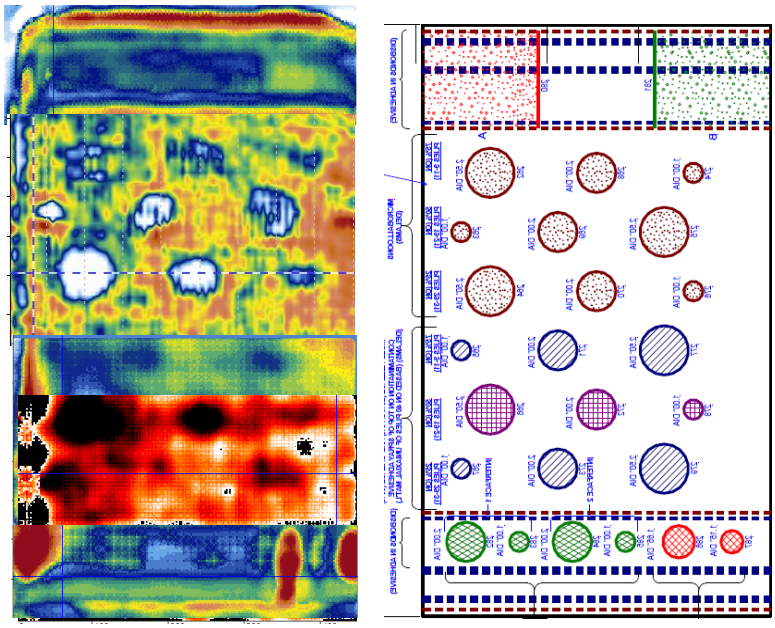

Figure 3-5. Composite Microwave Image(left) Illustrating Detection and Mapping of Flaws in sketch Ref-STD-7-214-265-SXX-1 (right adapted from [3]).

The flaws in Ref-STD-7-214-265-SXX-1 were more difficult to detect overall than the flaws in Ref-STD-6-202-250-SNL-1. This is the result of the nature of the flaws that were used in making Ref-STD-7-214-265-SXX-1 . More detail on the inspection results is available in Appendix A,

3.2.2 Field Inspection Capability

To evaluate the ability to inspect wind turbine blades in field settings, an inspection was carried out using the Motorized Axis Portable Scanner (MAPS) system. A simple scan of Ref-STD-6-202-250-SNL-1was made as a comparison to the large scanning platform system results.

The MAPS uses a scan axis with a stepper motor to control the distance moved in that axis. It is manually moved in the Index axis, and those movements are recorded via an encoder attached to the system. The MAPS is shown on Ref-STD-6-202-250-SNL-1 in Figure 3-13. The red box is the inspection area covered in this inspection.

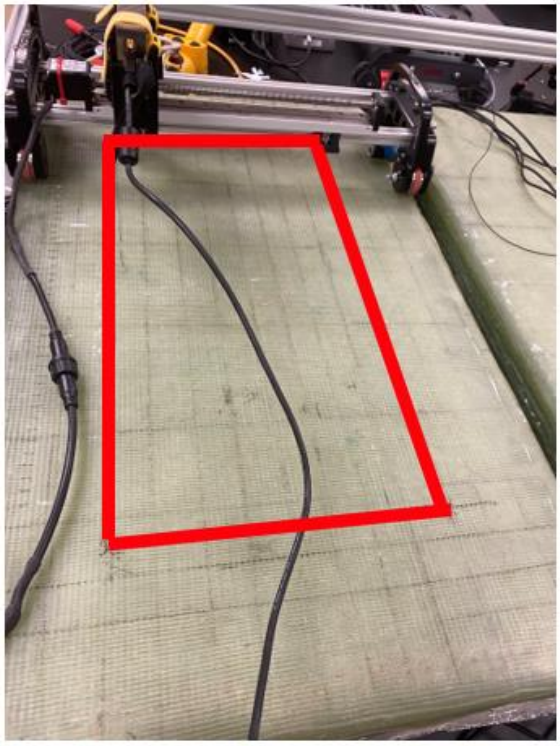

Figure 3-6. Scanning area using the MAPS scanner on sample Ref-STD-6-202-250-SNL-1.

The inspection results show the level of detail possible with a field inspection. The image is directly correctable to the full-scale inspection system image. The image below shows a sample of the inspection data using Synthetic Aperture Focusing and the part drawing.

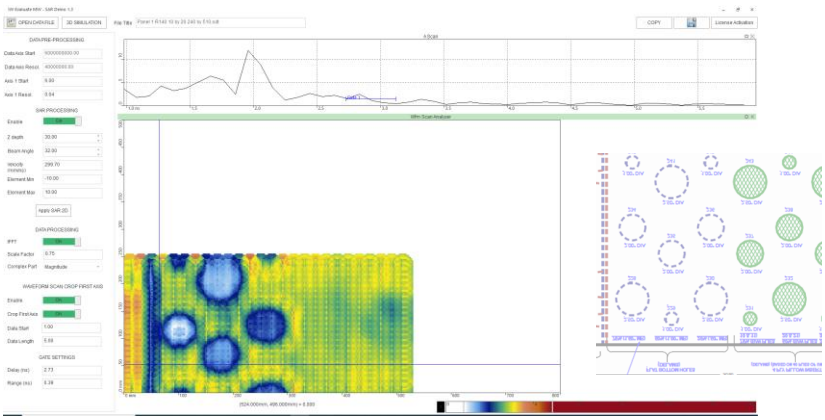

Figure 3-7. MAPS data for sample Ref-STD-6-202-250-SNL-1.

Because the size and curvature of sample WIND-7-110-SPAR, this part could not be inspected using the scan table and it was only inspected using the MAPS. Figure 3-15 presents a photograph of the scanning system and the dataset.

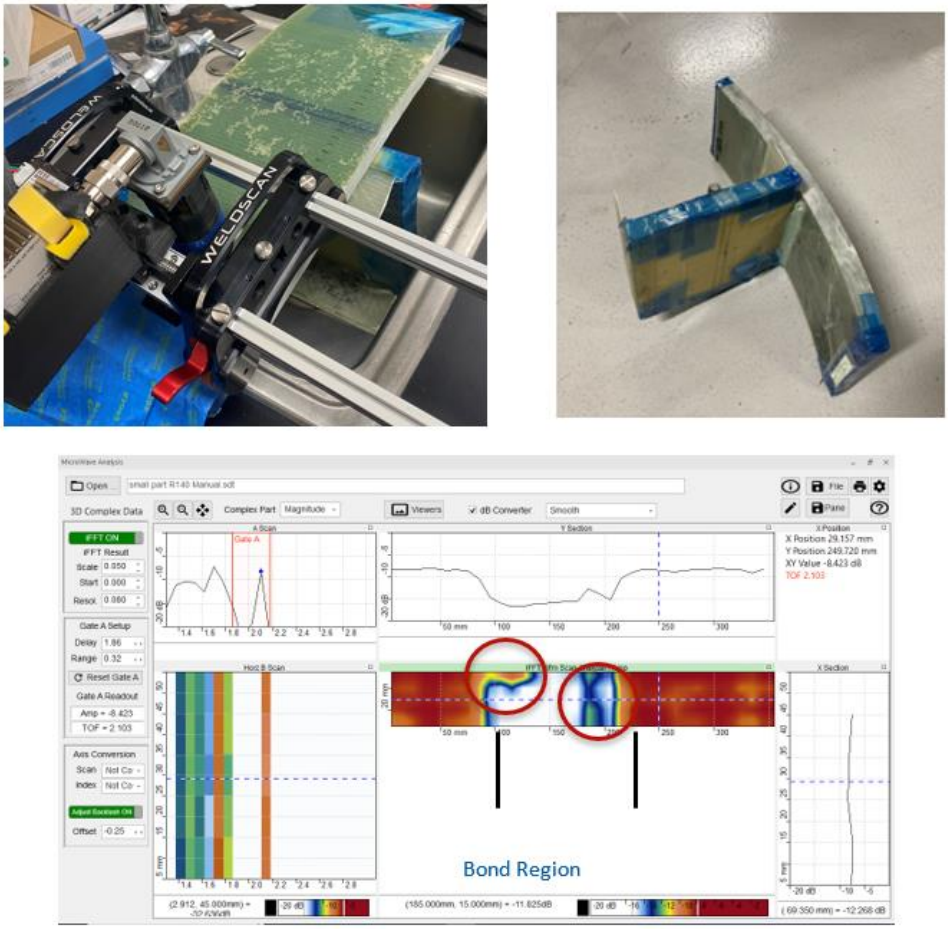

Figure 3-8. WIND-7-110-SPAR-150. Scanning with the MAPS (top left), isometric photograph of the part showing the curvature (top right), and data (bottom).

Looking at the inspection result, the area of the spar cap that is bonded underneath the top surface of the part can be identified. The small area at the top left corner of the bond area and the region spanning the width (circled in red) indicates dis-bonds in the adhesive area. The presence of a dis-bond in the upper left region was confirmed visually, and a photograph taken of the region, is shown in Figure 3-16. It is a small region of missing adhesive underneath the fiberglass upper layer.

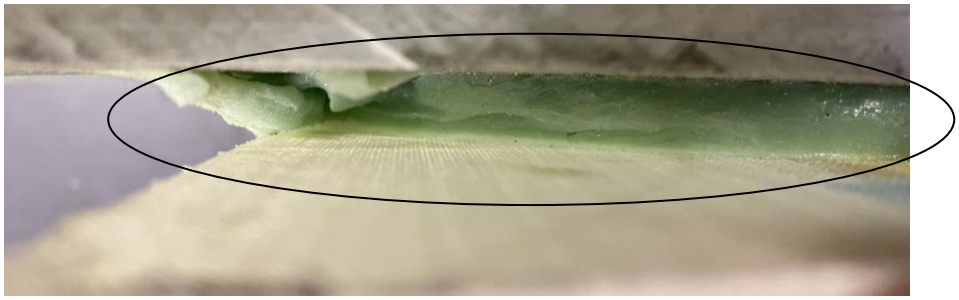

Figure 3-9. WIND-7-110-SPAR-150. Missing adhesive underneath the fiberglass piece.

The second disbond could not be confirmed because it is not visible in the part. It is located directly between the upper portion and the adhesive but above the spar cap. The locations of the flaws are overlaid on images of the WIND-7-110-SPAR-150 in Figure 3-17.

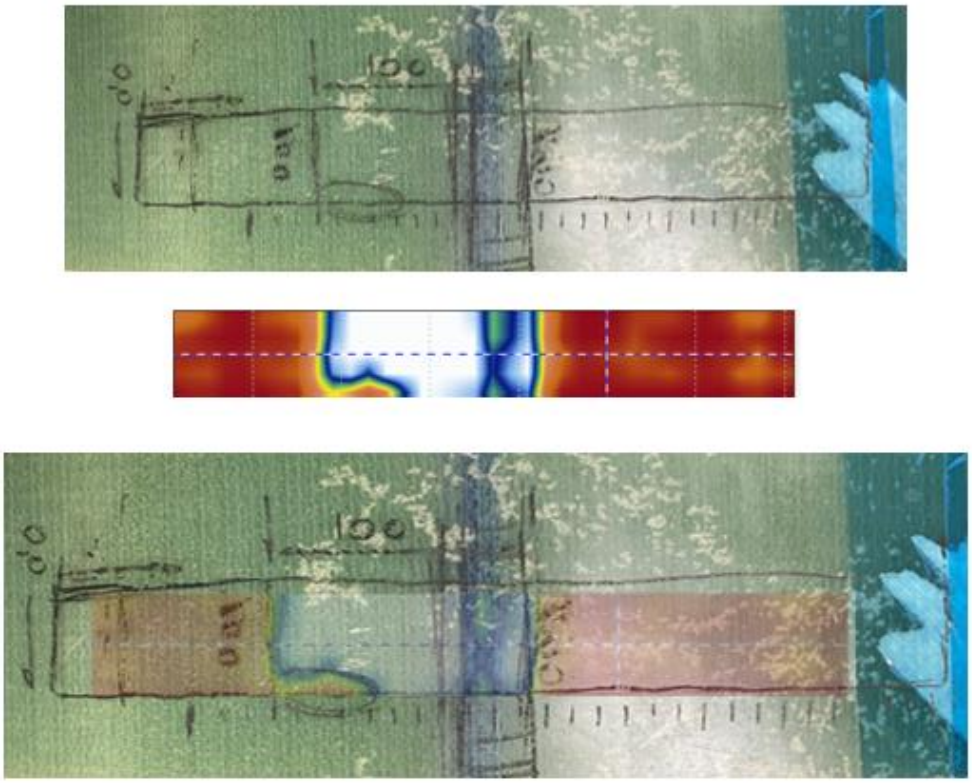

Figure 3-10. Sample WIND-7-110-SPAR-150. Photograph of the top of the sample (top), C-scan data of the inspection with MAPS (middle), and data overlaid on top of photograph (bottom).

4 FABRICATION OF OFFSHORE WIND SAMPLES

4.1 Overview

To support the advancement of the inspection methods for offshore wind blades a total of 24 samples were fabricated. The samples include representative materials and thicknesses used for the fabrication of offshore wind blades. Additionally flaws and/or discontinuities were added to each one of the samples depending on the nature of the material being used. The type of panels fabricated used a variety of materials that included the following:

- Balsa core panels (3 samples)
- Carbon pultrusion panels (3 samples)
- Foam core panels (2 samples)
- Fiberglass panels with porosity (16 samples)
- Wrinkle samples (2 samples)

A summary of the sample inventory is included in Table 4-1. Photographs referenced in the table are included in the body of this report in Section 4 and in Appendix A.

Table 4-1. Summary of offshore wind blade samples.

Sample	Number of samples	Sample ID	Figures
Carbon pultrusion	2	23002-02	4-1, 4-2, 4-3
Balsa Core	2	23002-01	4-4
Balsa Core	1	23002-03	4-4
Carbon pultrusion	1	23002-04	4-1, 4-2, 4-3
Foam core	2	23002-05	4-5
Porosity trial	1	23002-06	4-7
Porosity trial 6a	1	23002-06a	A-1
Porosity trial 6b	1	23002-06b	A-2
Porosity	1	23002-07	A-3
Porosity	1	23002-08	
Porosity	1	23002-09	
Porosity	2	23002-10	A-4
Porosity	2	23002-11	A-5
Porosity	2	23002-12	A-6
Porosity	2	23002-13	A-7
Porosity	2	23002-14	A-8
Wrinkle sample	2	23002-15	4-8

4.2 Summary of the Samples and Fabrication Process

This section provides a brief description of the process followed to fabricate the different samples that included specific materials and defects. The samples will be used as part of the program to deploy NDE methods. The information for the NDE methods and the samples tested is included in Section 3.

4.2.1 Carbon pultrusion samples

Carbon pultrusion plates were stacked in a brick-like pattern with a carbon biaxial pattern between each pultrusion layer and a 1 mm (0.039 in.) gap between each plate. The panels were manufactured using vacuum infusion on a heated table for 4 hours at 40°C (105°F) and post-cured for 10 hours at 70°C (158°F). Figure 4-1 presents some photographs of the process followed for fabrication.

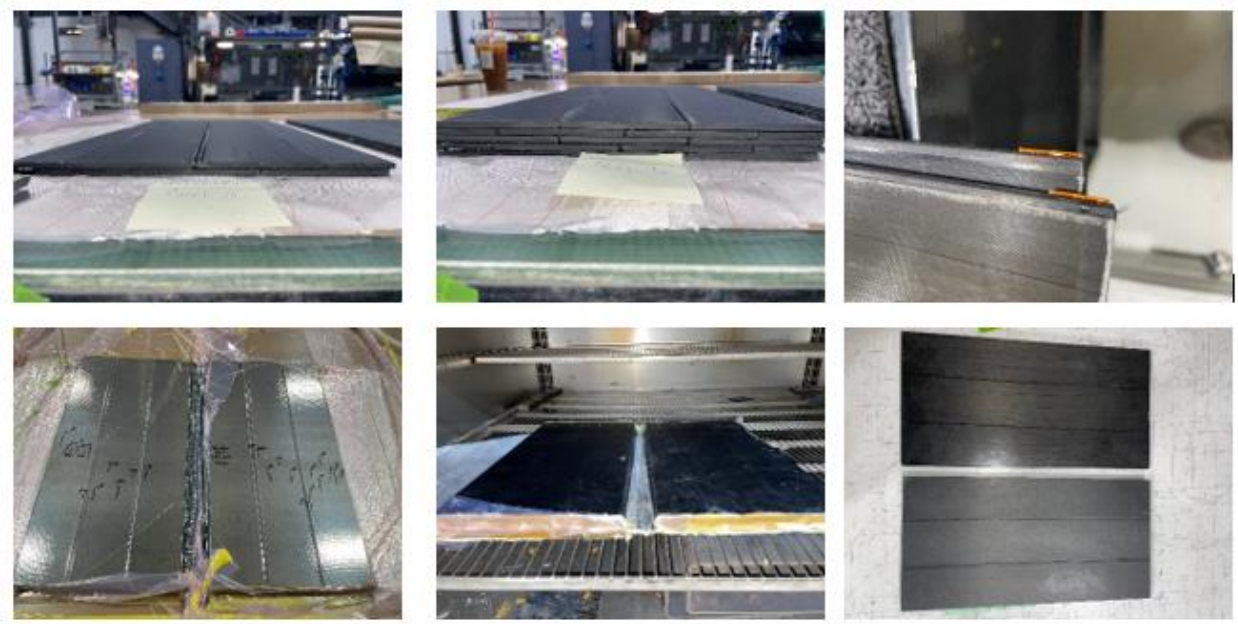

Figure 4-11. Fabrication of carbon pultrusion panels with five layers. Two layers of carbon (top left), five layers (top middle), inserts (top right), infusion (bottom left), curing (bottom middle), samples without drilled holes (bottom right).

After the samples were cured and completed, round defects were machined using a vertical mill to drill holes with variable depths and diameters as shown in Figure 4-2. Figure 4-3 presents a photograph of the samples.

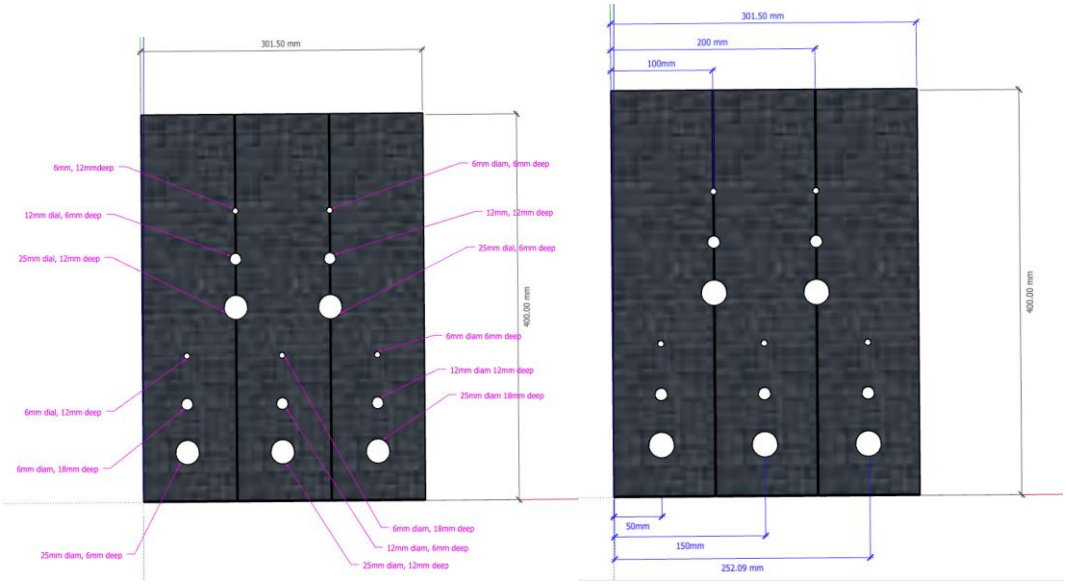

Figure 4-12. Sketches of back-drilled holes on carbon panels. Diameter and depth of holes (left) and position of holes (right) (1 in. = 25.4 mm)

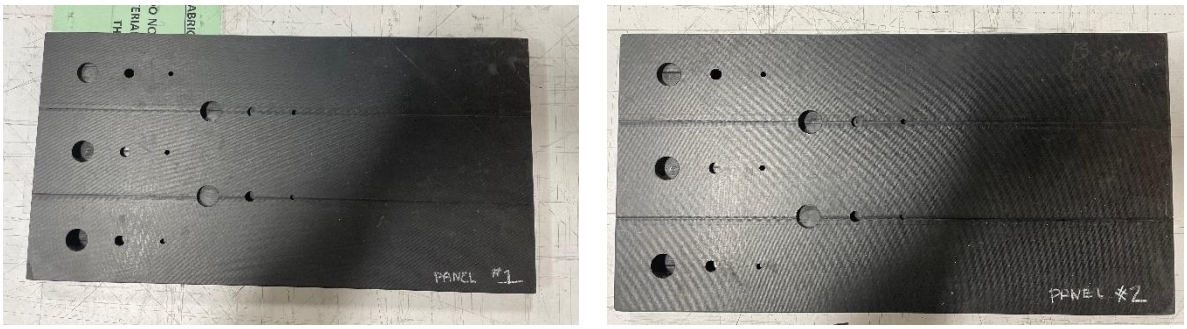

Figure 4-13. Photographs of carbon samples with back-drilled holes.

4.2.2 Balsa core samples

The balsa core was machined with 4.8 mm (3/16 in.) through holes spaced every 50.8 mm (2 in.) Non-perforated Teflon was used to create the pull-tab defects and placed on the B side before the infusion. The panels were manufactured using vacuum infusion on a heated table for 4 hours at 40°C (105°F). Bond paste was applied to the B surface of the panel with HDPE inserts and post-cured for 10 hours at 70°C (158°F). A summary of the fabrication process is presented in Figure 4-4.

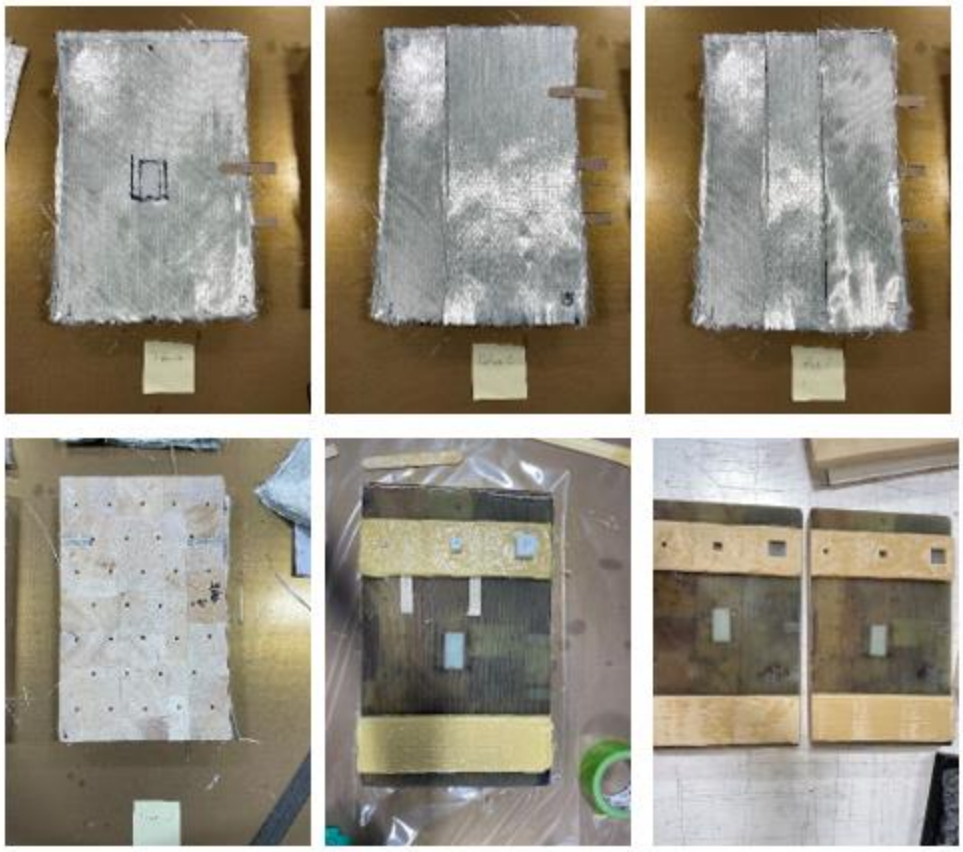

Figure 4-14. Eighteen-ply Balsa core GFRP samples. Sample 1 Layer 13 (top left), Layer 15 (top middle), Layer 17 (bottom left), Sample 2 Balsa core (bottom middle), finished samples (bottom right).

4.2.3 Foam core samples

The PET Foam core was machined with 4.8 mm (3/16 in.) through holes spaced every 50.8 mm (2 in.) throughout the core. Non-perforated Teflon was used to create the pull-tab defects and placed on the B side before the infusion. The panels were manufactured using vacuum infusion on a heated table for 4 hours at 40°C (105°F). Bond paste was applied to the B surface of the panel with HDPE inserts and post-cured for 10 hours at 70°C (158°F). Figure 4-5 presents a photograph of the finished sample.

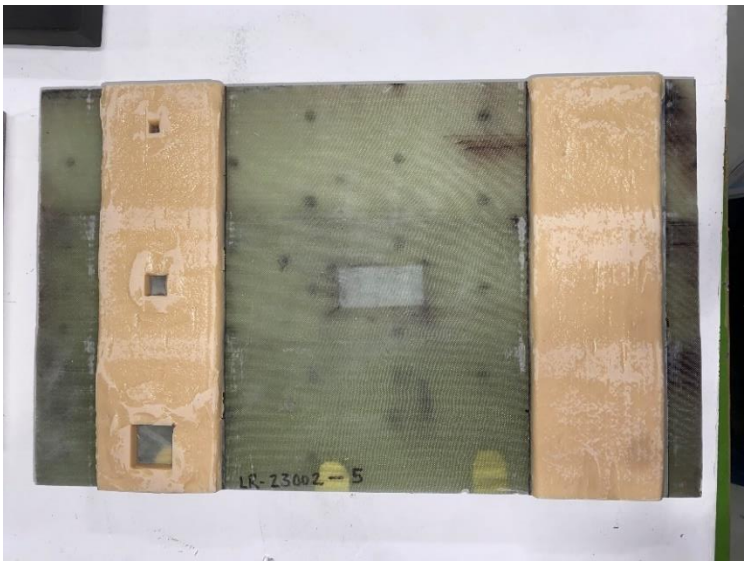

Figure 4-15. Foam core sample.

4.2.4 Porosity samples

The samples were made of 18 plies of glass biaxially oriented +45°/-45. Resin ratios and quantities were kept consistent among the porosity panels, and the time of resin mix was recorded. The panels were manufactured using vacuum infusion on a heated table for 4 hours at 40°C (105°F). The time of the feed opening (resin intake) and the pressure of the vacuum was used as a variable to control the porosity level. Depending on the remaining gel time, the pressure was gradually dropped from 30 inHg to 15 inHg and eventually to 0 inHg. Figure 4-6 presents photographs of the trial process for introducing porosity and a closeup of induced porosity. Learning from this cure process, syringes were not used for the final product and double vacuum infusion with variable pressure was applied to produce different concentrations of porosity per panel. Figure 4-7 shows a photograph of the sample after curing.

Figure 4-16. Injection of air during infusion with a 20-cc syringe.

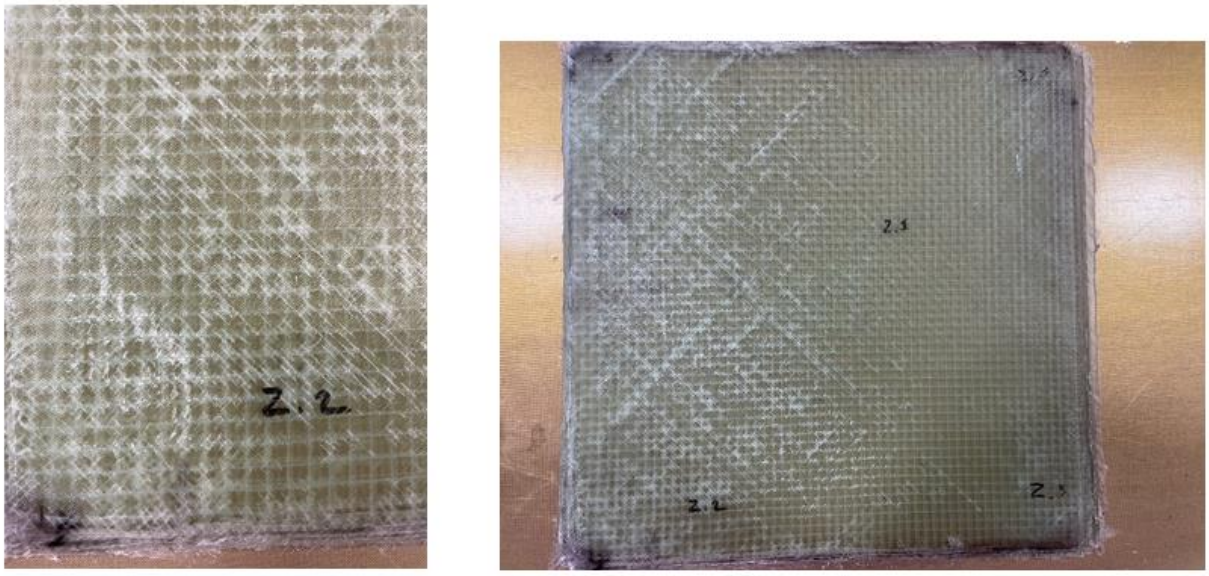

Figure 4-17. Porosity sample trial. Close up of induced porosity (left) and photograph of sample (right).

4.2.5 Wrinkle samples

The wrinkle samples were fabricated with 8 plies of glass biaxially oriented +/-45°,-/+45°. Three resin dowels were inserted in the midplane of each panel and oriented in the 0° direction. A High-Density Polyethylene (HDPE) mold was used to create the resin dowls with a semicircular profile. The dowels had variables depths of 4, 6, and 8 mm (0.16, 0.23, and 0.31 in.) with a fixed diameter of 8mm (0.31 in.) The panels were manufactured using vacuum infusion on a heated table for 4 hours at 40°C (105°F) and post cured for 10 hours at 70°C (158°F). Figure 4-8 presents a plan and a cross-section view of one of the wrinkle panels.

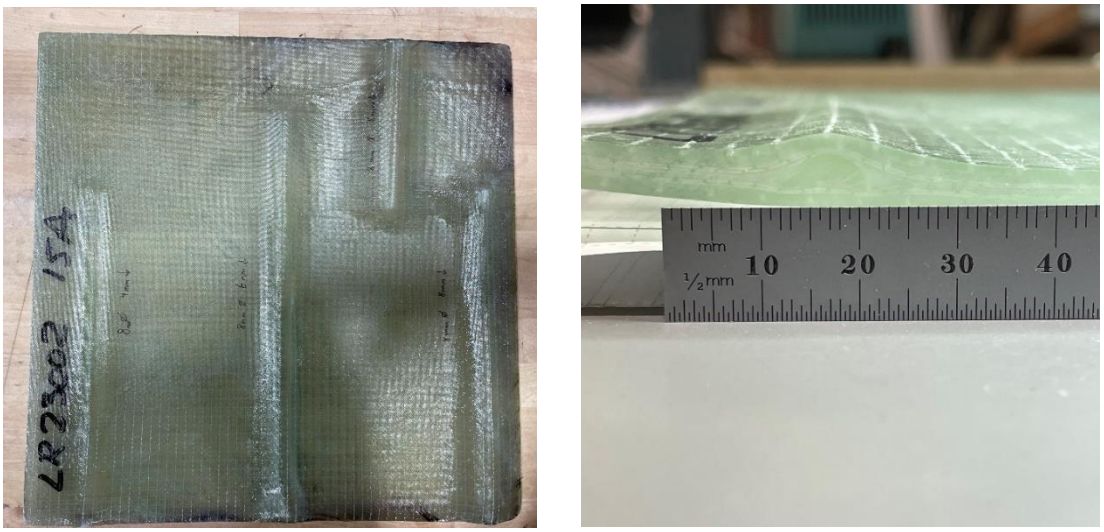

Figure 4-18. Plan view (left) and cross section view of the wrinkle panel (right).

5 TESTING OF OFFSHORE WIND SAMPLES

The samples prepared and described in Section 2 were tested and analyzed using NDE methods. For the carbon fiber and fiberglass samples, ultrasonic and microwave testing were used, respectively. More details about the testing and samples tested are included in Sections 3 and 4.

5.1 Ultrasound

The carbon fiber specimen, as photographed in Figure 5-1, manufactured by TPI was subject to UT scanning for an initial qualitative assessment of UT capabilities and a comparison of full matrix capture (FMC) /total focusing methods (TFM) and plane wave imaging (PWI)/TFM. The specimen measures 577×293×26 mm or (22.7×11.5×1.02 in.) and the longitudinal sound speed is determined to be 2600 ms^{-1}. Of the two largest faces of this specimen, one face is appreciably smoother than the other. Fifteen FBH are connected to the large face of the specimen that is rougher. The FBH are arranged in three sets of five with diameters of 30.0, 15.0, and 7.5 mm (1.2, 0.6, and 0.3 in.) and depths of approximately 8, 14, and 20 mm (0.3, 0.6, and 0.8 in.)

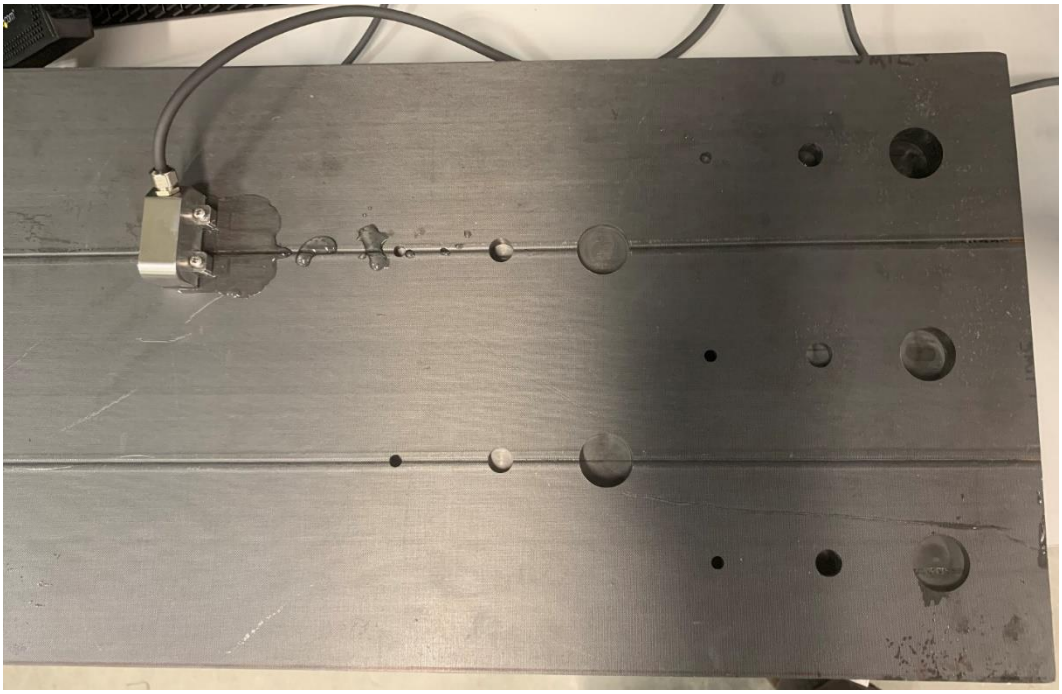

Figure 5-1. Carbon fiber specimen manufacturing by TPI for UT scanning. The 5MHz phased array probe with Ultragel II couplant is shown atop the specimen towards the top left.

The UT instrument used was the Zetec Emerald 64/128, a device capable of FMC and PWI acquisition and real-time TFM display. Two different phased array probes were used to acquire data without wedge. Their attributes are listed in Table 5-1. Ultrasonic acquisitions were carried out in elementary FMC and in PWI. The latter was done with angular sweeping from -10° to 10° in 5° increments. Coupling between the probe and the specimen was done by Ultragel II.

Table 5-1. Attributes for the phased array UT probes used to scan the TPI carbon fiber samples (1 in. = 25.4 mm)

Probe ID	**1-11506-1060**	**13493-1011**
Centre Frequency	5.0MHz	10.0MHz
Element Count	64	128
Pitch	0.6mm	0.3mm
Elevation	10.0mm	10.0mm
Pulse Width	100ns	50ns
Active Aperture	38.4mm	19.2mm

Six scans were carried out in total; five from the smoothest face and one from the face to which the FBHs were connected. The scans are listed in Table 5-2, and the cumulated side and end views are shown in Figure 5-2. Cumulated side view (left subplot) and end view (right subplot) of the FMC/TFM scan of the TPI sample at 5MHz. 2 though Figure 5-7 for each corresponding scan, as indicated in the second column of the table. The probe motion range is short so as only to cover a “set” of three FBHs. Probe motion was aligned to the longest dimension of the block in all but one scan.

Table 5-2. Scan attributes for the TPI carbon fiber samples (1 in. = 25.4 mm)

Scan ID	**Shown in Figure**	**Acquisition Type**	**Inspection Frequency**	**Applied Hard Gain**	**Reconstruction Volume Dimension**
FMC_05	Figure 5-2**Error! Reference source not found.**	FMC	5 MHz	30dB	(40×25×200) mm
PWI_05	Figure 5-3	PWI	5 MHz	30dB	(40×25×200) mm
FMC_10	Figure 5-4	FMC	10 MHz	45dB	(20×25×200) mm
PWI_10	Figure 5-5	PWI	10 MHz	35dB	(20×25×200) mm
PWI_05t*	Figure 5-6	PWI	5 MHz	30dB	(40×25×200) mm
PWI_05v**	Figure 5-7	PWI	5 MHz	30dB	(40×25×200) mm

* Scan taken with probe motion aligned to the second-longest dimension of the plate
** Scan taken from side connected to the FBHs

The figures show reflections from the bonds between successive pairs of layers, spaced apart by 5mm (0.2 in.) The bulk material is attenuative but there is sufficient ultrasonic energy to propagate to the backwall. Shadowing, manifesting as gaps in backwall reflection or interlayer reflections, is visible in the cumulative end views. The shadows are caused by obstructions to

the ultrasonic bulk wave propagation due to certain “void channels” (of which two are visible as grooves in Figure 5-1) running along the length of the specimen.

The FBHs were imaged strongly in all scans at both frequencies and at both types of acquisition, demonstrating the viability of UT in this frequency range for ultrasonic inspection of this material. In general, the PWI/TFM scans show stronger ultrasonic reflections than those of FMC/TFM and this is attributed to the greater amount of ultrasonic energy being introduced to the part. All scans have a region close to the specimen interface that is saturated with noise, indicative of the near field of the probe. The region depth is around 6-7 mm (0.24-0.28 in.) For this reason, the first 5 mm (0.20 in.) depth or so of the volume beneath the specimen interface is not reconstructed.

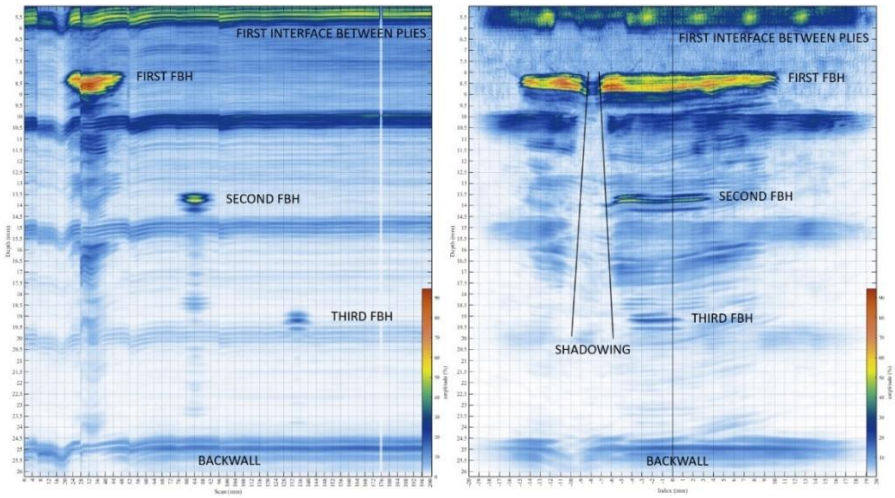

Figure 5-2. Cumulated side view (left subplot) and end view (right subplot) of the FMC/TFM scan of the TPI sample at 5MHz.

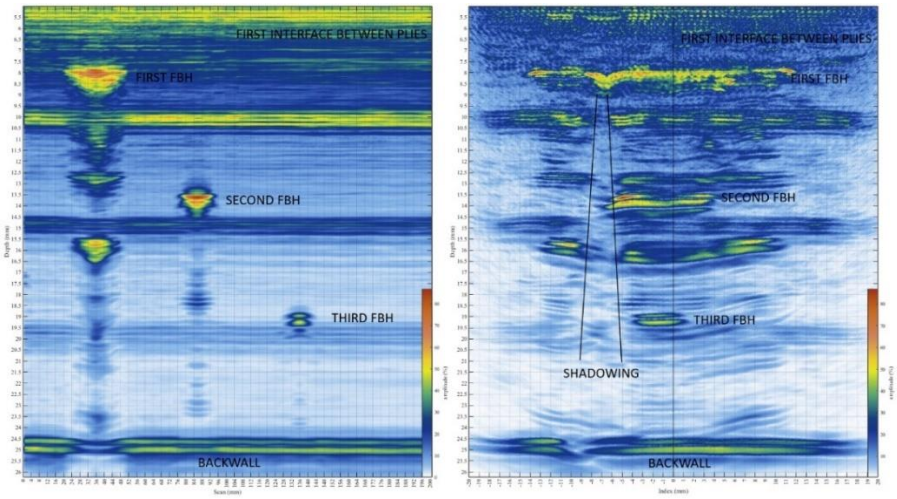

Figure 5-19. Cumulated side view (left subplot) and end view (right subplot) of the PWI/TFM scan of the TPI sample at 5MHz.

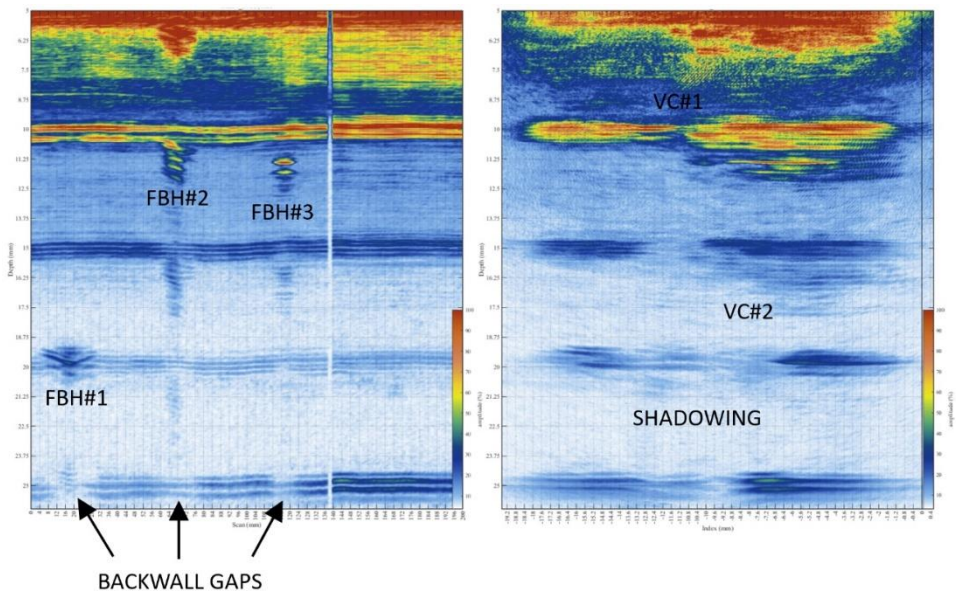

Figure 5-4. Cumulated side view (left subplot) and end view (right subplot) of the FMC/TFM scan of the TPI sample at 10MHz. The annotation lists void channels (VC) and flat-bottom holes (FBH).

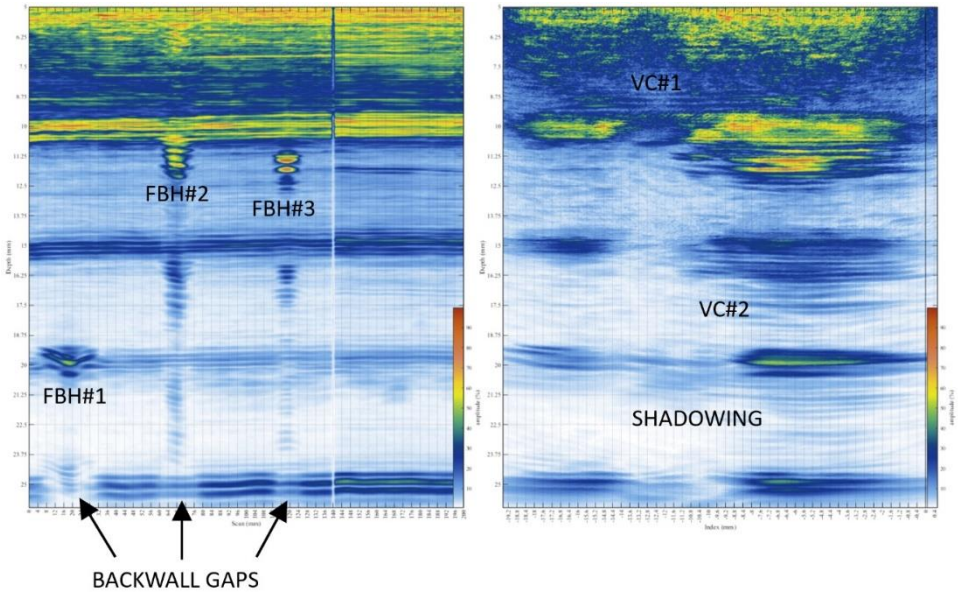

Figure 5-5. Cumulated side view (left subplot) and end view (right subplot) of the PWI/TFM scan of the TPI sample at 10 MHz. The annotation lists void channels (VC) and flat-bottom holes (FBH).

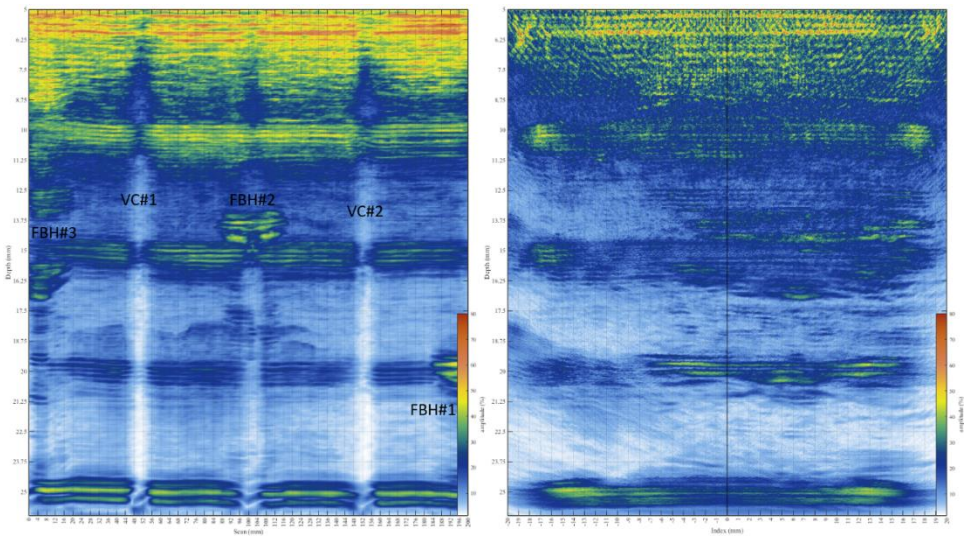

Figure 5-6. Cumulated side view (left subplot) and end view (right subplot) of the PWI/TFM scan of the TPI sample at 5MHz. Scan taken “transversely”; that is, with the probe motion aligned to the second-longest dimension of the plate. The annotation lists void channels (VC) and flat-bottom holes (FBH).

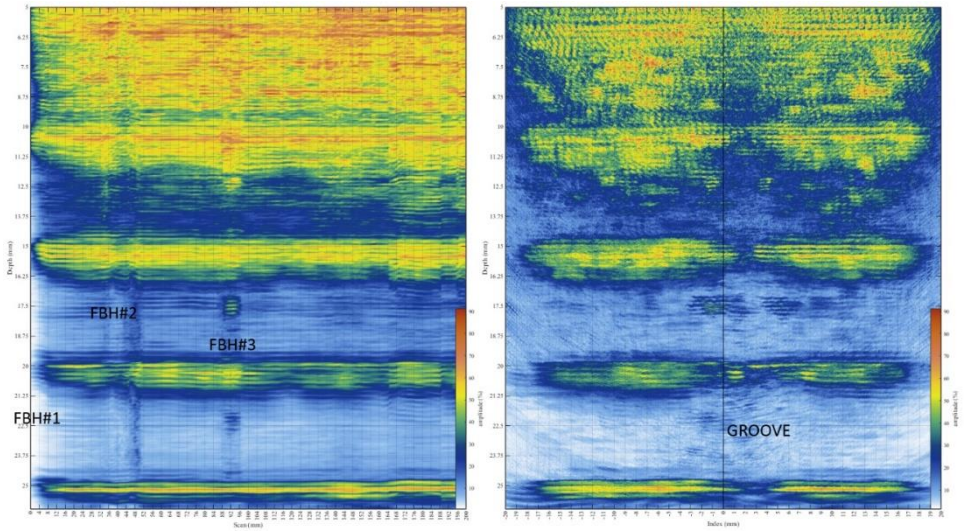

Figure 5-7. Cumulated side view (left subplot) and end view (right subplot) of the PWI/TFM scan of the TPI sample at 5MHz. Scan taken from the face connected to the FBHs.

5.2 Microwave

The objective of this phase of the project was to perform testing on samples representative of offshore wind blades. To reach this objective, samples with flaws were fabricated as described in Section 2 of this report. For this section of the report, a multi-frequency microwave technique was used to test the samples and demonstrate the capability of the technique to detect defects.

Some of the samples in the testing program included construction of layered materials, such as GFRP and balsa and foam. The inspection of these types of components creates a challenging environment for other techniques, such as ultrasound. For this reason, the use of a microwave technology is an important part of this program.

5.2.1 CFRP sample

One CFRP sample was tested using the microwave system. The sample was 50 mm thick and had multiple back-drilled holes. The CFRP sample was inspected, but microwave was not capable of obtaining volumetric information because the CFRP material is conductive and a reflector of EM radiation.

5.2.2 Samples with core material

Two samples of GFRP sandwich panels with core material, one with a balsa wood core and one with a foam core, were tested. The samples, construction processes, and materials utilized are typical of an offshore wind blade. In both samples, the core materials are sandwiched between two thin ~5 mm (0.2 in.) GFRP layers, and the entire sample is approximately 50 mm (2 in.) thick. The samples include multiple reflectors which mimic specific types of flaws found in these blade materials.

The reflectors include several pull-tab locations between the bottom GFRP and the core material, a central reflector meant to mimic a porous region, and two bond paste layers on the bottom – one that has three square openings of different sizes that mimic voids in the bond paste. There are also three different ply drops on the bottom section. These are not meant to mimic flaws, but the intent was simply to see if they can be detected. Images of the balsa core and foam core sample are shown in Figures 5-8 and 5-9, respectively.

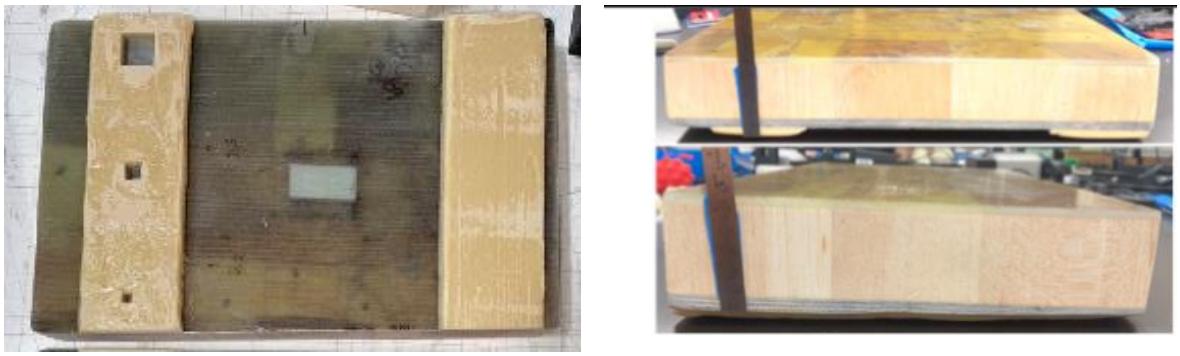

Figure 5-8. Bottom view (left) and side view (right) of the 50 mm (2 in.) thick balsa core sample.

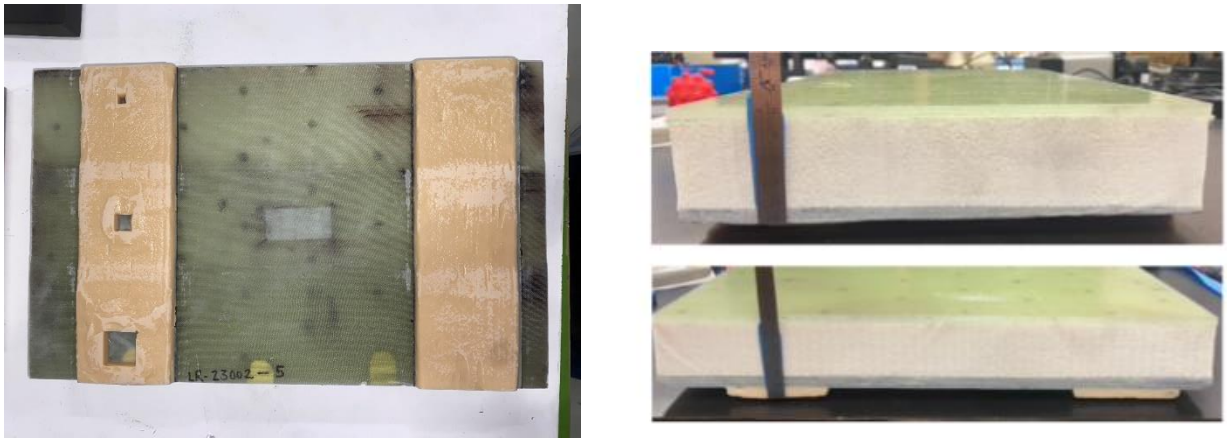

Figure 5-9. Bottom view (left) and side view (right) of the 50 mm (2 in.) thick balsa core sample.

The panels were inspected from the top surface using the standard AMWI multi-frequency microwave system. The inspection frequency was 10-18GHz and this was subdivided into 201 discrete frequency bins. The samples were scanned using several X-Y matrix sizes and the 5 mm by 5 mm matrix provided the best results for locating the features. The use of the finer mesh technique is not time limiting, although it does take about twice as long as the 15 mm by 15 mm (0.6 in. by 0.6 in.) scan time. The 15 mm by 15 mm (0.6 in. by 0.6 in.) inspection time took about 5 minutes and the 5 mm by 5 mm (0.2 in. by 0.2 in.) took approximately 12 minutes.

Figure 5-10 through 5-20 present the results of microwave testing on the balsa wood sample. Figure 5-10 shows the location of the simulated porosity and one of the pull-tabs as detected through the balsa core. Figure 5-11 demonstrates the detection of the ply drops in the GFRP layer through the balsa core. Figure 5-12 shows four additional pull-tabs which were detected through the balsa core. Finally, Figure 5-13 shows that two of the three bond paste flaws are detected though two GFRP layers and the balsa core. The smaller of the three instances of delamination in the bond paste was determined to possibly be detectable in the sensor data, but not necessarily reliably. In total, all flaws except the smallest bond paste flaw were detected.

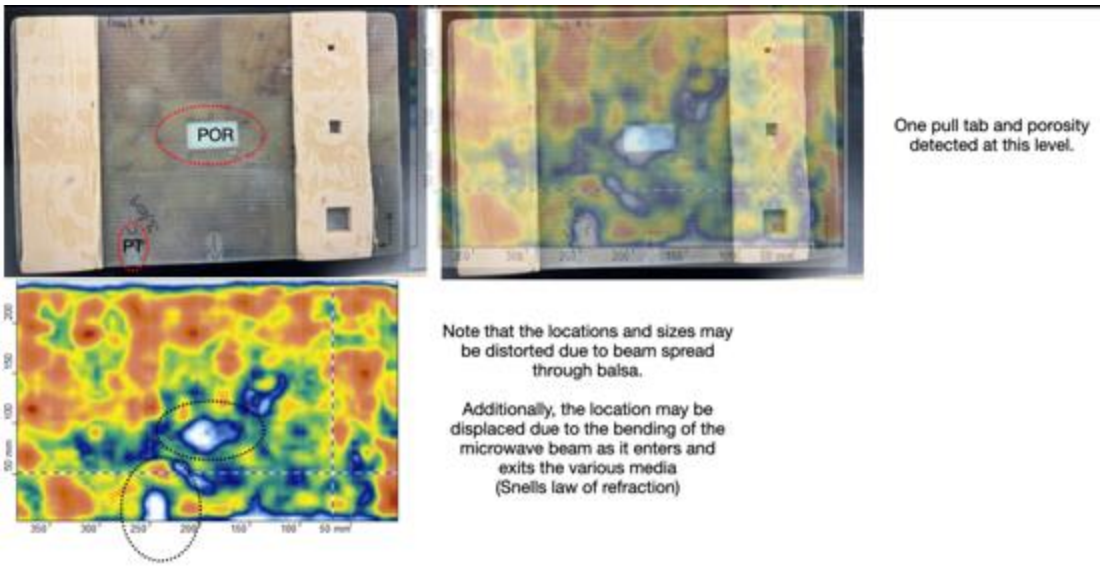

Figure 5-10. Lower GFRP samples compared to flaw locations.

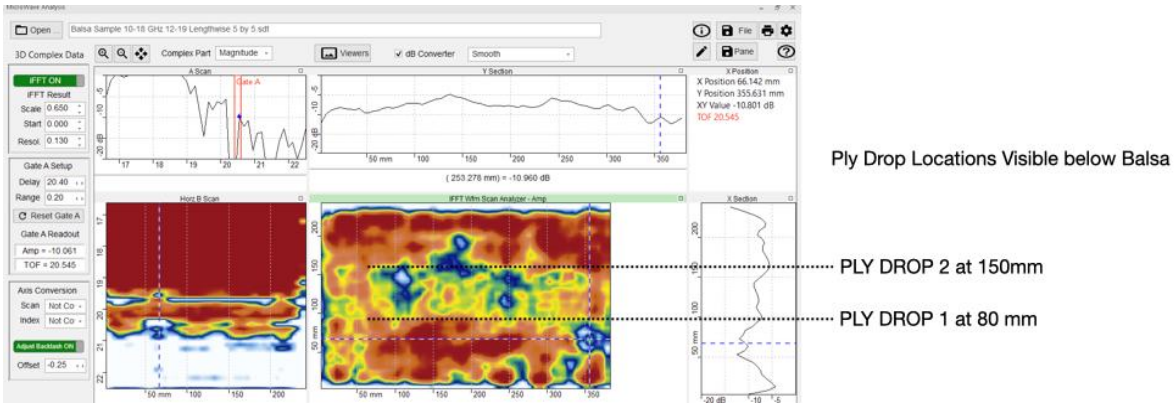

Figure 5-1120. Lower GFRP layer (1in.=25.4mm).

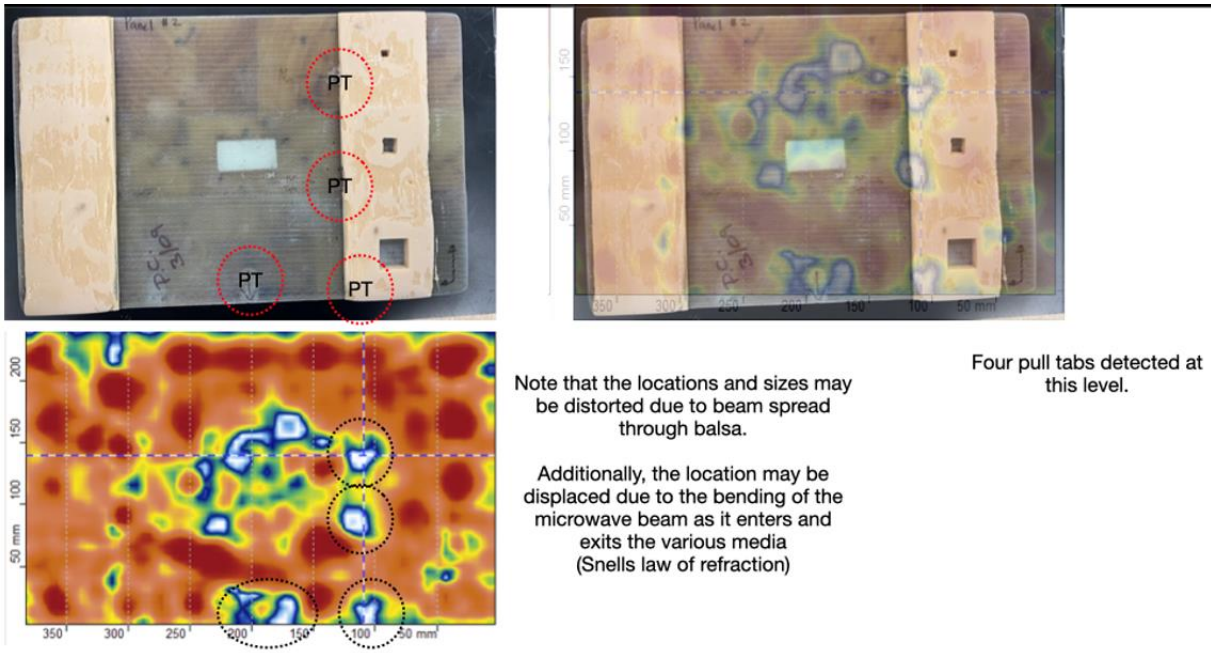

Figure 5-12. Lower GFRP layer compared to flaw locations.

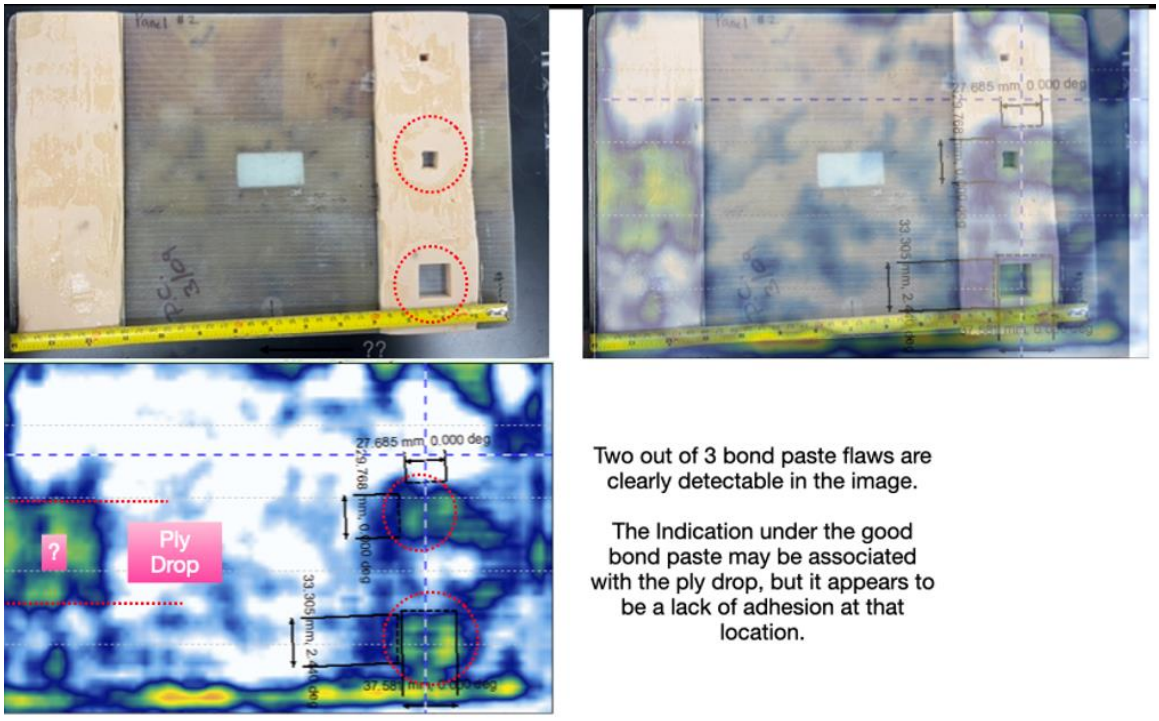

Figure 5-13. Overlay of microwave image over panel. (1in.=25.4mm).

The foam core samples were inspected using the same methodology as the balsa core samples. The data analysis was performed using Synthetic Aperture Radar (SAR) focusing techniques. This was done because of the sensitivity of the inspection method to the round holes in the foam core for resin transfer during infusion. These round resin-filled holes provided a large source of noise for the inspection technique. As a result, increased sensitivity was required for flaw detection over the balsa sample due to the increased sample noise level. All sample flaws were detected using this data analysis method.

Figure 5-14 shows how the ply drops in the lower GFRP layer are detectable through the balsa core. The ply drop locations in the data are close to the actual ply drop locations, even with beam spread and attenuation through the foam core.

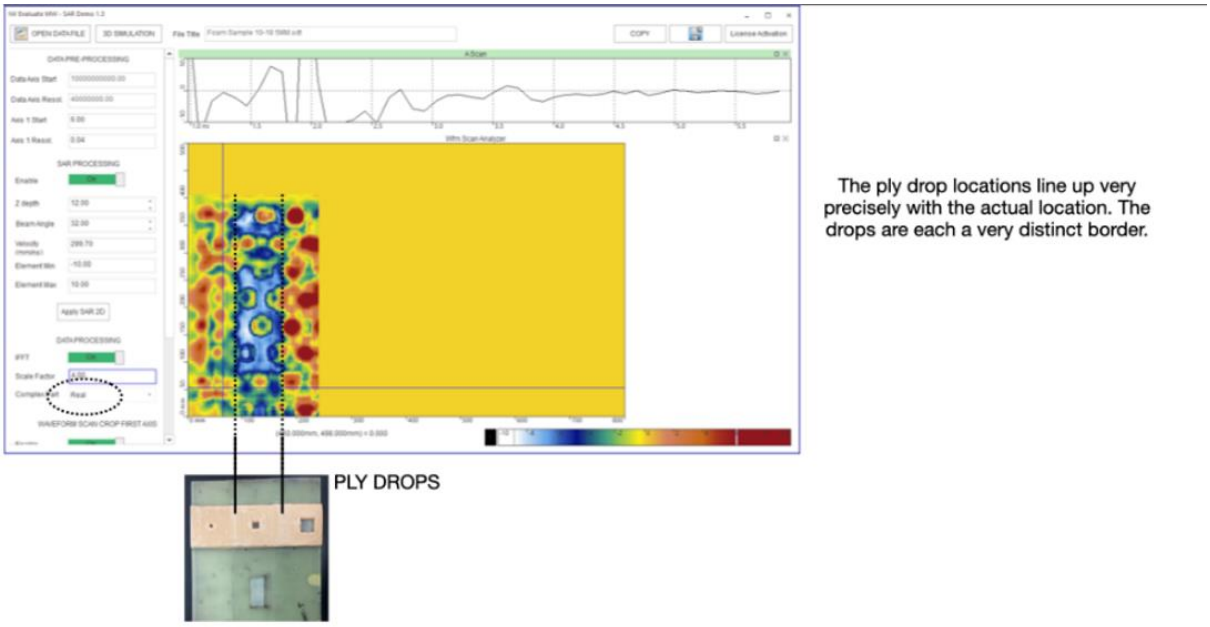

Figure 5-14. Ply Drop Detection.

Figure 5-15 demonstrates how the porosity flaw is detectable in the presence of the resin hole background noise. The simulated porosity flaw results in a much different signal than the rest of the GFRP panel in which it is located. Figures 5-16, 5-17, and 5-18 show three of the pull-tab locations near the edge of the sample. Finally, Figure 5-19 shows all three bond paste flaws and the remaining two pull-tabs. This data analysis set indicates how all flaws are detectable though the foam core.

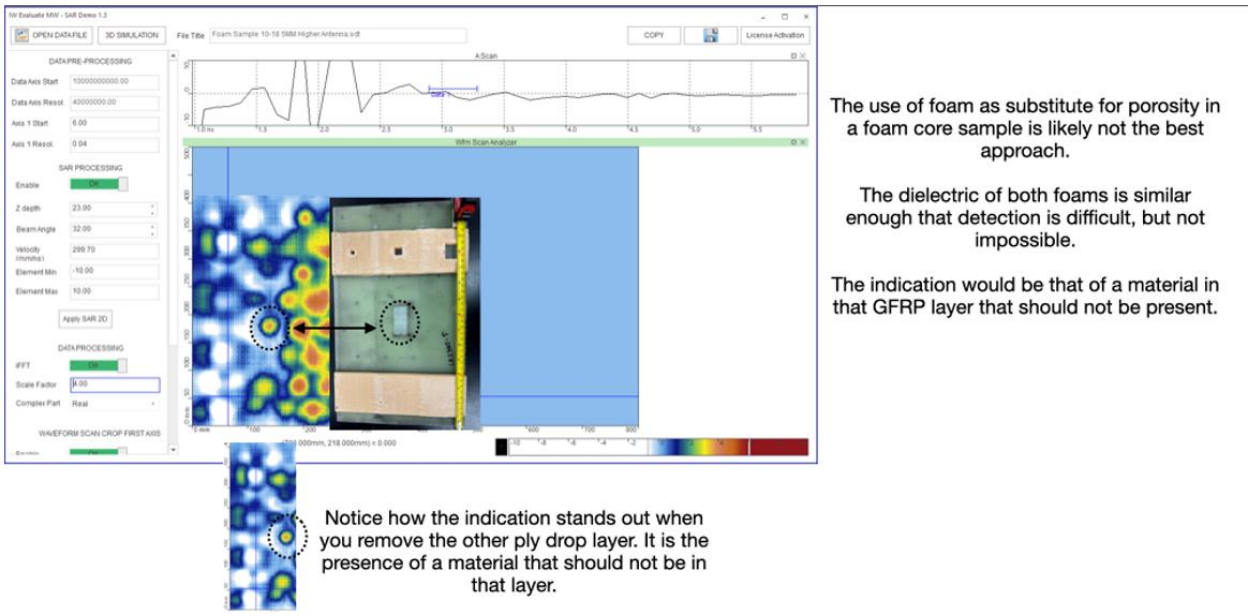

Figure 5-15. Porosity foam flaw.

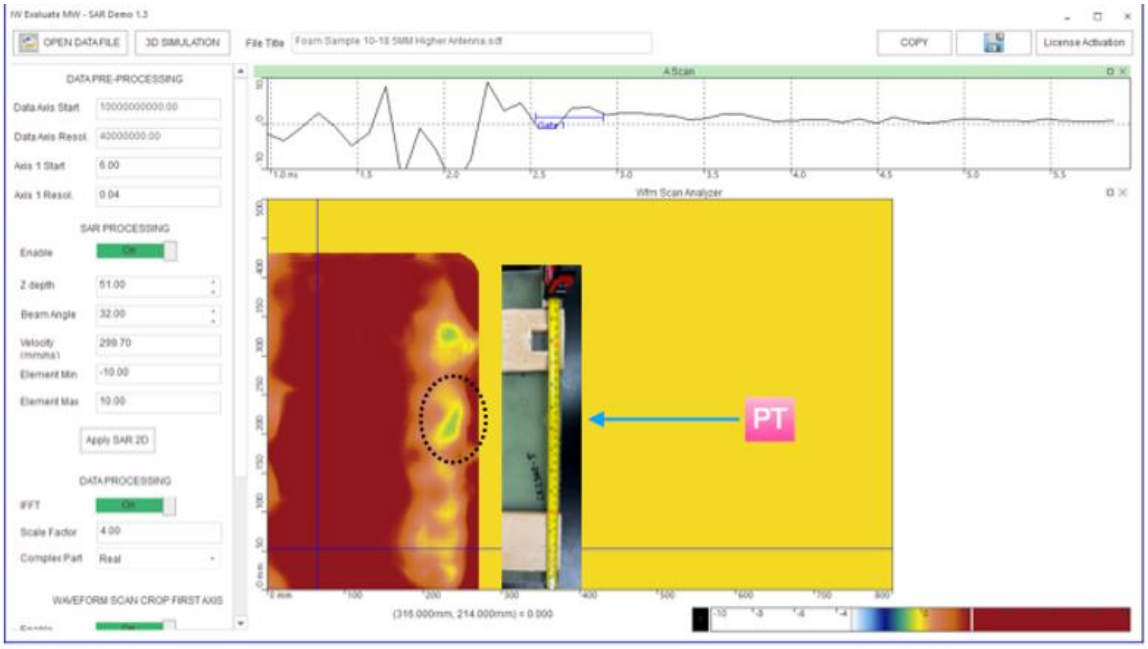

Figure 5-16. Pull-tab.

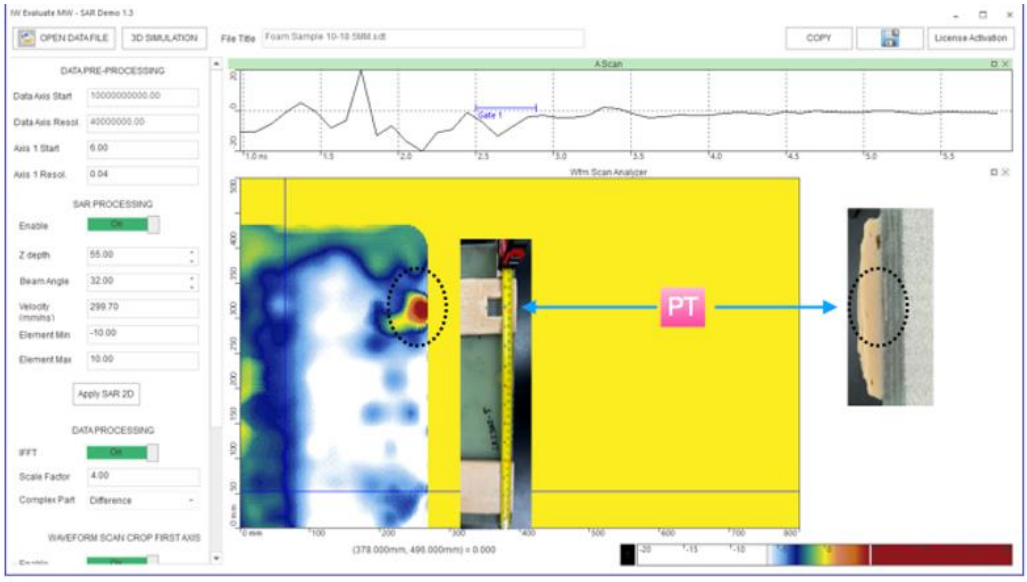

Figure 5-17. Pull-tab under bond paste.

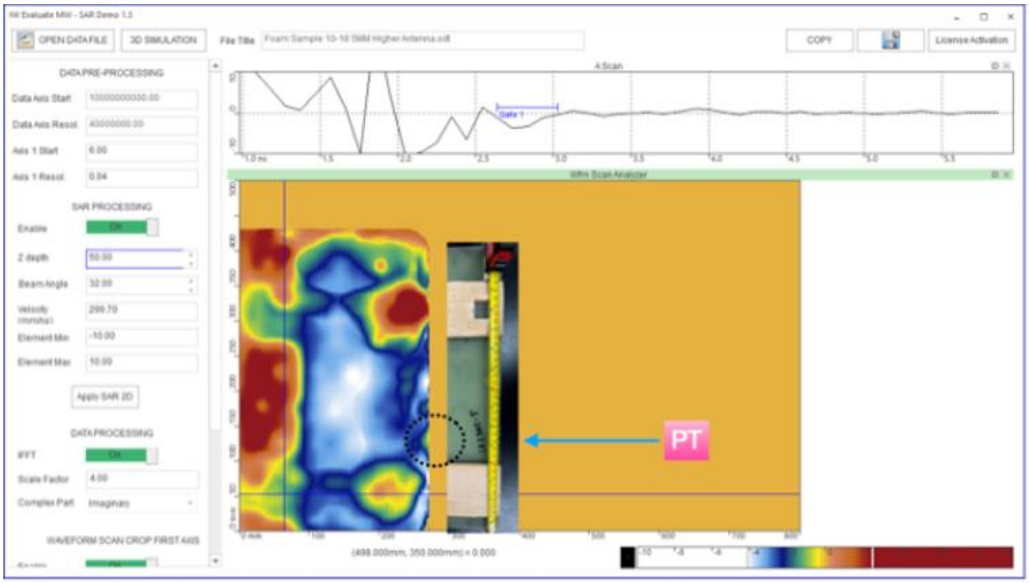

Figure 5-18. Pull-tab.

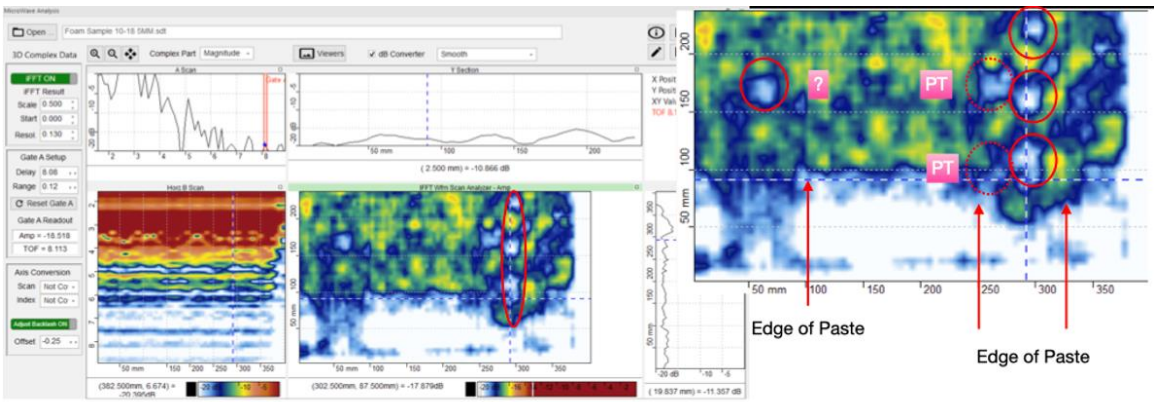

Figure 5-19. Bond paste flaws.

5.2.3 Porosity samples

A set of five (5) GFRP plates each with different porosity levels were provided for testing. The panels have dimensions of 300 mm by 300 mm (11.8 in. by 11.8 in.) with 18 plies of GFRP material [~10 mm (0.4 in.)] thick. The porosity was produced in each panel in a controlled fashion using the process described in Section 4.

The data analysis differs for this evaluation from flaw detection because bulk panel properties are being measured. This type of analysis uses frequency-based data because it represents the reflection coefficient for the entire panel thickness rather than any one layer. This is a better way to measure a bulk property such as porosity.

The data contained in the image can be correlated to the level of porosity in the sample. The electro-magnetic radiation interacts differently based on the amount of porosity and returns a different reflection coefficient, S11. The change in reflection coefficient is measurable and is a function of the amount of porosity in the sample. Because of this relationship, there can be a curve of reflection coefficient versus porosity developed that would lend itself to allowing for pre-calibration of the device prior to inspection.

A typical frequency-based data image is provided for reference in Figure 5-20. By using frequency-based data, a uniform image can be obtained. The frequency range for analysis would be pre-selected as part of the calibration and then listed as an essential variable. In this case, the frequency range selected is centered at 11.56GHz ± 2.3GHz.

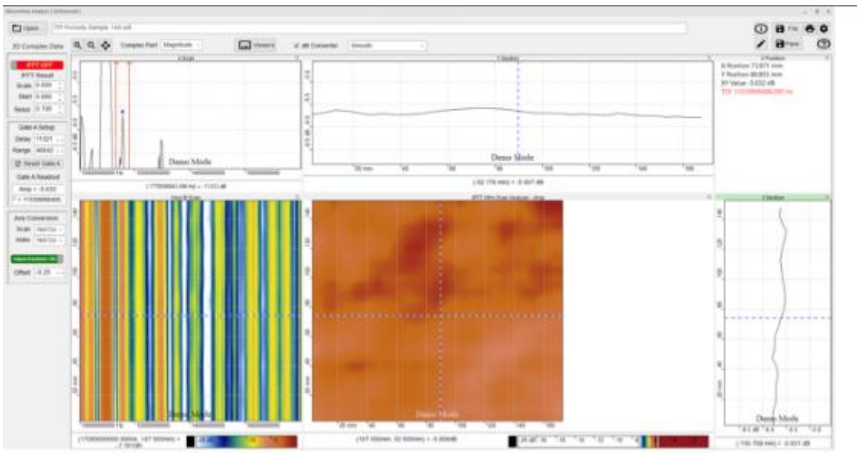

Figure 5-20. Example of Frequency Image 11.56GHz (±2.3 GHz).

Note that Figure 5-20 is created from the same data that can be used for thickness evaluation and depth of defect analysis. If we use the depth approach in the IFFT mode, the image becomes more granular and porosity can be localized within the part. This approach would allow for detection of specific areas of porosity that might be remediated to restore the part strength capability. Specifically, the high porosity sample in Figure 5-21 shows what is likely a channel where air traveled from the edge to the center of the part. This hypothesis is consistent with how the porosity (air) was introduced into the panel during construction. The arrow in the image shows the likely air flow path. This demonstrates the ability to detect overall porosity along with normal part inspection.

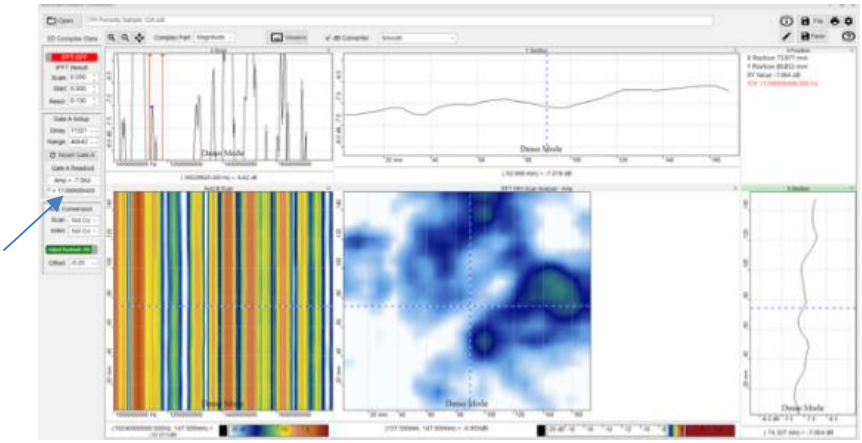

Figure 5-21. Depth Image with Possible Air Path.

In the final analysis of the porosity samples, a data line was developed using the imaginary reflected data at 12.6-13.2 GHz and the average porosity of the sample as determined by destructive testing. The data was collected using the same method as before, but the analysis was done by using the imaginary portion of the actual data (i.e., not dB of data) at a specific frequency range. This data was then averaged over the entire inspected region to develop the average imaginary reflected data for each of the samples. This average data was then plotted versus the average porosity determined via the destructive tests and a linear fit was used to obtain the following equation (eq. 5-1):

$$P = -117.09 \times ID + 59.461 \qquad \text{eq. 5-1}$$

Where *P = Average Sample Porosity* (in percent), and *ID = Average Imaginary data* (at the 12.6-13.3GHz). The porosity plot is shown in Figure 5-22. It is expected that different material types and potentially thicknesses would require different prediction equations.

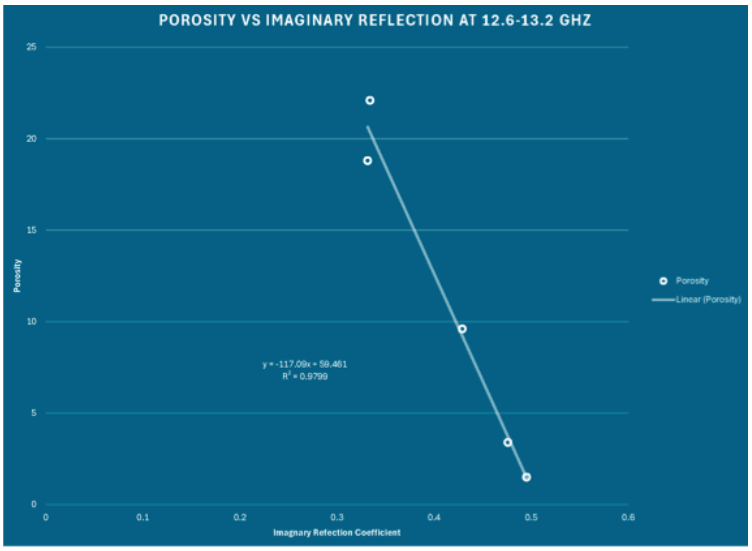

Figure 5-22. Porosity versus Imaginary Data.

5.2.4 Wrinkle panel

The wrinkle panel was inspected using the standard AMWI inspection method for GFRP. The data was collected over the entire panel to capture all wrinkle flaws present in the GFRP panel. The wrinkles extended to the edge of the panel, which made some of the data less reliable due to edge effects.

This type of analysis uses frequency-based data because it represents the reflection coefficient for the entire panel thickness rather than any one layer. This is a better way to measure a bulk property such as porosity.

Figure 5-23 shows that detection of the wrinkle is simple and very clear. The wrinkle has a very distinctive shape in the B Horizontal image. This image is only possible because of the multi-frequency data collection and implementation of the IFFT for the data. This places the data in a "Time of Flight" mode, so the B Horizontal represents a cross section of the part. The signature shape for a wrinkle so distinctive that AI automated detection is possible for future iterations.

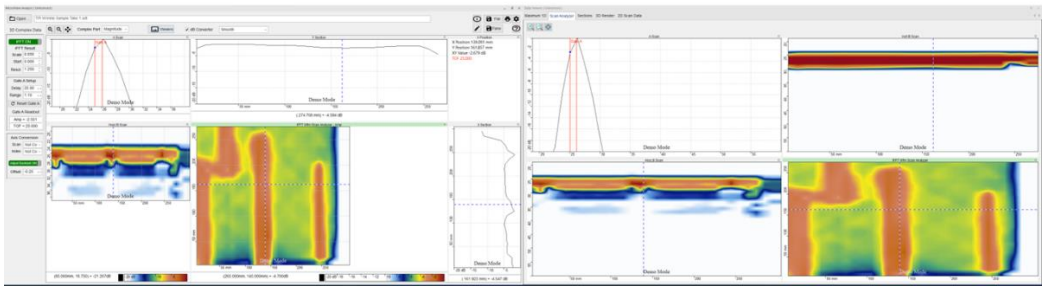

Figure 5-23. Wrinkle Panel Image.

The ability to measure the width and height of the wrinkle is critical to determining the aspect ratio of the wrinkle, which is defined as the width of the wrinkle divided by the height of the wrinkle. The data necessary to determine the depth is available via the multi-frequency inspection capabilities of the AMWI system.

Measuring the width of the wrinkle is similar to measuring any X-Y plane dimension in NDT techniques. The width of the wrinkle is apparent in the data that makes up the C scan image. In the software, this data appears on a data line that can be used for measurement.
The wrinkle data appears as a peak in the data line that intersects the wrinkle. The width of the peak is measured at a location defined as 3dB below the peak. The width at that location is used as the defined width of the flaw. This is demonstrated in Figure 5-24.

To accurately determine the wrinkle height, the material dielectric properties must be part of the input as the resolution factor. The dielectric properties determine the speed of light in the material, which determines the scale for the time of flight. The methods for determining the wrinkle width and depth were established using this sample. The results demonstrated that the method is capable of detecting wrinkles and measuring the critical dimensions of width and thickness of the wrinkles in GFRP. In this case, the material is GFRP and so the resolution is set to 2.290. When this value is used for resolution, the Y axis in the B horizontal closely approximates mm in GFRP. Thus, the height of the wrinkle can then be measured directly in the B Horizontal image.

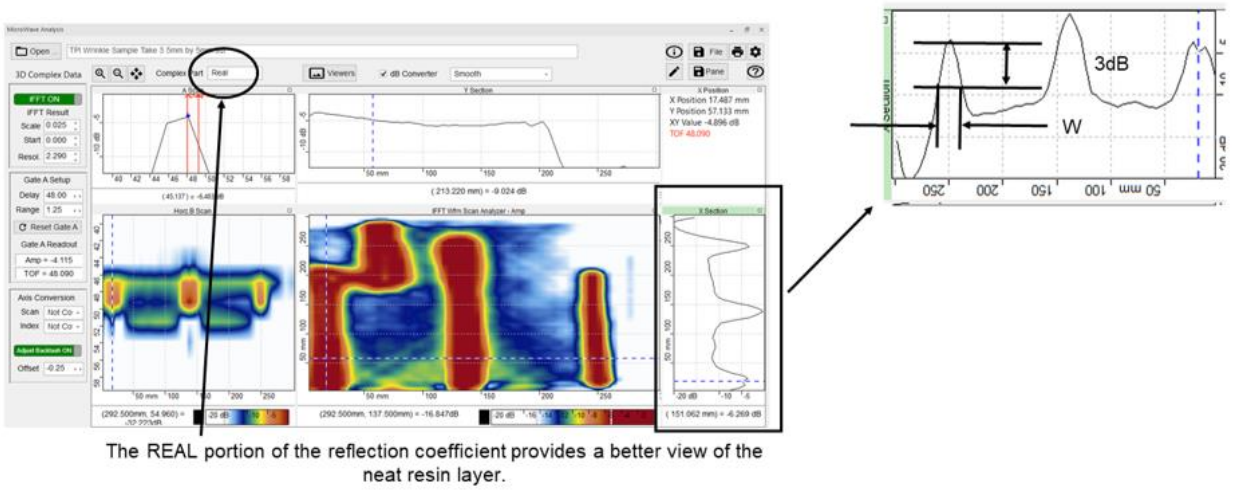

Figure 5-24. Width Measurement.

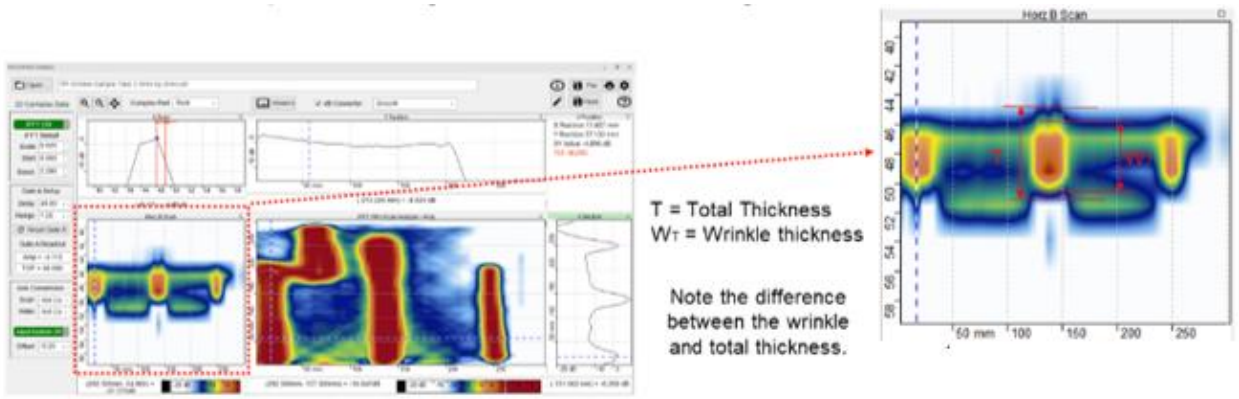

Figure 5-25. Wrinkle height.

Inspecting this wrinkle panel demonstrates the ability of a multi-frequency microwave system to detect wrinkle flaws, measuring wrinkle flaws, and determining the wrinkles critical characteristics. This is a very challenging application for many inspection methods but is reasonably easy and fast using a microwave system. These were all reasonably large wrinkles with low aspect rations. Further tests can be carried out with smaller, more subtle wrinkles.

A summary of the aspect rations is as follows:

Length		
L_A = 209.3mm	Measured L_A = 200mm	Delta L_A = 4.7%
L_B = 113.7mm	Measured L_B = 105mm	Delta L_B = 8.3%
L_C = 259.5mm	Measured L_C = 245mm	Delta L_C = 5.9%
L_D = 194.7mm	Measured L_D = 190mm	Delta L_B = 2.5%

Centerline Distance		
A-C = 121.67mm	A-C = 125mm	Delta A-C = (-) 2.7%
A-B = 52.9mm	A-B = 50mm	A-B = 5.8%
C-D = 108.667mm	C-D = 120mm	C-D = (-) 9.4%

Aspect Ratio

A - W = 26.4mm, T = 5.316mm, AR = 4.97

B - W = 28.7mm, T = 7.309mm, AR = 3.92

C - W = 22.6mm, T = 3.966mm, AR = 5.69

D - W =15.24mm,T = 6.519mm, AR = 2.34

6 SUMMARY OF TESTING AT CARBON RIVERS

Team members traveled to the CR Powerhouse blade laydown yard in Kingston, Tennessee on October 14-17, 2024. The laydown yard possesses reclaimed blades from most major U.S. deployed wind turbine platforms and rotor diameters ranging from 34 meters up to 162 meters. An aerial image of the CR Powerhouse blade laydown yard is shown in Figure 6-1.

Figure 6-21. Aerial view of Carbon Rivers blade laydown yard in Kingston, TN. Credit: Google Earth

After evaluating hundreds of different blade sections at the laydown yard, seven sections were selected for NDE testing that spanned the entirety of the blade. A summary of the blade sections scanned at CR is shown in Table 6-1. Each blade section represents a different wind turbine blade make/model. Additionally, the selected blade sections included several flaws and features of interest, including delamination, voids, root hardware and interlaminar lay-up characteristics, quantitative characteristics of internal reinforcements (scanned externally), fiber wrinkles, bond line integrity, and factory (pre-commissioning) repairs.

Table 6-4. Sections used for NDE testing demonstration with flaws identified according to EPRI's Blade Anomaly Dictionary.

Section #	Approx. Section Location on Blade	Material(s)	Flaw as defined by EPRI's Blade Anomaly Dictionary	Photo(s)
1	Outboard 33%	Fiberglass, balsa wood, gel coat	Delamination, bond anomalies	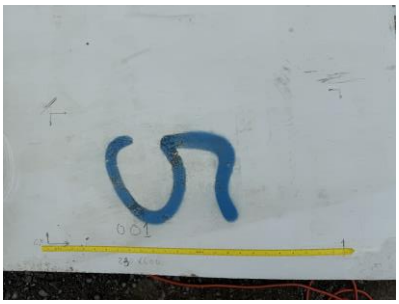 

2	Root	Steel, bolt inserts, bolts, fiberglass, gel coat	Root insert gaps, root laminate delamination	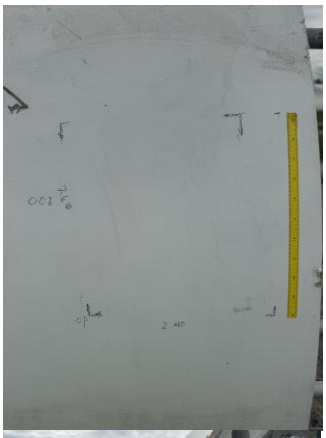 
3	Root	Steel, bolt inserts, bolt shroud fabric, fiberglass, gel coat	Root insert gaps, root laminate delamination	 

4	Midboard 33%	Fiberglass, foam core, adhesive gel coat	Internal blade reinforcements, surface gouges	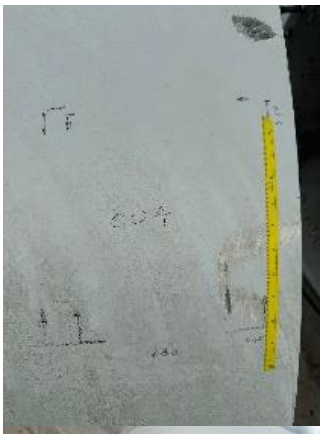 
5	Outboard 33%	Fiberglass, balsa wood, adhesive woven carbon fiber, gel coat	Fiber wrinkles, bond anomalies, delamination	 

6	Outboard 33%	Fiberglass, balsa wood, gel coat, adhesive	Bond anomalies, end of bond line bead, bond line thickness	
7	Root composite	Fiberglass, balsa wood, gel coat, repair patches	Single shot blade geometry, factory repairs	 

7 SUMMARY OF TEST RESULTS AT CARBON RIVERS

This section presents a brief description of the NDE test results from scanning the blade sections highlighted in Section 6, as well as a summary of the ultrasonics testing (UT) and microwave (MW) advanced techniques deployed. The blade sections selected for the demonstration are representative of the blade materials and geometries found in most larger wind turbine blades and have similar characteristics as to what can be found in OSW blades. The goal of inspecting the comparable blade sections is to demonstrate the capability of tools available in the market to inspect the OSW turbine blade materials to detect flaws, defects, and damages. Further, the results from this advanced NDE technique evaluation will serve as a platform for development of the techniques for the scale, materials and characteristics of OSW blades.

7.1 Testing of Advanced Ultrasound Techniques

The UT instrument used was the Zetec Emerald 64/128, a device capable of FMC and PWI acquisition and real-time TFM display. It is compatible with both conventional monocrystal UT search units and phased array UT probes.

All eight sections photographed and described in **Error! Reference source not found.** were assessed for favorable conduct of UT or not, via free scanning (i.e., not encoded) using two conventional monocrystal probes of one inch diameter and of center frequencies of 0.5MHz and 1.0MHz. The probe attributes are shown in Table 7-1. The two probes differed only by their center frequency; they were 0.5MHz and 1.0MHz. In the case of favorable UT responses, they would also be used to measure the sound speed in the bulk material.

The performance of UT was not strong in specimens with cores of either foam or wood (sections 1, 5 and 6) due in part to the low stiffnesses and high attenuation of these materials but also due to the high impedance mismatch between the many layers in the internal structure. It was generally not possible to retrieve a backwall reflection using either conventional probe listed in Table 7-1.

Furthermore, though sections 2 and 3 may appear similar in the photography from **Error! Reference source not found.**, in that they are of similar sizes and thicknesses, there was a stark contrast in UT performance, with UT performing strongly in section 2 but poorly in section 3. A visual inspection reveals that there is a notable difference in structural composition, though not evident from the table. Section 2 is built from a dry layup of many thin layers assembled by machine from pre-impregnated lamina sheets. Section 3, by contrast, is built from a wet layup comprising heavier, thicker layers often assembled by hand with applied adhesive. The latter process often yields a higher concentration of aid voids between layers.

Overall, it was found that sections 2, 4 and 7 responded the most favorably to ultrasonic propagation. The longitudinal sound speed was measured as 4882ms^{-1}, corresponding to fiberglass in the built-in material library.

Two different phased array probes, whose attributes are listed in Table 7-2, were used to scan these blade sections. The scan plan attributes are listed in Table 7-3 with the qualitative features of interest in the scan; typically either the OD of machined holes (see photograph for the second specimen in **Error! Reference source not found.**) or to visualize the internal interfaces between the different materials in the composition. To obtain a strong focusing within each specimen, FMC/TFM was used for insonfication and image reconstruction [1].

Using only a string encoder, probe movement was along one dimension, with the greater dimension of the probe aperture, and also the region of interest, oriented perpendicularly to the direction of movement. Indexing was accomplished simply by merging multiple such one-line scans together in a graphics engine built in-house at EPRI for volumetric data visualization.

Table 7-1. Attributes for the conventional monocrystal UT probes used to assess UT performance and sound speed in the blade sections

Probe ID	**C16206**	**A1028-48161**
Manufacturer	KB-Aerotech	Panametrics-Accuscan
Centre Frequency	0.5MHz	1.0MHz
Shape	circular	circular
Diameter	25.4mm	25.4mm
Pulse Width	1000ns	500ns

Table 7-2. Phased array UT probe attributes used to scan the blade sections

Probe ID	**10030-N1862**	**11506-1060**
Manufacturer	Olympus	Imasonic
Centre Frequency	2.25MHz	5.0MHz
Element Count	60	64
Pitch	1.0mm	0.6mm
Elevation	10.0mm	10.0mm
Pulse Width	222ns	100ns
Active Aperture	60.0mm	38.4mm

Table 7-3. Summary of scan plans shown in this section

Specimen	**PA Probe**	**Orientation**	**Indexing Range (in.)**	**Frame size (in.)**	**Frame resolution**
2	10030-N1862	axial	range(1,9,2)	3.0×4.0	320×384
4	11506-1060	circ.	range(1,11,2)	1.8×1.8	384×384
4	10030-N1862	circ.	range(1,11,2)	2.0×2.0	192×256
7	11506-1060	circ.	range(-2,12,2)	2.5×2.5	512×512
7	10030-N1862	circ.	range(-2,12,2)	2.5×2.5	512×512

Figure 7-1. Photographed UT probes used in this work; from top left: (a) 0.5MHz monocrystal; (b) 1.0MHz monocrystal; (c) 2.25MHz phased array; (d) 5.0MHz phased array

7.1.1 Blade Section #2

Section #2 takes the form of a pipe with a regular cylindrical curvature at the OD (the scan surface). The diameter, being in the order of seven feet, was not measured precisely, though the thickness was measured as 3.5in at the accessible end of the structure, with a taper at the ID, such that its thickness decreases as one moves farther from the end. The features of interest in this section are a series of Ø1.5in. holes of approximately 10in. depth, spaced by approximately 4.5in. center-center. Scanning was carried out only axially, parallel to the axis of said holes.

Annotated views of the volumetric data are shown in Figure 7-2. The indexing range covered two holes; whose positions are indicated by the dashed lines. Note that the axes are not necessarily to scale; hence the holes do not appear circular in the end view. In the top right corner of the side view, the specular reflection, the creeping wave around the hole and the second specular reflection are visible, along with the ID reflection. The top view and, to a lesser extent, the side view, reveal interesting circular features at the ends of the hole, likely resulting from diffraction from the tip.

The volumetric view demonstrates the viability of UT to track the thickness of the part up to long sound paths of three inches or greater, and to indicate the presence of reflectors within the bulk material.

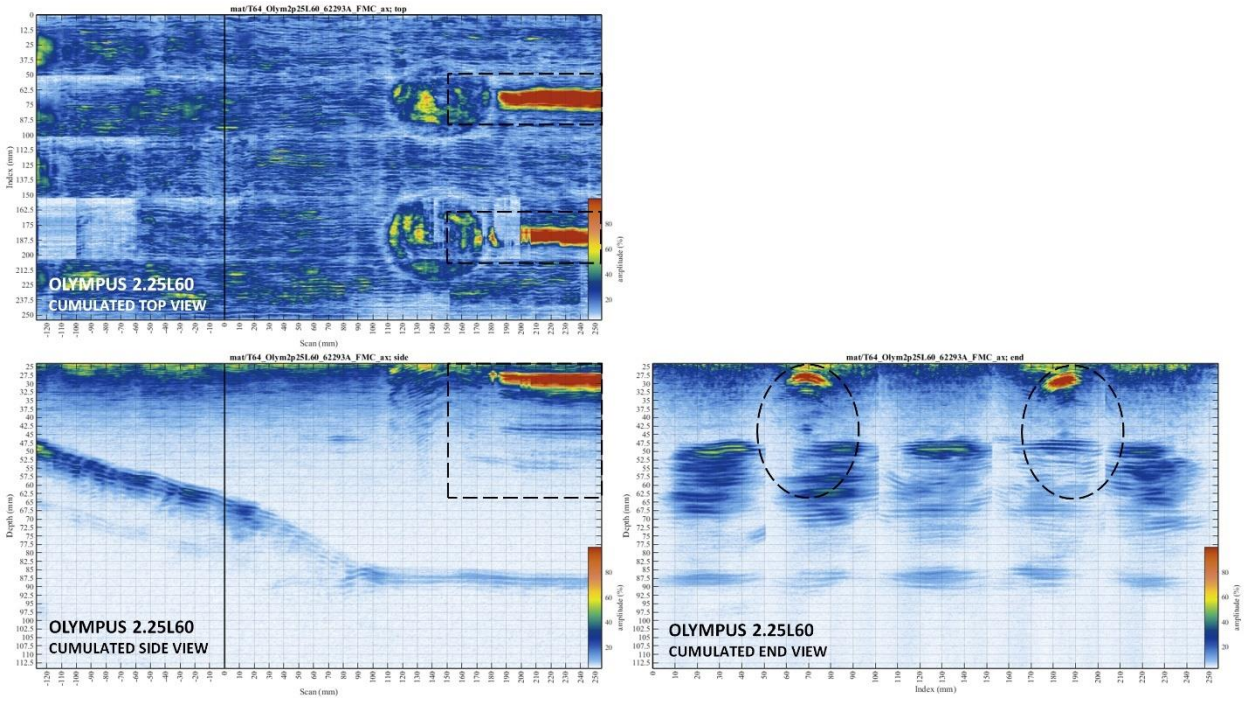

Figure 7-2. Composited view of volumetric TFM data acquired from axial scan of Section #2, showing (a) top view; (b) side view and (c) end view

7.1.2 Blade Section #4

Section #4 is from the midboard near the root, with a nearly circular shape and with a composition that includes more than one material, unlike the component section #2. In this There is neither hole nor known feature of interest. There is instead an interface between the two materials of generally constant depth (approximately 1.5in.) and an ID of varying depth, as photographed in Figure 7-3 and as captured by a TFM scan using the 5MHz Imasonic probe. The scan intermittently captures the interface and the backwall reflection, with gaps caused by one or more of the following factors:

- Surface irregularities or damage, as evident from the photograph in Figure 7-3, affecting the contact of the probe;
- Angle of the backwall that is unfavorable to the receiving probe;
- Morphology of the ID not providing a reflecting surface for ultrasound.

The cumulated side view as captured by the 2.25MHz Olympus probe is shown in Figure 7-4. Due to slight variation of the structure along the axial direction, the resulting cumulated view appears a little blurry. It is demonstrated that TFM focused from data captured by either probe is sufficiently capable of reconstructing the interface and the backwall so that the overall thickness and the bonding quality at the interface can be assessed.

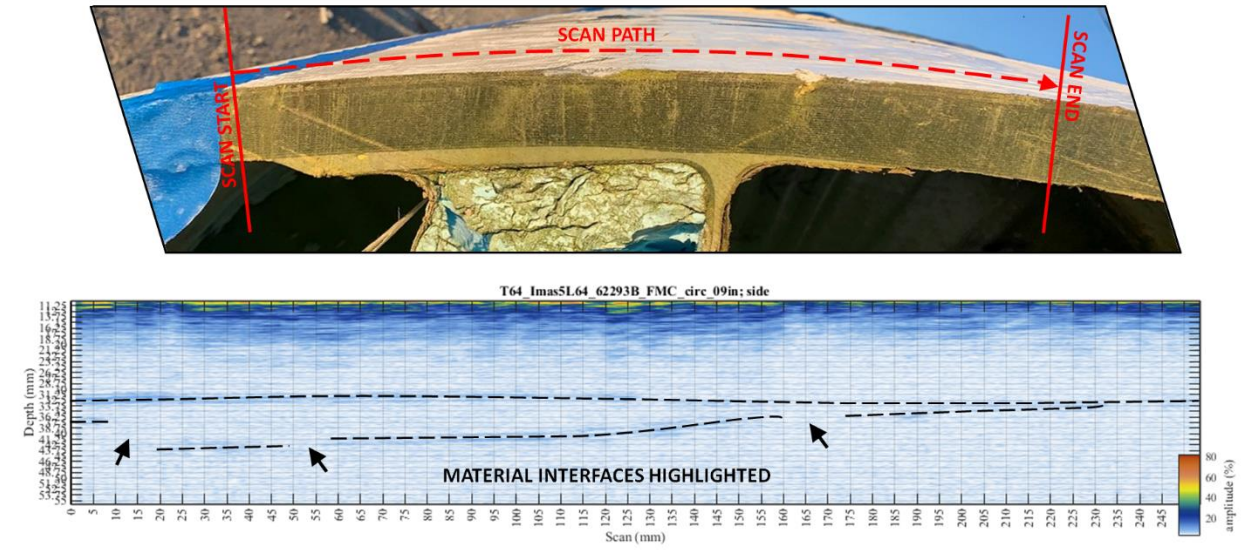

Figure 7-3. (a) Photograph from the end of Section #4 and (b) a corresponding annotated side view of volumetric TFM data captured by the 5MHz Imasonic probe

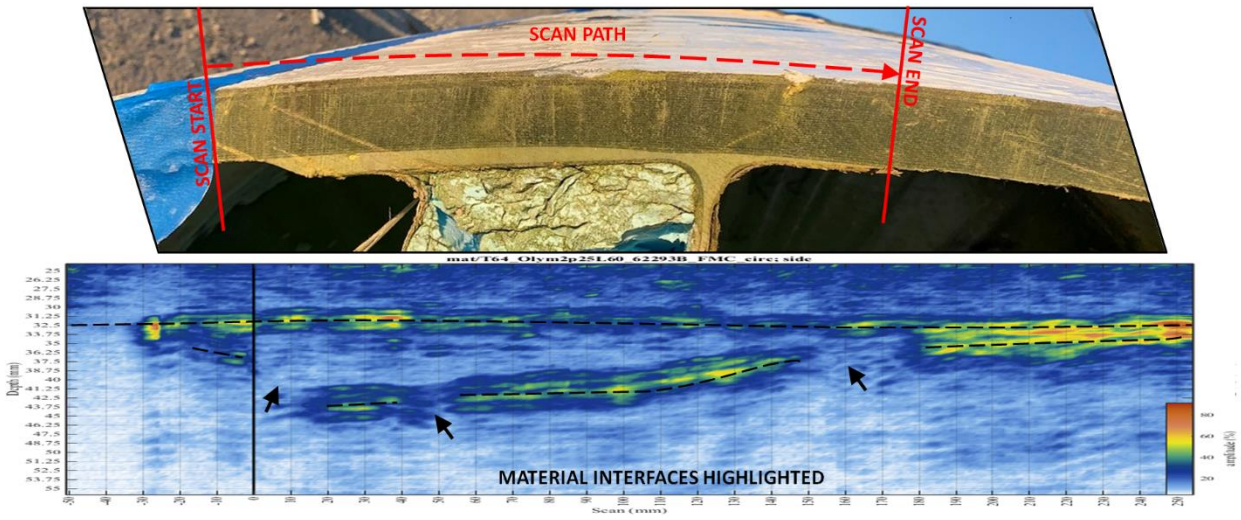

Figure 7-4. (a) Photograph from the end of Section #4 and (b) a corresponding annotated side view of volumetric TFM data captured by the 2.25MHz Olympus probe

7.1.3 Blade Section #7

Section 7 is from the root of a different blade to those presented above. At this section, the shape is more oval than circular, with a composition that appears, from a visual inspection, to be of three distinct materials. The overall thickness varies from 1.5in. to 2.25in. Only circumferential scans were applied from the OD.

The OD upon which the probes were physically scanned is photographed in

Figure 7-5. Microwave scanning was also applied this same region, as discussed in §7.2.7, which detected two items of potential interest. Said items were located at (scan, index)=(5.5,1.0)in. and (5.5,11.0)in., according to the coordinate system used for UT scanning, and are indicated by black arrows in

Figure 7-5. Slices at indices closest to these features are shown in Figure 7-6, where possible indications in the volume are also indicated by black arrows. There is potential correlation with the microwave scanning results though these indications are rather too weak to conclude this definitively.

As shown in

Figure 7-7, the UT scanning reveals the presence of material interfaces in cases where the interface is oriented favorably so as to reflect a higher proportion of energy back to the probe position. In the strongest case, near the middle of the scan range, up to four interfaces are visible. However, there are still gaps in the tracking of the interfaces, for the same reasons as listed in the bullets in 7.1.2.

Just as in the case of Section #4, the internal structure is not consistent with depth (or index position, in the context of these UT scans). Observing the side views at different scan indices illustrates these changes. We also see evidence of this from the composited end view, shown in Figure 7-8.

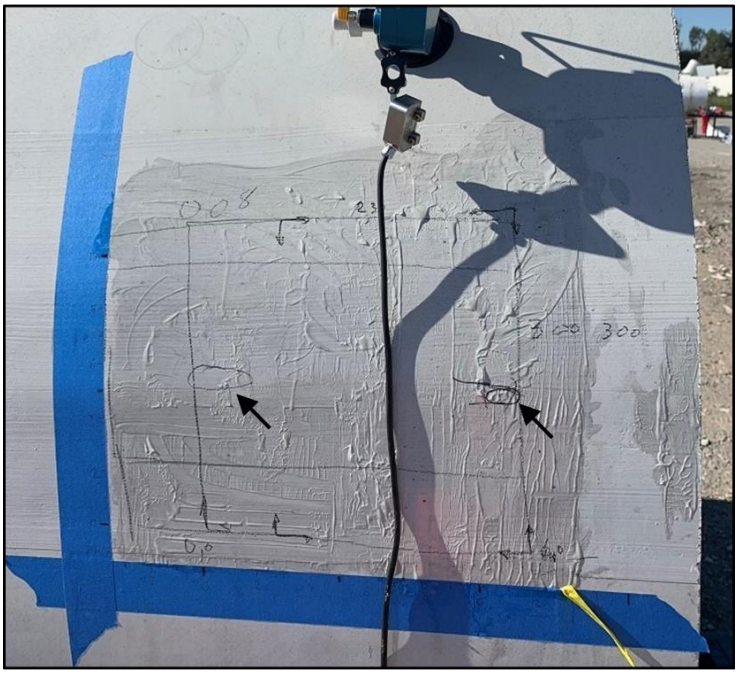

Figure 7-5. Scanning area at the OD of Section #7. Suspected reflectors of interest are indicated by the two black arrows

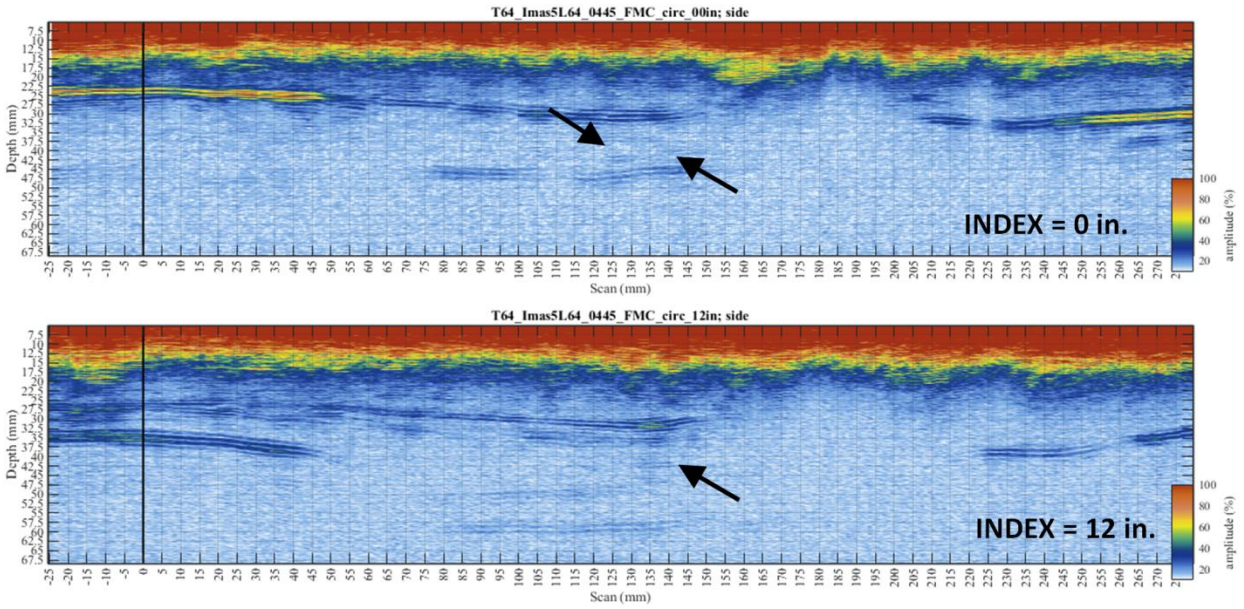

Figure 7-6. Side views at (a) index=0.0in. and (b) index=12.0in., which slice the scan volume so at the locations of suspected reflectors of interest indicated in

Figure 7-, which are indicated by black arrows

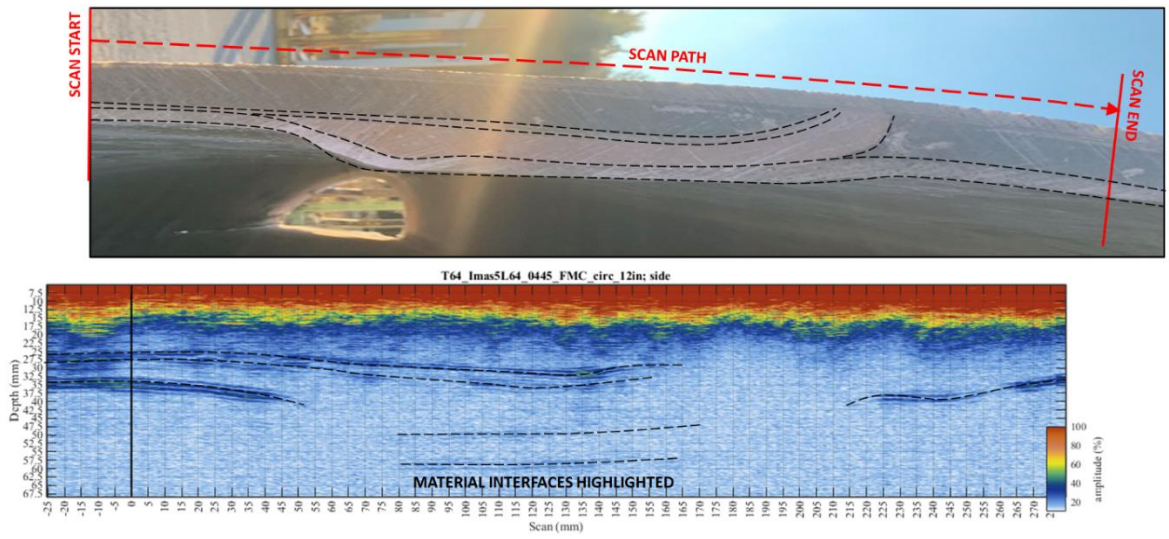

Figure 7-7. (a) Photograph from the end of Section #7 and (b) a corresponding annotated side view of volumetric TFM data captured by the Imasonic 5MHz probe

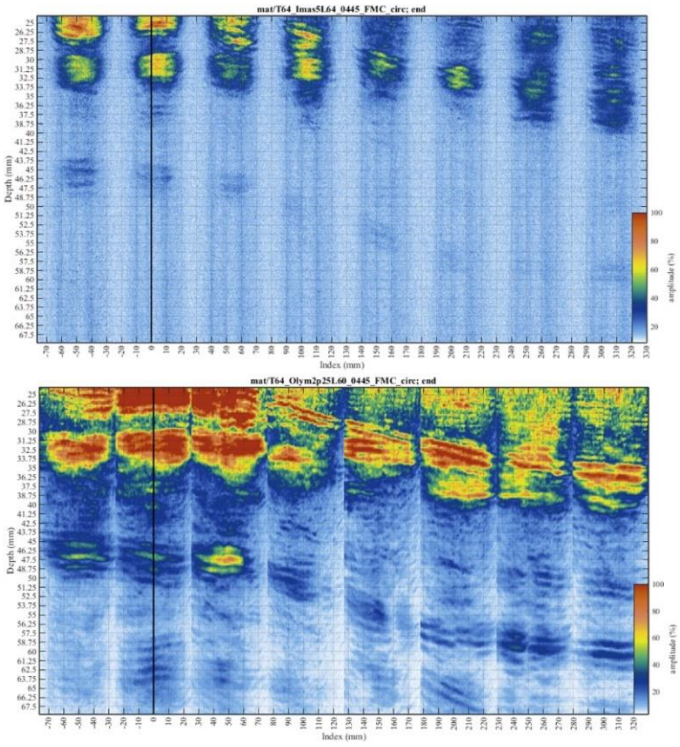

Figure 7-8. End view of Section #7 composited from volumetric UT data acquired by (a) the Imasonic 5MHz probe and (b) the Olympus 2.25MHz probe

7.2 Testing of Advanced Microwave Techniques

The eight sample sections described in Table 7-1 were inspected using the Advanced Microwave Imaging Motorized Axis Portable Scanner (MAPS) system. This system is currently in use for field inspections of wind turbine blades.

Figure 7-9. AMWI MAPS System in Use

The blade samples were inspected using the typical MAPS setup as follows:

- Microwave Frequency Range: 6–14 GHz
- Datapoints: 201
- Antenna Position: 5–7 mm above surface
- X and Y Step Size: 10 mm
- Scanning Speed: 20 mm/sec (stop at inspection point)

This configuration enables high-resolution imaging of subsurface features, including bond lines, voids, wrinkles, and delamination in composite blade structures.

7.2.1 Blade Section #1

Blade Section #1 was inspected using the MAPS system to assess its internal and external structural integrity. Microwave imaging was used to identify anomalies such as bonding issues, delamination, embedded wrinkles, or voids.

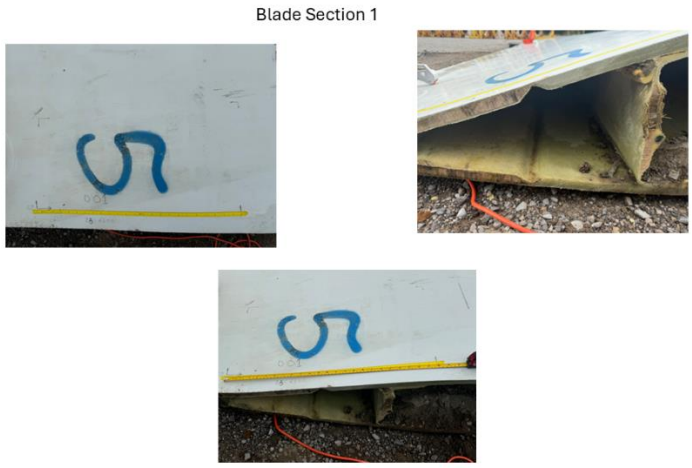

Figure 7-22. Image of inspection zone

Microwave Inspection Results:

Key observations:

1. Trailing edge bond - lack of bond or bond paste
2. Trailing edge bond – bond paste likely not applied uniformly
3. Disbonds between outer shell and bond cap – May have occurred when cutting blade apart, but multiple disbonds were detected.

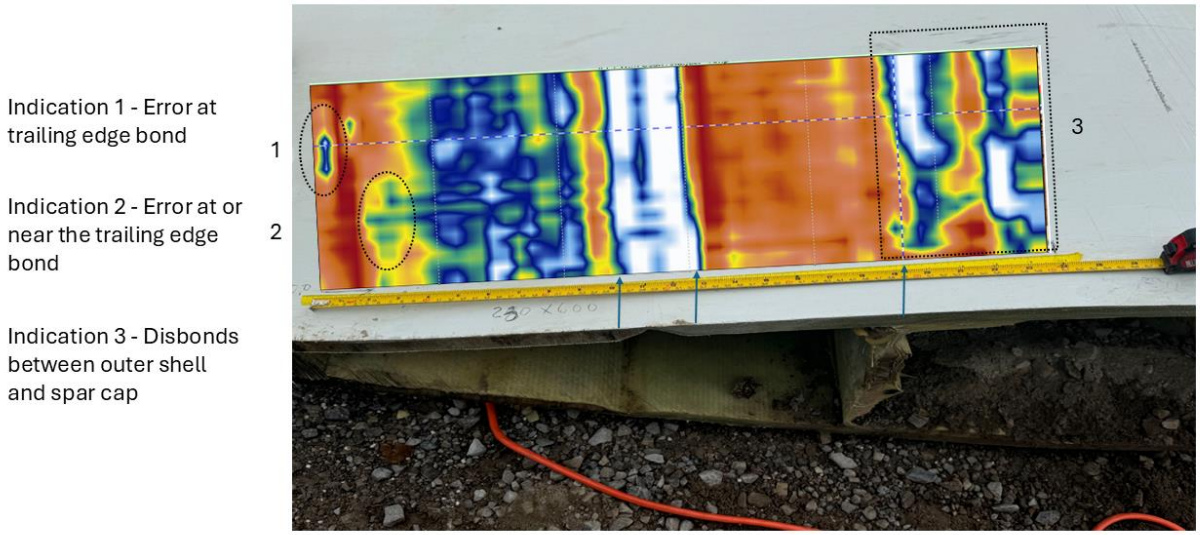

Figure 7-23. AMWI Microwave Inspection image overlay on part showing flaw location

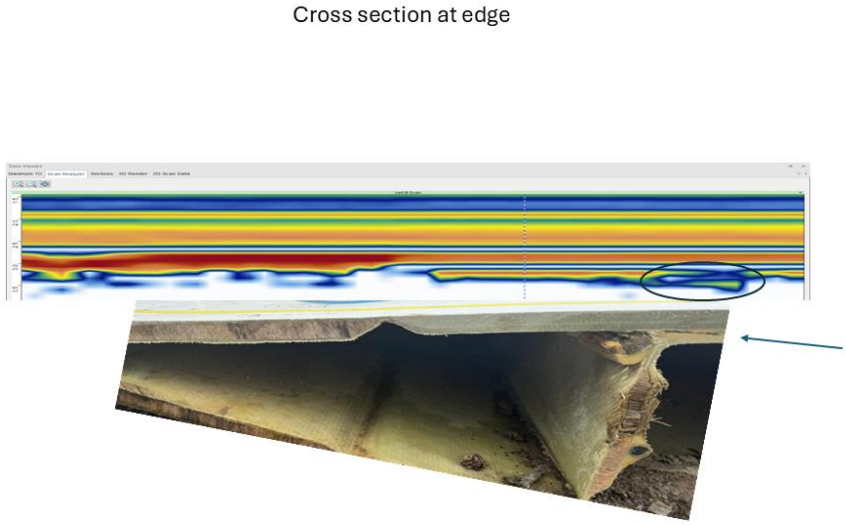

Figure 7-24. Inspection cross section using Horizontal B identifying delamination at spar cap

Additional Commentary:

Advanced microwave imaging provided clear visualization of defects within this section. The identified flaw types—such as disbonds and bond paste errors demonstrate the system's ability to detect and spatially resolve flaws through layered materials and bonding interfaces. These insights are crucial for evaluating both manufacturing consistency and in-service degradation.

7.2.2 Blade Section #2

Blade Section #2 was inspected using the MAPS system to assess its internal and external structural integrity. Microwave imaging was used to identify anomalies such as bonding issues, delamination, embedded wrinkles, or voids.

Figure 7-253. Inspection Site 2 – Blade Root

Microwave Inspection Results:

Key observations:

1. Stud locations and barrel nut identified
2. One rounded void indication was identified between two studs

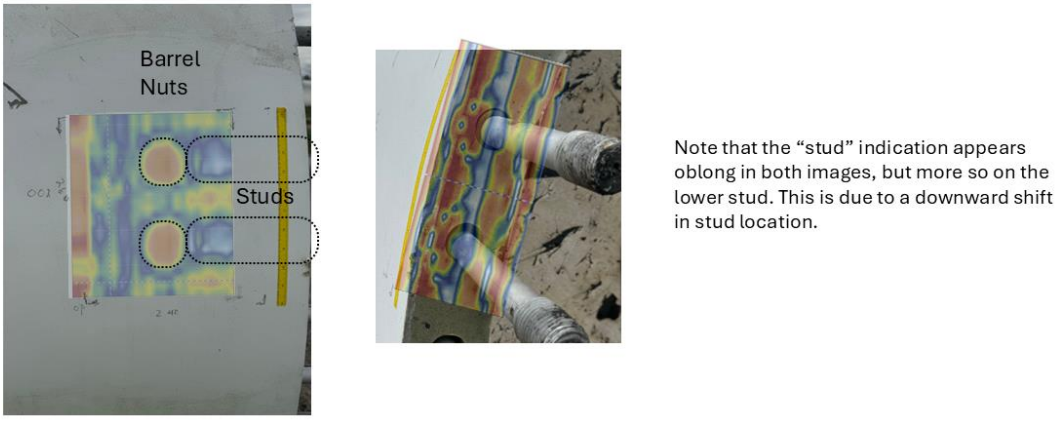

Figure 7-264. Root Top view and cross section showing construction detail

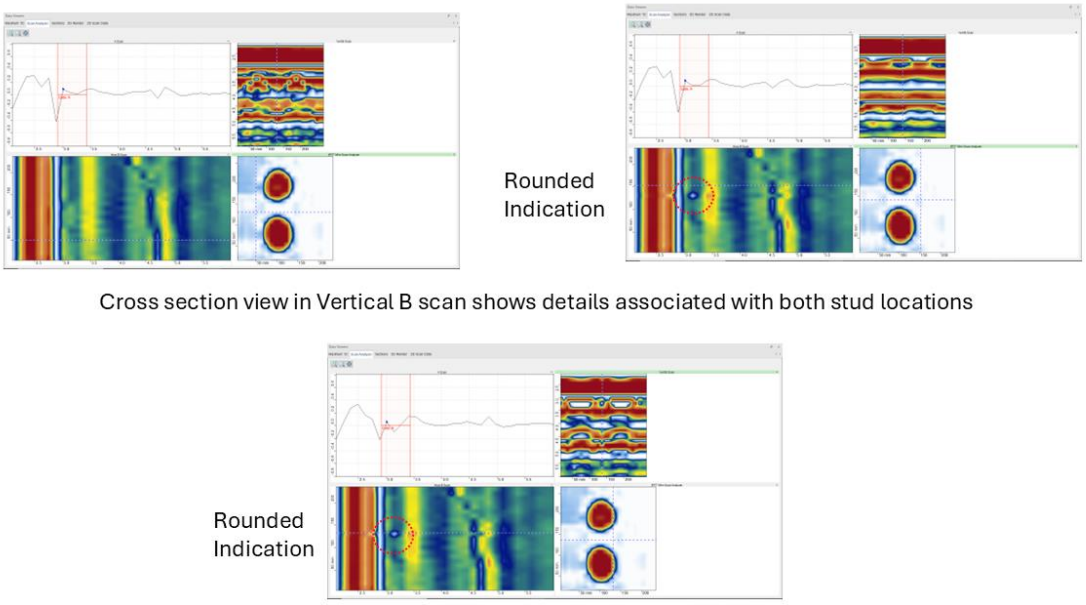

Figure 7-275. Inspection Images with rounded indication mid stud

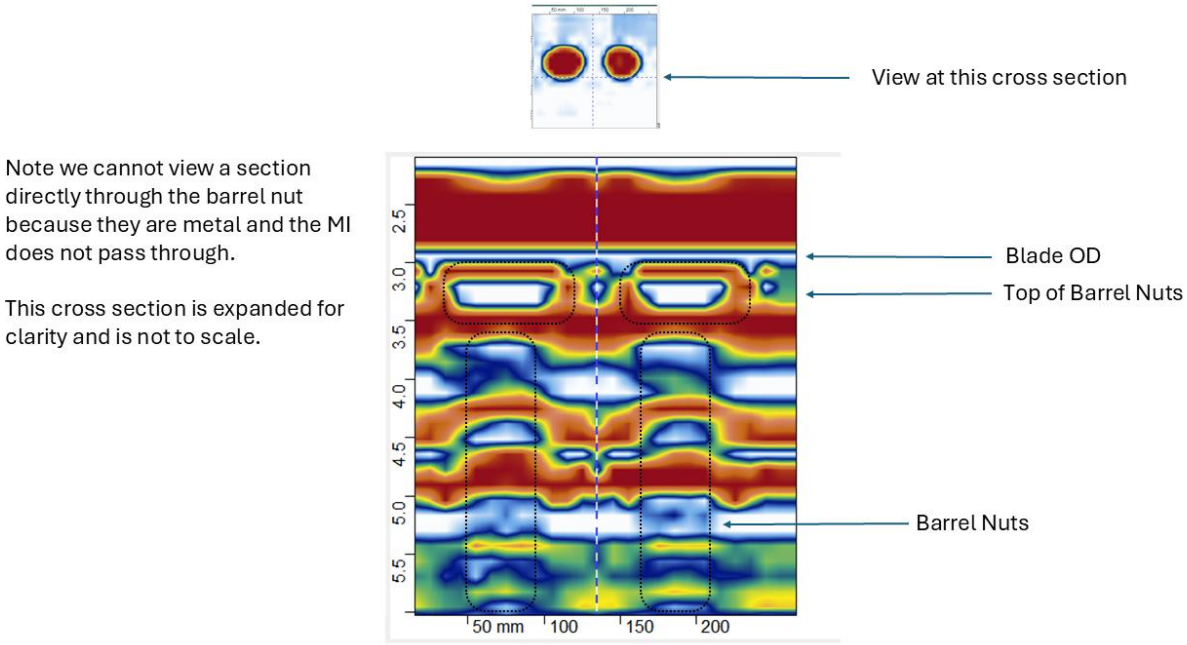

Figure 7-286. Cross section of root area

Additional Commentary:

Advanced microwave imaging provided clear visualization of features within this section. The identified flaw types—such as a rounded, void demonstrate the system's ability to detect and spatially resolve layered materials and bonding interfaces. These insights are crucial for evaluating both manufacturing consistency and in-service degradation.

7.2.3 Blade Section #3

Blade Section #3 was inspected using the MAPS system to assess its internal and external structural integrity. Microwave imaging was used to identify anomalies such as bonding issues, delamination, embedded wrinkles, or voids.

Blade Section 3

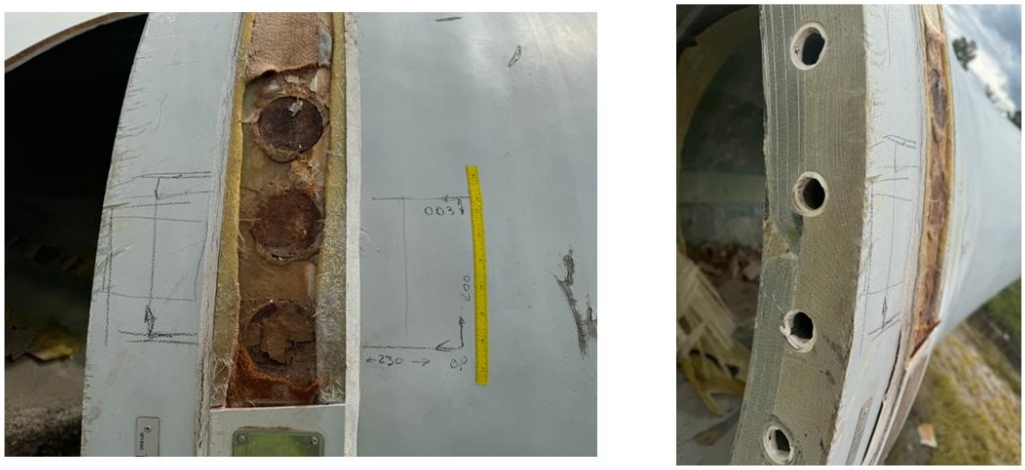

Figure 7-297. Section 3 Root with no studs

Microwave Inspection Results:

Key observations:

1. One rounded indication identified between the two barrel nuts that appears to be a void or delamination at that location.

2. No other indications identified.

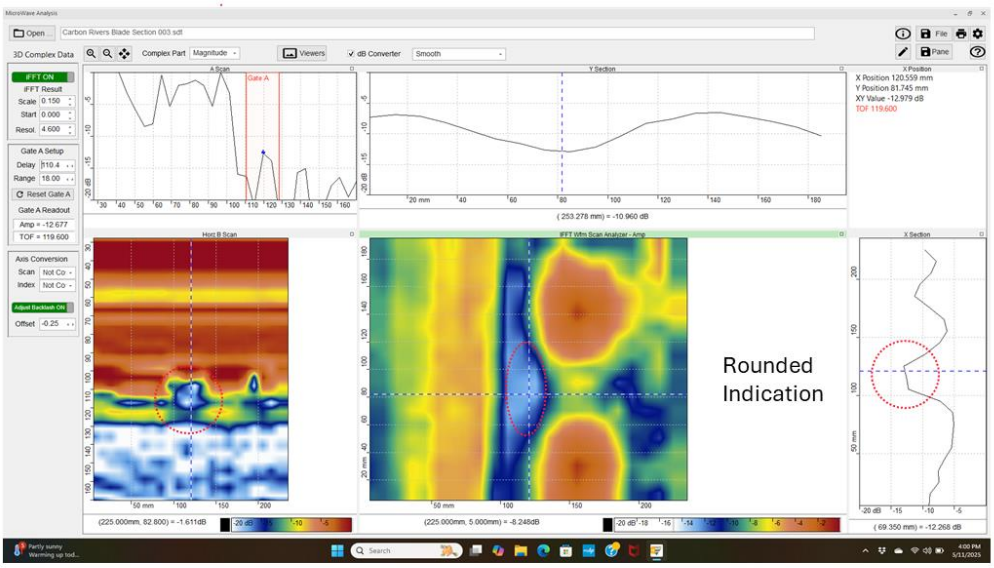

Figure 7-308. Root section with rounded indication

Additional Commentary:

Advanced microwave imaging provided clear visualization of defects within this section. The identified flaw types—such as voids or delamination—demonstrate the system's ability to detect and spatially resolve layered materials and bonding interfaces. These insights are crucial for evaluating both manufacturing consistency and in-service degradation.

7.2.4 Blade Section #4

Blade Section #4 was inspected using the MAPS system to assess its internal and external structural integrity. Microwave imaging was used to identify anomalies such as bonding issues, delamination, embedded wrinkles, or voids.

Blade Section 4

Figure 7-19. Mid span with internal reinforcement

Microwave Inspection Results:

Key observations:

1. Delamination at GFRP to bond paste in several regions of the spar to blade tapered bon paste.

2. No other indications identified

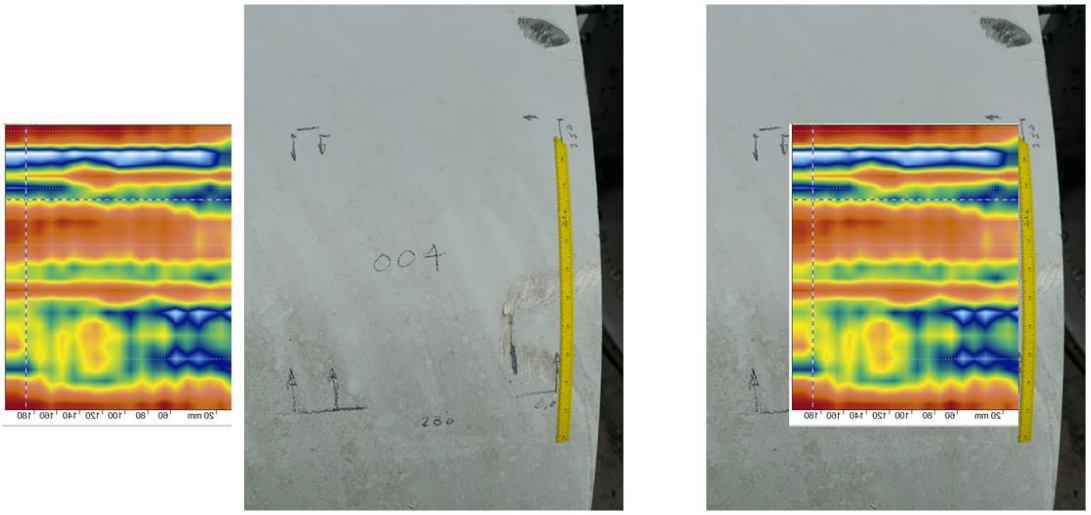

Figure 7-310. Inspection image in plain view

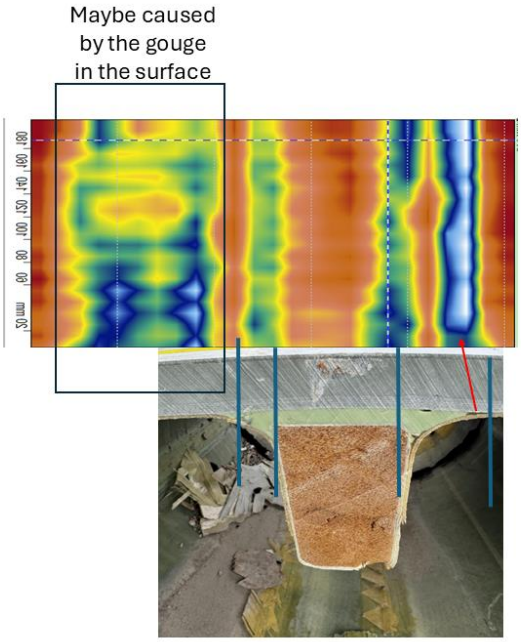

Figure 7-321. Microwave inspection showing detection of flaws in bond paste levels

Additional Commentary:

Advanced microwave imaging provided clear visualization of defects within this section. The identified flaw types—such as [insert flaw type]—demonstrate the system's ability to detect and spatially resolve layered materials and bonding interfaces. These insights are crucial for evaluating both manufacturing consistency and in-service degradation.

7.2.5 Blade Section #5

Blade Section #5 was inspected using the MAPS system to assess its internal and external structural integrity. Microwave imaging was used to identify anomalies such as bonding issues, delamination, embedded wrinkles, or voids.

Figure 7-33. Carbon Fiber spar cap section

Microwave Inspection Results:

Key observations:

1. Wrinkle – Wrinkle in CFRP spar cap identified.
2. Edges of CFRP Spar located.
3. Two bond line (CFRP Spar to GFRP) located and detected.

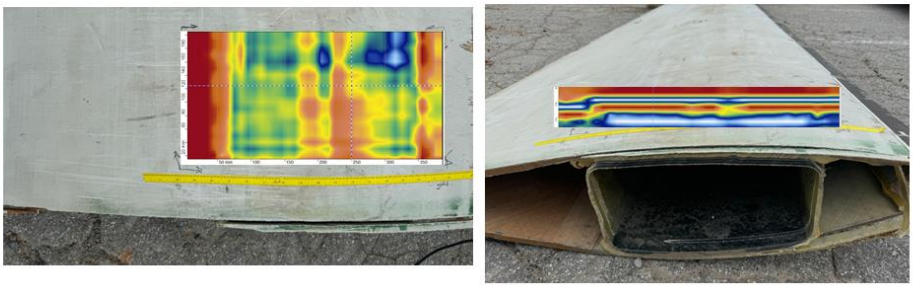

Figure 7-34. Plan and section detail of microwave inspection

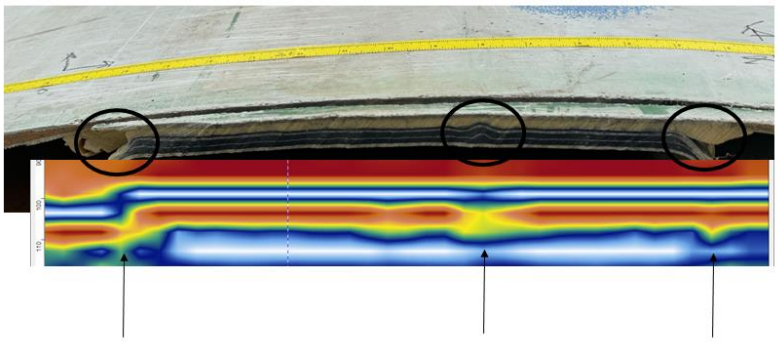

Figure 7-35. Close up comparison of Horizontal B image and blade cross section

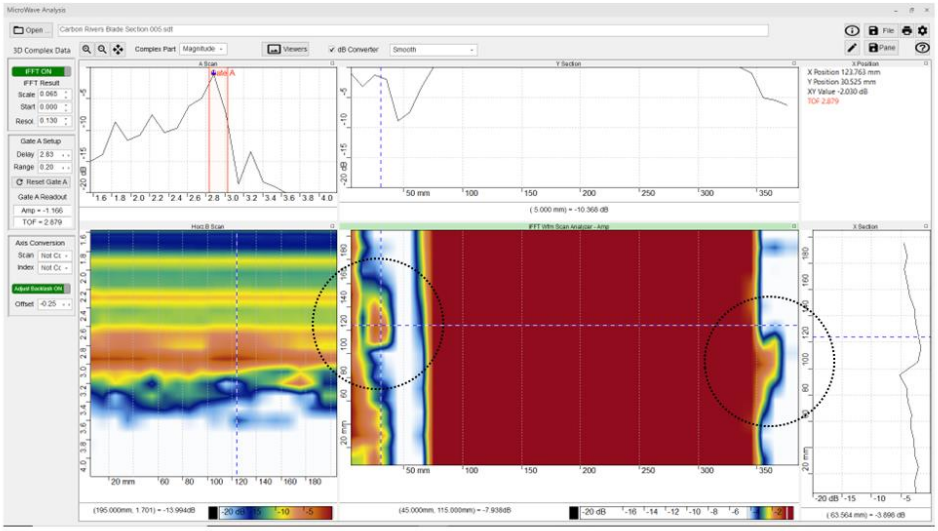

Figure 7-36. C Scan at depth showing detection of bond paste flaws at edge of carbon fiber

Additional Commentary:

Advanced microwave imaging provided clear visualization of defects within this section. The identified flaw types—such as wrinkles and bond line flaws—demonstrate the system's ability to detect and spatially resolve layered materials and bonding interfaces. These insights are crucial for evaluating both manufacturing consistency and in-service degradation.

7.2.6 Blade Section #6

Blade Section #6 was inspected using the MAPS system to assess its internal and external structural integrity. Microwave imaging was used to identify anomalies such as bonding issues, delamination, embedded wrinkles, or voids.

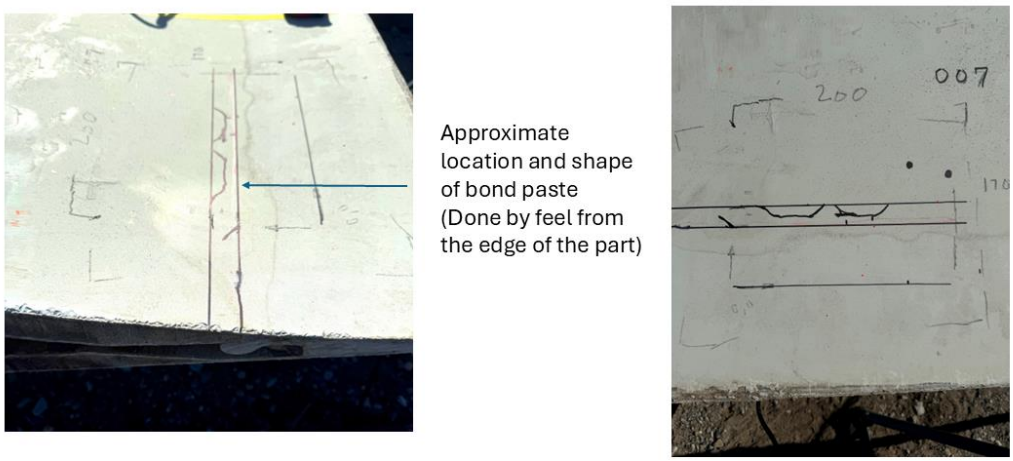

Figure 7-37. Blade trailing edge showing approximate location of internal edge of bond paste

Microwave Inspection Results:

Key observations:

1. Detect and locate edge of bond paste from OD or ID.
2. Identified areas where bond paste did not migrate during application (i.e. – squeeze) leaving an area without paste.
3. Insufficient bond paste squeeze may result in an insufficiently bonded part.

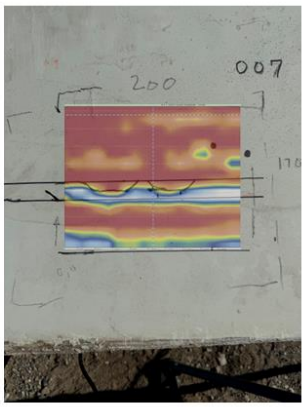

C scan overlay on part shows approximately the same shape as the “drawn in” bond paste shape

Figure 7-38. Microwave C scan at depth shows ability to map edge of bond paste to validate proper squeeze out

Additional Commentary:

Advanced microwave imaging provided clear visualization of defects within this section. The identified flaw types—such as bond paste edge and squeeze - demonstrate the system’s ability to detect and spatially resolve layered materials and bonding interfaces. These insights are crucial for evaluating both manufacturing consistency and in-service degradation.

7.2.7 Blade Section #7

Blade Section #7 was inspected using the MAPS system to assess its internal and external structural integrity. Microwave imaging was used to identify anomalies such as bonding issues, delamination, embedded wrinkles, or voids.

Top Down Image | End Image | Interior Image at Scan

Figure 7-39. Edge of blade repair section

Microwave Inspection Results:

Key observations:

1. Stacked delamination (multiple delamination in same XY location but differing Z location) in repair.

2. Able to track ID thickness changes using Horizontal B (time of flight) data.

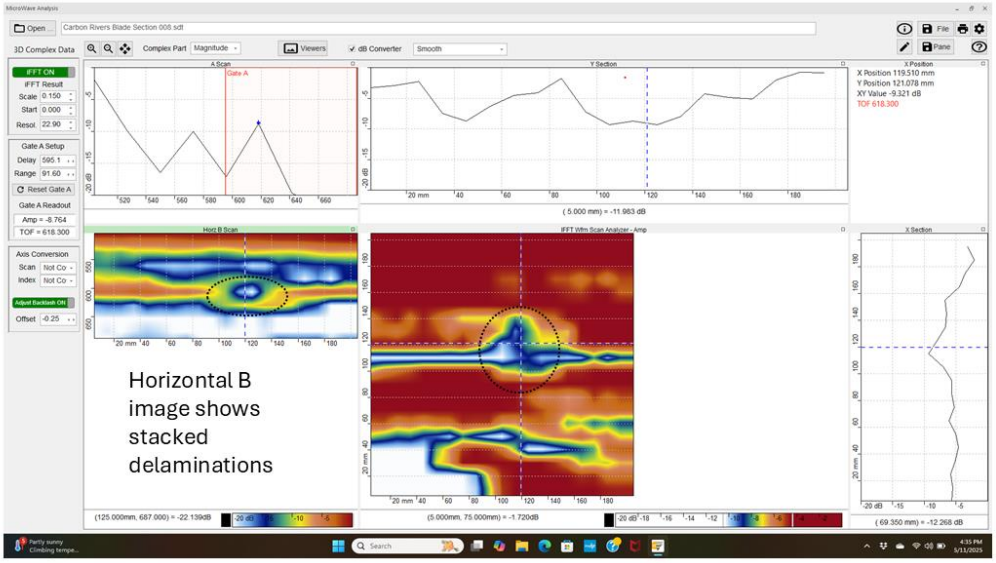

Figure 7-40. Horizontal B image shows ability to detect and locate stacked flaws within part

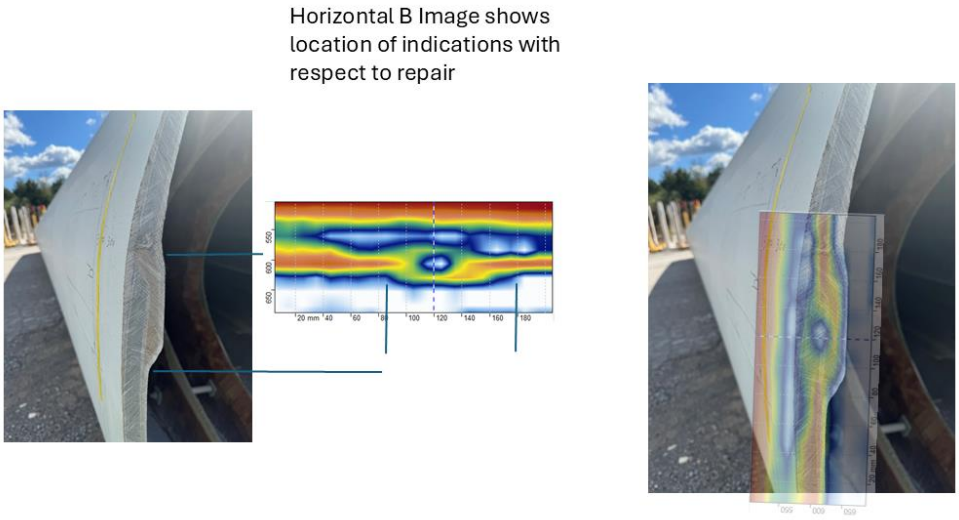

Figure 7-41. Horizontal B image compared to part edge to validate ability for microwave imaging to track varying blade wall thickness in the presence of delamination

Additional Commentary:

Advanced microwave imaging provided clear visualization of defects within this section. The identified flaw types—such as stacked delamination— as well as the ability to track varying blade thicknesses demonstrate the system's ability to detect and spatially resolve layered materials and bonding interfaces. These insights are crucial for evaluating both manufacturing consistency and in-service degradation.

8 SUMMARY AND CONCLUSIONS

This report summarizes the exploration and evaluation of ultrasonic and microwave testing techniques for the purposes of identifying flaws in offshore wind turbine blades. The evaluation of these techniques was first performed with mockup samples which were utilized in previous wind power research projects. Samples from previous R&D efforts related to the inspection of wind blades were tested to demonstrate the feasibility of applying ultrasonic methods and microwave methods in CFRP and GFRP samples, respectively. For ultrasonics, PWI/TFM were used for the inspection of a CFRP sample. The results from testing indicate that there is a difference in detectability based on the orientation of the probe and this should be considered in the procedure development of the technique. A significant volume near the surface was saturated. The presence of a wedge would likely reduce the saturation but would introduce internal wedge reflections. For inspecting a specific thickness, the selection of a wedge should be considered. For the microwave technique, data was collected with tabletop and portable scanners. A multi frequency probe was used and different analysis methods were employed to visualize the defects. The different analysis techniques show that some defects are better detected than others. It is likely that in an inspection scenario with unknown defects, all microwave analysis methods utilized in this study would need to be applied to arrive to a conclusion.

As part of this project, four different types of panel fiberglass samples and a set of carbon fiber reinforced samples representative of real-world wind turbine blade manufacturing techniques and materials were tested and analyzed. The panels included some potential flaws that could occur during their manufacture as a means of establishing whether they can be reliably detected using a multi-frequency microwave inspection system. For the CFRP samples, ultrasonic techniques were evaluated for their feasibility and application. The equipment used is commercially available and TFM/FMC and PWI/FMC analysis was performed. The results from testing allowed the operator to locate the pre-drilled holes added to samples. Ine interesting observation was that the CFRP panels were made of several layers of CFRP bonded together. The test results indicate that the boundary of the layers along the thickness of the panel can be observed. This is important because in a real-world application, the reflection of the interfaces can provide an approximation of the location of the defect. For the fiberglass panels and panels with multilayered materials, the microwave system provided detection information related to ply drops, delamination, porosity, and bond paste flaws through 50 mm (2 in.) of balsa and 50 mm (2in.) of foam. When testing the porosity samples and performing a calibration of the porosity, the system is capable of detecting and approximating the percentage of porosity and the areas of localized porosity within GFRP.

Blade sections with representative scale, geometry, and flaws or defects were tested at CR to demonstrate the feasibility of applying ultrasonic methods and MW methods in carbon fiber and glass fiber reinforced OSW blades. For ultrasonics, FMC/TFM was used for inspection of several blade sections. The volumetric UT data were acquired using phased arrays driven by a portable UT instrument from a vendor of NDE equipment. Positional encoding was used in both

axial and circumferential scans. Though a portion of the volume near the surface was saturated due to coupling, this effect was mitigated by reconstructing the image deeper into the structure. The results were varied; several of the sections appeared to be impervious to ultrasonic energy. However, others responded favorably to ultrasonic interrogation and demonstrated the viability of the superior focusing of ultrasonic TFM to provide information regarding the internal structure. In the latter cases, multiple interfaces between different materials, in addition to the backwall, could be identified, though not consistently. Further UT development, including trial of TFM variants, such as PCI, should be considered for possible improvement of the SNR to enable more reliable tracking of material interfaces. For the microwave technique, data was collected with tabletop and portable scanners. A multi frequency probe was used and different analysis methods were employed to visualize the defects. The microwave techniques illustrate its capability to identify a plethora of composite material flaws in wind turbine blade sections. It is likely that in an inspection scenario with unknown defects, the microwave analysis methods would need to be accompanied with a validation methodology whether that be destructive assessment or another NDE technique. Greater certainty in MW NDE analyses will likely occur as the technique becomes more prevalent in the industry, but would benefit from the creation of a library or index to help with the verification and validation.

The test performed at CR demonstrates that the NDE techniques developed in this project are capable of identifying critical flaws in OSW turbine blades. The results from this demonstration and project provide a solid basis for continuing the development of the NDE techniques to assist on the inspection of OSW blades as a proactive maintenance approach.

9 REFERENCES

1. Full Matrix Capture (FMC) Standards and Code Development Interface: A Documentation of the Establishment of FMC Standards and Codes. EPRI, Palo Alto, CA: 2019. 3002015971.

2. D. Roach, S. Neidigk, T. Rice, R. Duvall, J. Paquette, " Blade Reliability Collaborative: Development and Evaluation of Nondestructive Inspection Methods for Wind Turbine Blades" SAND2014-16965, Unlimited Release, Printed September 2014

3. D. Roach, T. Rice, J. Paquette, "Probability of Detection Study to Assess the Performance of Nondestructive Inspection Methods for Wind Turbine Blades", Sandia national laboratories, SAND2017-8032, August 2017

4. K. Rackow, D. Roach, "Blade Reliability Collaborative – Round Robin Wind Turbine Blade NDI Feedback Specimens with Flaws", SANDIA National Laboratory, February 2011.

5. D. Roach, et al. "Development and assessment of advanced inspection methods for wind turbine blades using a focused WINDIE experiment." *33rd Wind Energy Symposium*. 2015.

APPENDIX – MICROWAVE SCANNING HARDWARE

Equipment:

Standard Multi-frequency System	
Table Top Scanning system Frequency Range 10GHz-18GHz 201 Data Points 10mm by 10mm scan/index and 5mm by 5mm scan/index Sample 680mm by 430mm (sample was split into two scans to accommodate SAR software) Scan time approximately 15 minutes (10 by 10) and 30 minutes (5 by 5) No couplant required (Air coupled)	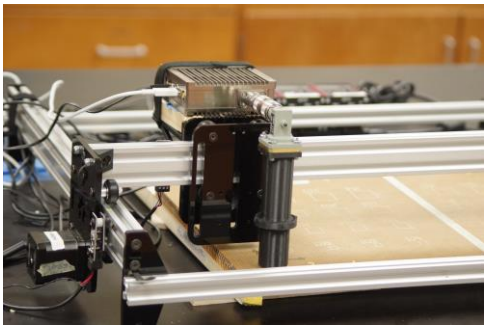

Export Control Restrictions

Access to and use of this EPRI product is granted with the specific understanding and requirement that responsibility for ensuring full compliance with all applicable U.S. and foreign export laws and regulations is being undertaken by you and your company. This includes an obligation to ensure that any individual receiving access hereunder who is not a U.S. citizen or U.S. permanent resident is permitted access under applicable U.S. and foreign export laws and regulations.

In the event you are uncertain whether you or your company may lawfully obtain access to this EPRI product, you acknowledge that it is your obligation to consult with your company's legal counsel to determine whether this access is lawful. Although EPRI may make available on a case-by-case basis an informal assessment of the applicable U.S. export classification for specific EPRI products, you and your company acknowledge that this assessment is solely for informational purposes and not for reliance purposes.

Your obligations regarding U.S. export control requirements apply during and after you and your company's engagement with EPRI. To be clear, the obligations continue after your retirement or other departure from your company, and include any knowledge retained after gaining access to EPRI products.

You and your company understand and acknowledge your obligations to make a prompt report to EPRI and the appropriate authorities regarding any access to or use of this EPRI product hereunder that may be in violation of applicable U.S. or foreign export laws or regulations.

About EPRI

Founded in 1972, EPRI is the world's preeminent independent, non-profit energy research and development organization, with offices around the world. EPRI's trusted experts collaborate with more than 450 companies in 45 countries, driving innovation to ensure the public has clean, safe, reliable, affordable, and equitable access to electricity across the globe. Together, we are shaping the future of energy.

EPRI
3420 Hillview Avenue, Palo Alto, California 94304-1338 USA
800.313.3774 ▪ 650.855.2121 ▪ askepri@epri.com ▪ www.epri.com